

# **Non-Precious Cathode Electrocatalytic Materials for Zinc-Air Battery**

by

**Baejung Kim**

A thesis  
presented to the University of Waterloo  
in fulfillment of the  
thesis requirement for the degree of  
Master of Applied Science  
in  
Chemical Engineering

Waterloo, Ontario, Canada, 2013

© Baejung Kim

## **Author's Declaration**

I hereby declare that I am the sole author of this thesis. This is a true copy of the thesis, including any required final revisions, as accepted by my examiners.

I understand that my thesis may be made electronically available to the public.

## **Abstract**

In the past decade, rechargeable batteries attracted the attention from the researchers in search for renewable and sustainable energy sources. Up to date, lithium-ion battery is the most commercialized and has been supplying power to electronic devices and hybrid and electric vehicles. Lithium-ion battery, however, does not satisfy the expectations of ever-increasing energy and power density, which of their limits owes to its intercalation chemistry and the safety.<sup>1-2</sup> Therefore, metal-air battery drew much attention as an alternative for its high energy density and a simple cell configuration.<sup>1</sup> There are several different types of metal-air batteries that convey different viable reaction mechanisms depending on the anode metals; such as Li, Al, Ca, Cd, and Zn. Redox reactions take place in a metal-air cell regardless of the anode metal; oxidation reaction at the anode and reduction reaction at the air electrode. Between the two reaction, the oxygen reduction reaction (ORR) at the air electrode is the relatively the limiting factor within the overall cell reactions. The sluggish ORR kinetics greatly affects the performance of the battery system in terms of power output, efficiency, and durability. Therefore, researchers have put tremendous efforts in developing highly efficient metal air batteries and fuel cells, especially for high capacity applications such as electric vehicles. Currently, the catalyst with platinum nanoparticles supported on carbon material (Pt-C) is considered to exhibit the best ORR activities. Despite of the admirable electrocatalytic performance, Pt-C suffers from its lack of practicality in commercialization due to their prohibitively high cost and scarcity as of being a precious metal. Thus, there is increasing demand for replacing Pt with more abundant metals due economic feasibility and sustainability of this noble metal.<sup>3-5</sup> Two different attitudes are taken for solution. The first approach is by optimizing the platinum loading in the formulation, or the alternatively the platinum can be replaced with non-precious materials. The purpose of this work

is to discover and synthesize alternative catalysts for metal-air battery applications through optimized method without addition of precious metals.

Different non-precious metals are investigated as the replacement of the precious metal including transition metal alloys, transition metal or mixed metal oxides, and chalcogenides. These types of metals, alone, still exhibits unsatisfying, yet worse, kinetics in comparison to the precious metals. Nitrogen-doped carbon material is a recently well studied carbon based material that exhibits great potential towards the cathodic reaction.<sup>6</sup> Nitrogen-doped carbon materials are found to exhibit higher catalytic activity compared to the mentioned types of metals for its improved conductivity. Benefits of the carbon based materials are in its abundance and minimal environmental footprints. However, the degradation of these materials has demonstrated loss of catalytic activity through destruction of active sites containing the transition metal centre, ultimately causing infeasible stability. To compensate for these drawbacks and other limits of the nitrogen-doped carbon based catalysts, nitrogen-doped carbon nanotubes (NCNT) are also investigated in the series of study.

The first investigation focuses on a development of a simple method to thermally synthesize a non-precious metal based nitrogen-doped graphene (NG) electrocatalyst using exfoliated graphene (Ex-G) and urea with varying amounts of iron (Fe) precursor. The morphology and structural features of the synthesized electrocatalyst (Fe-NG) were characterized by SEM and TEM, revealing the existence of graphitic nanoshells that potentially contribute to the ORR activity by providing a higher degree of edge plane exposure. The surface elemental composition of the catalyst was analyzed through XPS, which showed high content of a total N species (~8 at.%) indicative of the effective N-doping, present mostly in the form of pyridinic nitrogen groups. The oxygen reduction reaction (ORR) performance of the catalyst was evaluated by

rotating disk electrode voltammetry in alkaline electrolyte and in a zinc-air battery cell. Fe-NG demonstrated high onset and half-wave potentials of -0.023 V (vs. SCE) and -0.110 V (vs. SCE), respectively. This excellent ORR activity is translated into practical zinc-air battery performance capabilities approaching that of commercial platinum based catalyst.

Another approach was made in the carbon materials to further improve the cost of the electrode. Popular carbon allotropes, CNT and graphene, are combined as a composite (GC) and heteroatoms, nitrogen and sulfur, are introduced in order to improve the charge distribution of the graphitic network. Dopants were doped through two step processes; nitrogen dopant was introduced into the graphitic framework followed by the sulfur dopant. The coexistence of the two heteroatoms as dopants demonstrated outstanding ORR performance to those of reported as metal free catalysts. Furthermore, effects of temperature were investigated through comparing ORR performances of the catalysts synthesized in two different temperatures (500 °C and 900 °C) during the N-doping process (consistent temperature was used for S-doping). Through XPS analysis of the surface chemistry of catalysts produced with high temperature during the N-doping step showed absence of N-species after the subsequent S-doping process (GC-NHS). Thus, the synergetic effects of the two heteroatoms were not revealed during the half-cell testing. Meanwhile, the two heteroatoms were verified in the catalyst synthesized though using low temperature during the N-doping process followed by the S-doping step (GC-NLS). Consequently, ORR activity of the resulting material demonstrated promising onset and half-wave potentials of -0.117 V (vs. SCE) and -0.193 V (vs. SCE).

In combination of these investigations, this document introduces thorough study of novel materials and their performance in its application as ORR catalyst in metal air batteries. Moreover, this report provides detailed fundamental insights of carbon allotropes, and their

properties as potential electrocatalysts and essential concepts in electrochemistry that lies behind zinc-air batteries. The outstanding performances of carbon based electrocatalyst are reviewed and used as the guides for further direction in the development of metal-air batteries as a promising sustainable energy resource in the future.

## **Acknowledgements**

The work reported in this thesis was financially supported by the Natural Sciences and Engineering Research Council of Canada (NSERC), the University of Waterloo and the Waterloo Institute of Nanotechnology.

The author would like to thank Dr. Zhongwei Chen and Dr. Aiping Yu for their wonderful mentorship, guidance, and remarkable supports during the Mater's study.

Thanks to Hey Woong Park, Dong Un Lee, Drew Higgins, Ja-Yeon Choi, Brian Kihun Kim, Dr. Min Ho Seo, Dr. Rongyue Wang, Jason Wu, Yulong Liu, Fathy Hassan, Mohammed Ariful Hoque, Jordan Scott, Hadis Zarrin, Victor Chabot, and Gaopen Jiang for their support and assistance. Very special thanks to Yeonhong Kim for being always being understanding and supportive.

Furthermore, the author would like to acknowledge reviewers including Dr. Zhongwei Chen, Dr. Aiping Yu, Dr. Eric Croiset, and Dr. Michael Fowler.

## **Dedication**

I would like to dedicate this work to my parents.

## Table of Contents

List of Figures .....	xii
List of Tables .....	xiv
List of Abbreviations .....	xv
1.0 Introduction.....	1
2.0 Background.....	5
2.1 Metal-Air Battery.....	5
2.1.1 Operation Principle of Zinc-Air Battery .....	7
2.1.2 Anode: Zinc Electrode .....	9
2.1.3 Electrolyte and Separator .....	10
2.1.4 Cathode: Air Electrode .....	11
2.1.5 Technical Challenges .....	14
2.2 Graphene .....	15
2.2.1 Properties .....	16
Electrical Conductivity .....	16
Geometric Structure .....	17
Functional Structure.....	19
2.3 Carbon Nanotube .....	20
2.4 Material Synthesis and Characterization .....	23
2.4.1 Graphene .....	24

Graphene Oxide .....	24
2.4.3 Scanning Electron Microscopy .....	26
2.4.4 Transmission Electron Microscopy .....	27
2.4.5 X-ray Diffraction .....	29
2.4.6 X-ray Photoelectron Spectroscopy .....	31
2.4.7 Raman Spectroscopy.....	33
2.4.8 Half-Cell Electrochemical Analysis .....	34
2.4.9 Zinc-Air Battery Performance .....	39
3.0 Effects of Iron and Nanoshell Composites on N-Doped Graphene.....	41
3.1 Purpose.....	41
3.2 Experimental Methods .....	42
3.3 Results and Discussion .....	43
3.3.1 SEM and TEM: Structure and Morphology.....	43
3.3.2 XRD Analysis .....	46
3.3.3 XPS Analysis .....	47
3.3.4 ORR Performance.....	48
3.3.5 Zinc-Air Battery Performance .....	52
3.4 Conclusion .....	53
4.0 Effect of Heteroatoms in Graphene and CNT Composite .....	54
4.1 Purpose.....	54

4.2 Experimental Methods .....	55
4.2.1 Oxidized Carbon Nanotube.....	55
4.2.2 Graphene Oxide and Oxidized Carbon Nanotube Composite .....	55
4.2.3 Nitrogen-Doped GC.....	55
4.2.4 Sulphur-Doped GC-N .....	56
4.3 Results and Discussion .....	56
4.3.1 SEM: Structure and Morphology.....	56
4.3.2 XPS Analysis .....	59
4.3.3 ORR Performance .....	63
4.4 Conclusion .....	67
5.0 Summary and Future Directions .....	68
References.....	71

## List of Figures

Figure 1. World transportation sector energy consumption.....	2
Figure 2. Theoretical and practical specific energy density of various battery systems.....	6
Figure 3. Overall schematic of a zinc-air battery.....	9
Figure 4. Different morphologies of zinc metal.....	10
Figure 5. Volcano trends in oxygen reduction activity.....	13
Figure 6. Schematics of graphene nanoribbon synthesis.....	18
Figure 7. Nitrogen doped graphene. ....	20
Figure 8. Folding direction from graphene to form SWNT.....	21
Figure 9. TEM image of a typical NCNT.....	23
Figure 10. Apparatus of scanning electron microscope.....	27
Figure 11. Principle behind TEM. ....	28
Figure 12. Schematic of XRD operation.....	30
Figure 13. HR-TEM analysis of a typical N-doped graphene. ....	32
Figure 14. RDE voltammetry setup and RDE electrode schematic.....	36
Figure 15. ORR polarization of an active catalyst.....	38

Figure 16. Assembled prototype of zinc-air battery. ....	40
Figure 17. SEM and TEM images of Fe-NG and its derivatives.....	43
Figure 18. SEM and TEM images of after post treatment of Fe-NG .....	45
Figure 19. Physical and composition analysis of Fe-NG-30. ....	47
Figure 20. Linear sweep voltammetry (LSV) first comparisons of Fe-NG.....	49
Figure 21. Linear sweep voltammetry (LSV) second comparisons of Fe-NG. ....	51
Figure 22. Zinc-air battery performanc of Fe-NG-30.....	52
Figure 23. SEM images of GO and O-CNT composite.....	57
Figure 24. SEM image of GC-NL.....	58
Figure 25. SEM image of GC-NLS. ....	59
Figure 26. XPS analysis of GC-NLS .....	61
Figure 27. XPS analysis of GC-NHS.....	62
Figure 28. Linear sweep voltammetry (LSV) first comparisons of GC-NS .....	65
Figure 29. Linear sweep voltammetry (LSV) comparisons of GC-NS vs. Pt-C.....	66

## List of Tables

Table 1. Characteristics of Metal-air cells. ....	8
Table 2. Comparison conductivity by different reduction methods. ....	17
Table 3. Relative atomic percentage of elements. ....	63
Table 4. Relative atomic percentage of C-1s species .....	63
Table 5. Relative atomic percentage of N-1s species .....	63
Table 6. Relative atomic percentage of S-2p species .....	63

## List of Abbreviations

CNT	Carbon nanotube
CV	Cyclic voltammetry
CVD	Chemical vapour deposition
DWNT	Double-walled nanotube
EELS	Electron energy loss spectroscopy
Ex-G	Exfoliated graphene
GC	Graphene and CNT composite
GO	Graphene oxide
H-GO	Highly oxidized graphene oxide
HR-TEM	High resolution transmission electron microscopy
HR-XPS	High resolution X-ray photoelectron spectroscopy
K-L	Koutecky-Levich
LSV	Linear sweep voltammetry
MWNT	Multi-walled nanotube
N-5	Pyrrolic group
N-6	Pyridinic group
N-C	Quaternary nitrogen group
N-O	Oxidized nitrogen group
NCNT	Nitrogen-doped carbon nanotube

NG	Nitrogen-doped graphene
OER	Oxygen evolution reaction
ORR	Oxygen reduction reaction
Pt-C	Carbon supported platinum
RDE	Rotating disk electrode
SAED	Selected area electron diffraction
SEM	Scanning electron microscopy
SWNT	Single-walled nanotube
TEM	Transmission electron microscopy
XPS	X-ray photoelectron spectroscopy

## **1.0 Introduction**

Humanity is faced against many challenges raised from consistent population which by the year of 2050 the population would reach nine billion. Consequently, the energy demand by that year would triple of today's. It is duty of the generations of today to satisfy the needs of present without compromising the ability of the future to meet their own needs. The research proceeds having its ultimate aim to free the dependency on depletable and non-renewable resources. The energy storage is one of many inevitable challenges to reach to goal. The increasing market size and advancement in microelectronic devices demand for higher energy density, safe, inexpensive, and reliable power sources.<sup>7</sup> The increasing population density and the rapid growth of transportation sector are the result of growing economic activities in developing countries. Consequently, these developments inherently increased energy consumption by the transportation sector – by more than 11 percent per year in average.<sup>8</sup> Figure 1 describes that the higher energy consumption by transportation sector than other sectors combined. Therefore, it is essential for the society to find a way to improve energy efficiency. Also, possible impacts to the environment of a new energy source are key factor that must be considered. This emphasizes the importance of the search for renewable and sustainable energy sources that can satisfy the demands of the future.

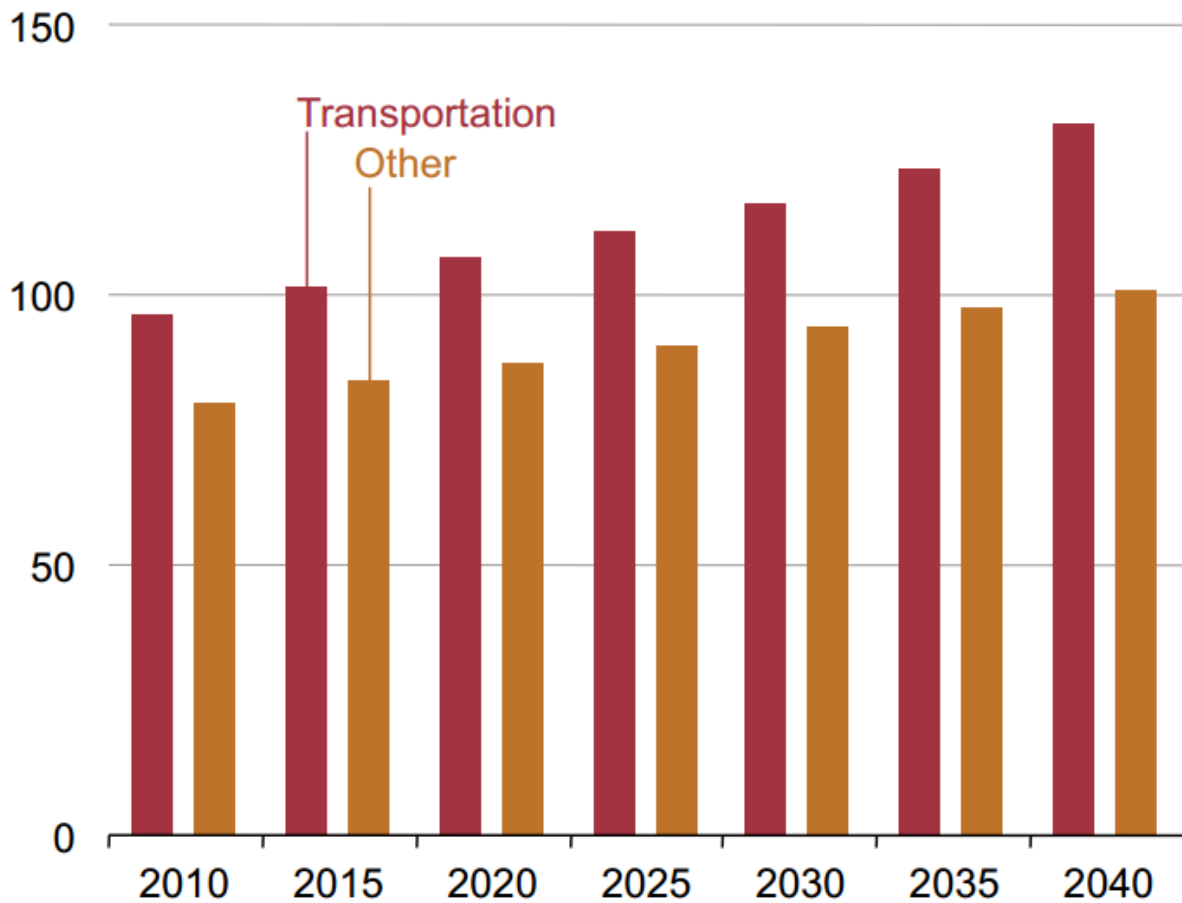


**Figure 1.** World transportation sector energy consumption in 2010-2040 in quadrillion Btu. Reprinted from [8], Copyright 2013, with permission from U.S. Energy Information Administration.

Producing electrical energy was achieved by different technologies through which derived from utilizing non-depleted resources, representatively wind, water, solar power, photovoltaics, biomass, and geothermal. Conventionally, pumped hydro is the preferable method of electrical energy storage, yet its feasibility suffers due to its site specific nature and high capital costs for large scale operation.<sup>9</sup> Other developing energy technologies (wind and solar power) are constrained by climate conditions.<sup>10-11</sup> As an alternative to those mentioned, electrochemical energy conversion system offers attractive options.<sup>12-13</sup> Electrochemical conversion technologies – *batteries* – are the most promising technology offering elimination/reduction of carbon emission, high efficiency, and great energy sustainability.<sup>2, 12</sup> Battery systems conventionally are

closed system. The active masses during the redox reaction are established as of the charge transfer between the two oppositely charged electrodes through the charge transfer media (electrolyte). Different voltages are achieved through flexible selection of the electrode composition and of their unique characteristics during the redox reaction.<sup>2, 14</sup> Through the reactions of which occurs due to the potential difference, batteries are capable of delivering high current pulses without having additional auxiliary units.<sup>14-15</sup> As a result of these beneficial features, batteries dominantly have been respected in the electronic device market, and will continue to be preferred over other storage technologies. Recently, transportation sector has gained interests in developing the current battery technology for the electrification of automobiles reducing the consequential air pollution.<sup>16</sup> Since 1990, lithium-ion battery became revolutionary in the electronic appliances as the most promising battery for its high energy efficiency, energy density, and high cycle capacity.<sup>2, 17-18</sup> Yet, lithium-ion battery faces many challenges adapting in the automobile electrification by which restriction is derived from its unsatisfying energy density that ranges from 200 – 250 Whkg<sup>-1</sup>.<sup>1</sup> In addition, the intrinsic limitations of lithium-ion battery are from its intercalating chemistry; its irreversible intercalating materials in the positive electrode material are responsible for its insufficient energy density and swelling battery cost.<sup>19-20</sup>

Recently, metal-air batteries have attracted much attention as an alternative to lithium-ion battery owing to its significantly high energy density and reducing environmental footprints.<sup>1-2</sup> Moreover, a wide selection of different anode metals is exceptionally appealing, which allows to adjust its energy storage capacity in a wide range for targeting specific applications. Within the selection of anode metals, zinc-air and lithium-air have gained much attention for their specific energy densities of 1084 Whkg<sup>-1</sup> and 5200 Whkg<sup>-1</sup>, respectively, accounting the mass of oxygen

as of being the metal-air batteries.<sup>1, 21-22</sup> Nevertheless, the metal-air battery technology, regardless to the selection of anode electrode, faces challenges in the air electrode. The air cathode determines the battery performance, durability, and the cost of the battery system.<sup>23-24</sup> The catalysts in the cathode facilitates oxygen reduction and evolution reactions (OER) which the rates of these reaction determines the performance of the battery.<sup>25</sup> Typically, catalysts for metal-air batteries include precious metals and alloys<sup>26-30</sup>, metal oxides supported on carbon materials<sup>31-32</sup>. Despite of the excellent theoretical specific energy density of metal-air batteries, diminishing cycle life and cycle efficiency of batteries due to degradation and carbon oxidation of these catalysts are the major obstacles in the way to commercialization of metal-air batteries.

The purpose of this report is to further enhance the performance of metal-air batteries through evaluation of catalysts in the air electrode, which is the major hindering concern in the commercialization of the metal-air battery. Herein, detailed overview of metal-air battery, specifically for zinc-air battery, will be established including fundamental principles of operation and current stage in the development. After, different methods of analyses and characterization methods used in the investigations will be reviewed. In addition, method of synthesis and experimental methods will be described followed by investigations on the novel catalysts serving as cathode materials. Subsequently, the results of investigations will be discussed regarding electrochemical performances of the novel catalysts in a prototype zinc-air battery.

## 2.0 Background

### 2.1 Metal-Air Battery

The metal-air battery was first introduced in 1868 by Leclanche using manganese dioxide with carbon support as air electrode. The metal-air battery was further developed adjusted with modern design.<sup>33</sup> In Figure 2, metal-air battery evidently displays incomparably higher energy densities compared to other electrochemical energy storage devices.<sup>1, 31</sup> This tremendous energy density of metal-air batteries is due to its open system assembly through which the oxygen is provided.<sup>34-35</sup> Specifically, lithium-air battery system displays exceptional energy density almost near 12,000 Whkg<sup>-1</sup>, which surpasses the theoretical energy density of the most well-known energy-densed liquid, gasoline.<sup>23, 36</sup> Additionally, the metal-air battery demonstrations long shelf life<sup>1, 37-39</sup>, low cost of electrode materials<sup>35, 40-41</sup>, and environmental kindly<sup>35, 40</sup>.

Considering the selection of anode metals, the specific energy density of the metal-air battery varies accordingly to the choice of the anode metal. Referring to Figure 2, lithium-air battery demonstrates the highest theoretical and practical energy density.<sup>1, 42</sup> Attribution to the spontaneous nature of lithium – oxidation of lithium metal to become to form lithium hydroxide (LiOH) once in contact with atmospheric air – the lithium-air battery operates at much higher coulombic efficiencies owing to the retardation of corrosion by the formation of the metal oxide. This parasitic formation ultimately causes hindrance during discharge requiring the change of electrolyte.<sup>42</sup> Despite of advantages such as rich voltage output and outstanding specific energy density of lithium metal as anode, commercialization of the lithium-air battery system encounters challenges concerning the operational cost and safety issues during production.<sup>37, 42</sup>

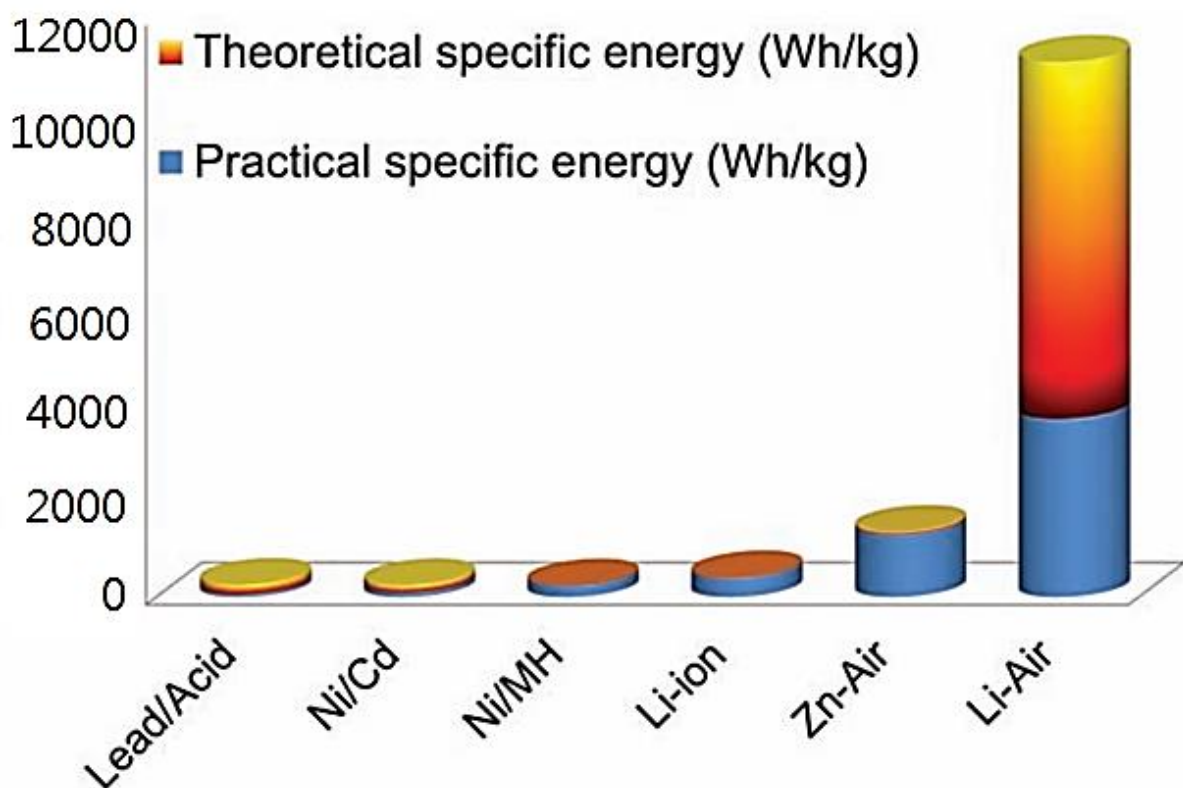


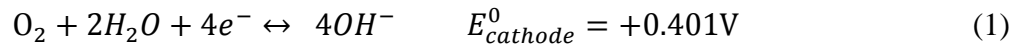
**Figure 2.** Theoretical and practical specific energy density of various battery systems including the representing types of metal-air battery systems, lithium-air and zinc-air. Reprinted from [1], Copyright 2011, with permission from Wiley.

In general, the metal-air battery operates in alkaline or neutral electrolyte, which the electrons from the oxidized anode metal are transferred to the load. Within the selection of metals as the anode of the battery, zinc is most favourable for its favourable electropositivity and stability in both types (aqueous and alkaline) of electrolytes.<sup>24, 37, 42-43</sup> Zinc metal serves advantages compared to other candidate anode metals in a metal-air battery in one of these areas: production cost, polarization and stability, parasitic corrosion, uniformity dissolution, and practical handling and safety.<sup>42, 44-45</sup> In addition, zinc offers relatively decent stability in alkaline media at low cost due to its high abundance.<sup>39, 46</sup> Therefore, zinc-air battery is anticipated to be the most promising metal-air battery to be successful in multiple markets. In order for zinc-air battery system to be effectively commercialized as power source for portable (cell phones and laptops) and large size

(vehicles and transportation) applications, problems of undesired dendrite formation, uneven dissolution, and insufficient air electrode performance need to be addressed.

### 2.1.1 Operation Principle of Zinc-Air Battery

Electrochemical battery performance heavily depends on the activities of reduction and oxidation reaction at air electrode and anode metal, respectively. In details, the half-cell reaction that reduces oxygen in the atmospheric air at the air electrode is written as:



In equation 1,  $E_0$  represents the standard half-cell electrode potential with respect to standard hydrogen electrode (SHE). This theoretical electrode potential of the cathode is compared to that of oxidation of anode metal as a pair representing the theoretical cell voltages. Thus, the oxidation reaction of metals at the anode can be written as:



where M denotes the metal used for anode the and the value of  $n$  depends on the valence change for the oxidation of the metal. Therefore, the standard electrode potential of the metal anode would depend on the type of the metal chosen. Table 1 describes theoretical cell voltage, valence change ( $n$ ), and theoretical and practical operating voltage of different metal anodes in metal-air battery.<sup>42</sup> Thereby, the difference of the standard electrode potentials of the two opposing electrodes defines the theoretical battery voltage through the following calculation:

$$E_{battery}^0 = E_{cathode}^0 - E_{anode}^0 \quad (3)$$

**Table 1.** Characteristics of Metal-air cells. Reprinted from [42], Copyright 2010, McGraw-Hill.

<b>Metal anode</b>	<b>Electrochemical equivalent of metal (Ahg<sup>-1</sup>)</b>	<b>Theoretical cell voltage (V)</b>	<b>Valence change</b>	<b>Theoretical specific energy (kWh kg<sup>-1</sup>)</b>	<b>Practical operating voltage (V)</b>
Li	3.86	3.4	1	13.0	2.4
Ca	1.34	3.4	2	4.6	2.0
Mg	2.20	3.1	2	6.8	1.2-1.4
Al	2.98	2.7	3	8.1	1.1-1.4
Zn	0.82	1.6	2	1.3	1.0-1.2
Fe	0.96	1.3	2	1.2	1.0

The voltage outlet of the cell is during discharge of the battery. On the other hand, the role of anode and cathode reverses during charging of the battery (the metal anode becomes the cathode and the air electrode becomes the anode).<sup>47</sup>

Zinc-air battery demonstrates the most promising power and energy density and is also already has launched in the commercial market as in a form of coin-cell, which is incapable to be recharged. Zinc-air battery, like any other types of metal-air battery, consists of three main components: cathode (air electrode), anode, and electrolyte and separator. Figure 3 describes overall schematic of a zinc-air cell including the overall battery reaction in alkaline media. The described battery voltage correctly states 1.65 V (*vs. SHE*), which is the difference in potential between the positive and the negative electrodes. During the discharge, zinc readily donates two electrons to cathode alongside of oxidation reaction forming zincate molecules ( $\text{Zn(OH)}_4^{2-}$ ) due to the nature of standard potentials of the opposing electrode. The two released electrons travel through the external circuit to the air electrode; there, electrons are used to reduce the oxygen consumed from the ambient air. This process is known as a three-phase reaction; the reaction takes place in catalyst (solid), electrolyte (liquid), and oxygen (gas).<sup>1</sup> The intake of oxygen enriches hydroxyl ions in the electrolyte medium along with generation of water and oxygen gas

as by-products. The replenishment of hydroxyl ions further shifts the reaction towards the formation of zincate molecules which ultimately dissociates into zinc oxide (ZnO).

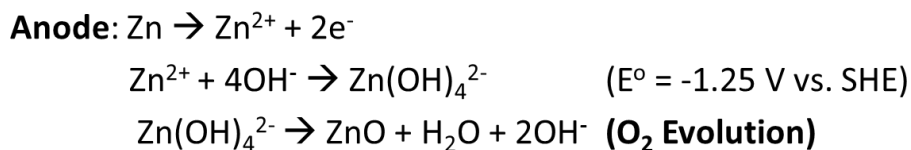
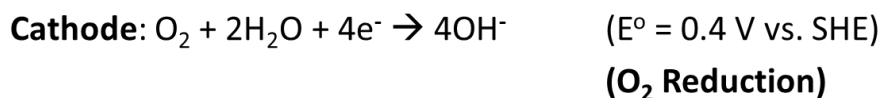
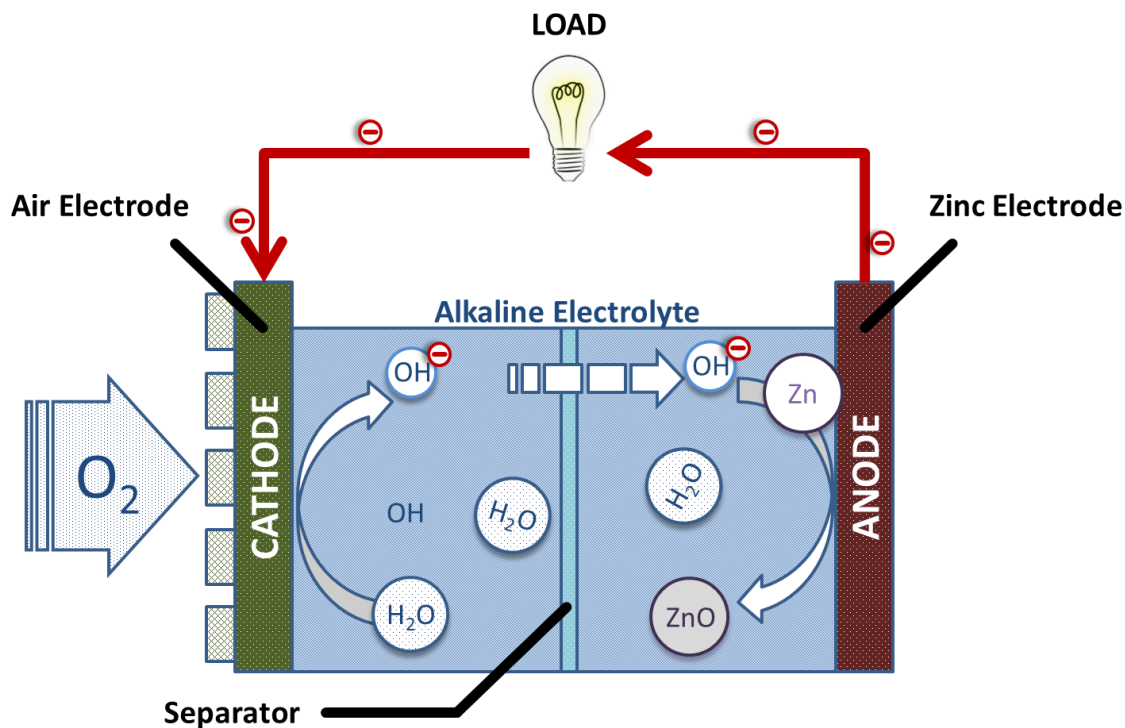


**Figure 3.** Overall schematic of a zinc-air battery

### 2.1.2 Anode: Zinc Electrode

Pure zinc metal is used as the anode active material of which zinc oxidation occurs during discharge. Therefore, improved reaction efficiency through increased surface area of the zinc electrode could promote improved battery performance.<sup>1</sup> Zinc anode surface area can be modified by controlling the morphology of zinc particles. Change in battery performance was

demonstrated from different zinc morphologies – such as particles, dendrites, and fibre marking each of its feasibility.<sup>48-49</sup>

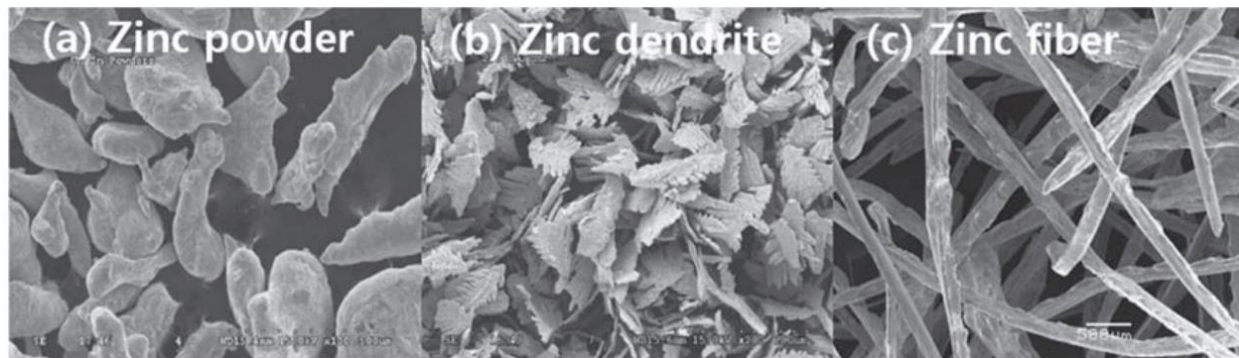


**Figure 4.** Different morphologies of zinc metal. Reprinted from [1], Copyright 2011, with permission from Wiley.

The most studies shifted away from improving zinc anode since the zinc-air battery utilizes pure zinc metal. In addition to morphology modification, zinc composition could be altered through coating with mercury for enhanced conductivity between the zinc metals and the current collector.<sup>1</sup> Moreover, studies also suggested alloying zinc with other metals such as nickel<sup>50</sup>, indium<sup>50</sup>, palladium<sup>50-51</sup> and cadmium<sup>50-51</sup> enhanced the inhibition of parasitic corrosion and undesired hydrogen evolution reaction (HER).

### 2.1.3 Electrolyte and Separator

Typical alkaline electrolytes in zinc-air batteries include potassium hydroxide (KOH), sodium hydroxide (NaOH), and lithium hydroxide (LiOH).<sup>52</sup> Potassium hydroxide has been most popularly used in the battery system for their desirable ionic conductivity of potassium (73.5  $\Omega$ -1  $\text{cm}^2/\text{equiv}$ ) compared to the other cation types.<sup>53</sup> The concentration of electrolyte has to be carefully chosen in order to optimize the cell performance; increasing concentration of electrolyte would reduce the resistance, but high concentration would lead to high viscosity through promoting the formation of ZnO in the electrolyte. On the contrary, decrease of KOH

concentration would lead to undesirable HER.<sup>54</sup> The optimal concentration of KOH was reported to be around 30% considering the maximum ionic conductivity.<sup>39</sup>

The purpose of separator in zinc-air battery system is to selectively transport hydroxyl ions in the electrolyte from the air electrode side to zinc anode electrode through permeable pores.<sup>55</sup> Ideal requirements for a separator in serving this purpose are stability in basic solution (electrolyte molarity), appropriate pore size and porosity, high ion conductivity and insulating to electron transportation.<sup>1</sup> The porosity of the separator should be fine enough to restrict the migration of zincate ions from the anode to the cathode. Separator for a possible secondary zinc-air battery requires unresponsiveness to oxidation, ability to withstand during charge and discharge, high electrolyte absorption, and a fine porous structure to retain electrolyte as additions to the basic necessities of a separator for a primary zinc-air battery.<sup>1, 56</sup>

#### **2.1.4 Cathode: Air Electrode**

The fact that the air cathode draws active mass from the ambient air is the major advantage that metal-air battery system offers. Therefore, in order to serve the purpose, the air electrode requires proper catalysts for ORR and high porous structure. The purpose of catalysts is to alleviate the activation energy for ORR, and the required structural features of the air electrode simultaneously contribute in serving the very purpose. Therefore, the air electrode needs to be gas diffusive in order to be able to allow access of air in order to carry out ORR, and need to be electrically conductive. The air electrode consists of a gas diffusion layer (GDL), a current collector, and a catalyst layer.<sup>57</sup> The gas diffusion layer acts as a substrate for catalysts and provides diffusion path for oxygen to travel through. The diffusion occurs through pores of which carbon derived materials such as activated carbon and carbon nanotubes (CNT) are used

as the substrate. Besides the carbon material, a hydrophobic binder such as polytetrafluoroethylene (PTFE) is widely used for carbon fibres to bond together. The hydrophobicity of the GDL maintains permeation to air but not the electrolyte. From reported studies, the micropores (0.2 – 2 nm) of the carbon material had diminishing effects to the cathode performance.<sup>58</sup> In consideration of prominent secondary zinc-air battery, the diffusive carbon material should additionally be able to endure reactive oxygen ions from OER during charging.

Next to the GDL, a catalytic active layer that ORR takes place consists of catalysts, carbon materials, and the binder. The mechanism of ORR is very complex involving multiple molecular adsorptions-desorptions, various elementary reaction steps, and formation different reaction products. However, it is believed that there are two reaction pathways that the ORR mechanism pursues during discharge: four-electron pathway and two-electron pathway. The four-electron pathway induces oxygen to be directly reduced to hydroxyl ion (equation 1), meanwhile the oxygen is indirectly reduced to hydroxyl ion via forming hydroperoxyl radical ( $HO_2^-$ ) (equation 4).



The  $HO_2^-$  radical, fortunately, can further be reduced to hydroxyl ions through the following equation:



This indirect formation of  $OH^-$  ions via two-electron pathway deteriorates the power density and causes high rate of discharge due to the large overpotential. Therefore, appropriate catalysts need to be found to either facilitate the four-electron pathway or to reduce the oxygen reduction overpotential.<sup>1</sup> The most desirable ORR active catalysts belong to precious metals such as Pt, Pd,

and Ag. These ORR active catalysts demonstrate high reduction performance through structural manipulation of these ORR catalysts, yet the cost of the air electrode manufacturing increases incoherently. Due to the cost of noble metals and their insufficient abundance, calcogenides<sup>59</sup> and other transition metals and its alloys and oxides<sup>26-30</sup> are chosen as alternatives. The ORR activities of metals, and both alloys and faced-metals are predicted through a complex computation.<sup>60</sup> Figure 5 describes volcano trend of oxygen reduction activity of the metals mentioned plotted as a function of oxygen binding energy.

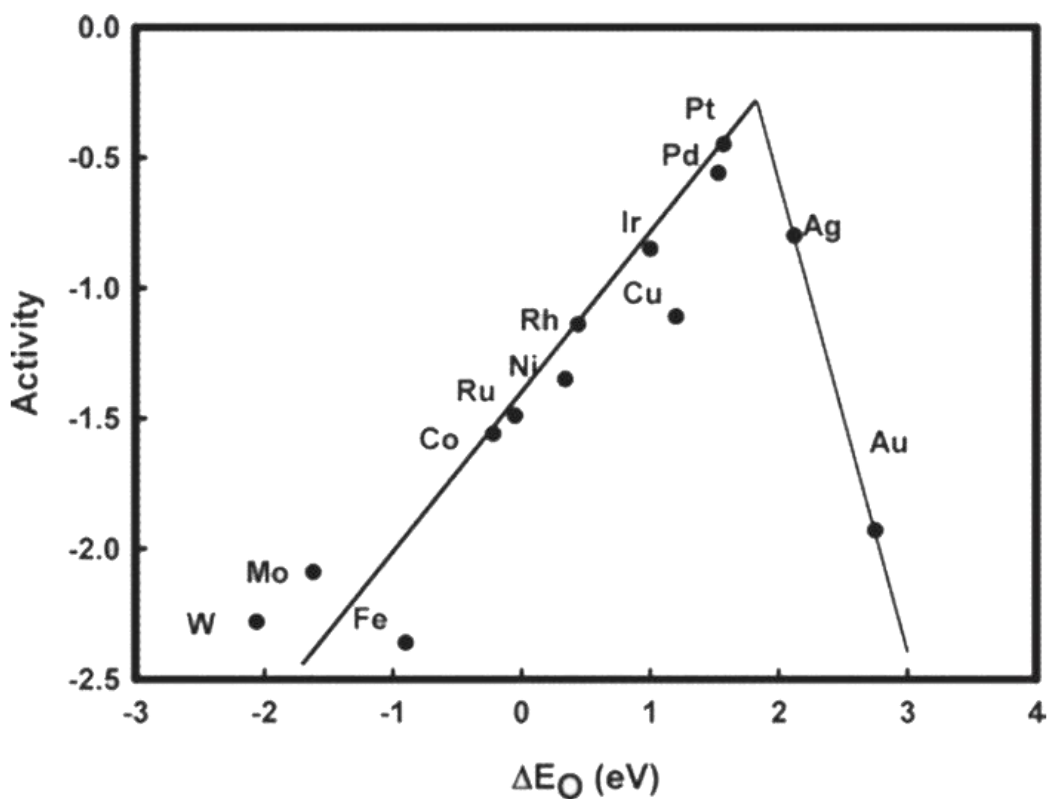


**Figure 5.** Volcano trends in oxygen reduction activity. Reprinted from [60], Copyright 2004, with permission from American Chemical Society.

As shown in Figure 5, noble metals such as Pt and Pd show high ORR activity, but the zinc-air battery application is not obligated to employ noble metal catalysts due to its privilege of having alkaline electrolyte.<sup>61</sup> As an alternative, metal oxide such as perovskite, pyrochlore and spinel, and their mixtures are known as prominent catalyst materials for ORR.<sup>4, 61-65</sup> Extensive work is in progress in order to understand the properties and the characteristics of non-precious metals and metal oxides as successful ORR catalysts for zinc-air battery applications.

### 2.1.5 Technical Challenges

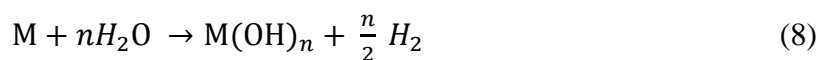
Further improvements are required regarding all the components mentioned above for commercialization of zinc-air battery. Current technology of zinc-air battery performances are restrained in reaching state of commercialization by many factors. These factors include polarization, electrolyte carbonation, water transpiration, and efficiency during charge and discharge.<sup>42</sup> The polarization, the voltage drop of the metal-air battery, is sharper with increasing current than other types of batteries due to diffusion and other limitations from drawing oxygen from the ambient air showing for high-power applications.<sup>42</sup> Another factor derived from the fact the zinc-air battery is an open system is the electrolyte carbonation. Electrolyte is vulnerable to absorbing carbon dioxide (CO<sub>2</sub>) from the ambient air which would lead to crystallization of carbonate in the porous air electrode via the following reactions<sup>42, 66-67</sup>:



The crystallization of carbonate is likely to inhibit the air access and cause mechanical damage ultimately deteriorating the battery performance.<sup>42</sup> Additional challenge to be considered due to the open system of the battery is the water vaporization. Water particles in the electrolyte may

vaporize and be transferred to atmosphere in the presence of partial pressure difference between the electrolyte and the air. Consequently, the loss of water would lead to increase of concentration of electrolyte increasing of its viscosity and eventually drying out and premature failure.

Most metals are capable of generating hydrogen due to thermodynamically instability in aqueous electrolyte and react with the electrolyte to cause parasitic corrosion through the following reaction:



Consequently, this corrosion reaction will cause decrease in coulombic efficiency of the anode and cause loss of capacity.

The greatest challenges lie within the air electrode of the zinc-air battery. The kinetics of ORR are very sluggish due to high overpotential which decreases the power density; the same problem applies during charge, OER at the cathode. Therefore, developing the air cathode inquires most of the total cost of the zinc-air battery.<sup>62, 68</sup> In addition, parasitic products such as hydroperoxyl radicals generated during the ORR can lead to earlier degradation of the active catalysts and will impact the durability and the efficiency of the zinc-air battery. Therefore, this thesis will further investigate novel carbon based ORR catalysts active in alkaline electrolyte as an approach towards developing stable and effective catalyst for ORR.

## 2.2 Graphene

Graphene has received much attention from various fields of study for its unique and superior properties. Graphene is a monolayer of sp<sup>2</sup> bonded carbons atoms, which exhibit high surface areas, outstanding chemical/mechanical/thermal stability, and excellent electron mobility owing

to its single-atom thickness.<sup>69-70</sup> The graphene oxide (GO) is a compound that consists carbon, oxygen, and hydrogen in variable ratios. GO is obtained by treating graphite with strong oxidant. This material was first found in 1859 by treating graphite with potassium and fuming nitric acid. Since then, several improvements have been made to the procedure to enhance product yield and safety.<sup>71-74</sup> The synthesis graphene was first done through mechanical exfoliation called without involving GO as its antecedent.<sup>75-76</sup> Despite of the simple and low-budget technique of mechanical exfoliation, the resulting graphene showed irregular shapes and sizes (several microns) and uncontrollable azimuthal orientation.<sup>73</sup> Therefore, other methods of graphene synthesis were considered such as chemical vapour deposition (CVD) using methane or other carbon-containing gases, low-energy electron diffraction (LEED). These methods, however, suffered from extremely low yield and impracticality in commercialization.<sup>73, 77</sup> As solution, bulk methods to exfoliate GO through removing the oxygen-containing groups was explored. One of the most attractive methods of obtaining graphene is through chemical conversion and thermal reduction of GO.

## **2.2.1 Properties**

### ***Electrical Conductivity***

Graphene is known for its unique properties. As one of its attractive properties, graphene exhibits high electrical conductivity. It is reported that few-layered graphene demonstrates sheet resistance around  $400 \Omega \text{ sq}^{-1}$  at room temperature.<sup>78</sup> Graphene synthesized through CVD method interestingly reported lower sheet resistance about  $30 \Omega \text{ sq}^{-1}$ .<sup>79</sup> Consequently, the graphene reveal low resistance, yet, shows difference in its properties as of the effects to the different reduction methods. Different criterions are set to judge the conductivity of the graphene

including bulk conductivity, powder conductivity, sheet resistance of individual graphene sheet and thin film.<sup>80</sup> Table 2 summarizes the electrical conductivity as of the effects to different reduction method from GO to graphene.<sup>81-87</sup>

**Table 2.** Comparison conductivity by different reduction methods. Reprinted with permission from [95], Copyright 2012, Elsevier.

<b>Reduction Method</b>		<b>C/O ratio</b>	<b><math>\sigma</math> (S/cm)</b>
Hydrazine hydrate		10.3	2
Hydrazine reduction in colloid state		N/A	72
NaBH <sub>4</sub> solution		8.6	0.045
Hydrazine Vapour		~8.8	N/A
Thermal Annealing (900°C, UHV)		~14.1	N/A
Thermal Annealing (1100°C, UHV)		N/A	~10 <sup>3</sup>
Thermal Annealing (1100°C, Ar/H <sub>2</sub> )		N/A	727
Multistep Reduction	NaBH <sub>4</sub> solution	4.78	0.823
	Conc. H <sub>2</sub> SO <sub>4</sub> (180°C)	8.57	16.6
	Thermal Annealing (1100°C, Ar/H <sub>2</sub> )	>246	202
55% HI Reduction		>14.9	298

### ***Geometric Structure***

As implied, the material's electrical conductivity and other properties are closely related to its geometric features such as dimensions.<sup>77</sup> Since the first discovery of zero band gap semimetal graphene through mechanical exfoliation from three-dimensional graphite to two-dimensional graphene, studies were conducted to control the dimension of the graphene – both vertical and lateral dimensions. Besides the low yield, mechanically exfoliated graphene did not offer spatial control, which produced only in micrometer-size sheets, demonstrating impracticality in the wafer industry. As a control of the thickness of the layers of graphene, GO has been reduced through sublimation of silicon.<sup>88-90</sup> In addition, CVD method of depositing carbon layers from carbon-containing gas as the precursor offered mono- or few-layers of graphene films grown on transition metals (Ni, Cu, and Ru).<sup>90-93</sup> Among the different metal catalysts were explored as

seeds for carbon monolayers to grow on, copper (Cu) was able to produce the largest lateral dimension graphene films owing to its unique surface catalytic mechanism.<sup>94</sup> Despite of the ability to produce high quality monolayer graphene films, CVD method of producing graphene cost an extra transfer step from the metal substrates to the substrate of choice.<sup>88</sup> Therefore, the final graphene layer is vulnerable to impurities and surface folding and breaking.<sup>88</sup> Furthermore, exfoliation of CNT produced zero-band gap carbon layers, which complies with the definition of graphene. This method involved ‘unzipping’ CNT to produce graphene nanoribbons (see Figure 6).<sup>95-97</sup> Through both mechanical and chemical methods of unzipping CNT in production of graphene nanoribbons have been studied, but all methods added complexity to the process of production, such as potassium intercalation<sup>96</sup>, lithographic<sup>98</sup>, hydrogen plasma etching<sup>99</sup>.

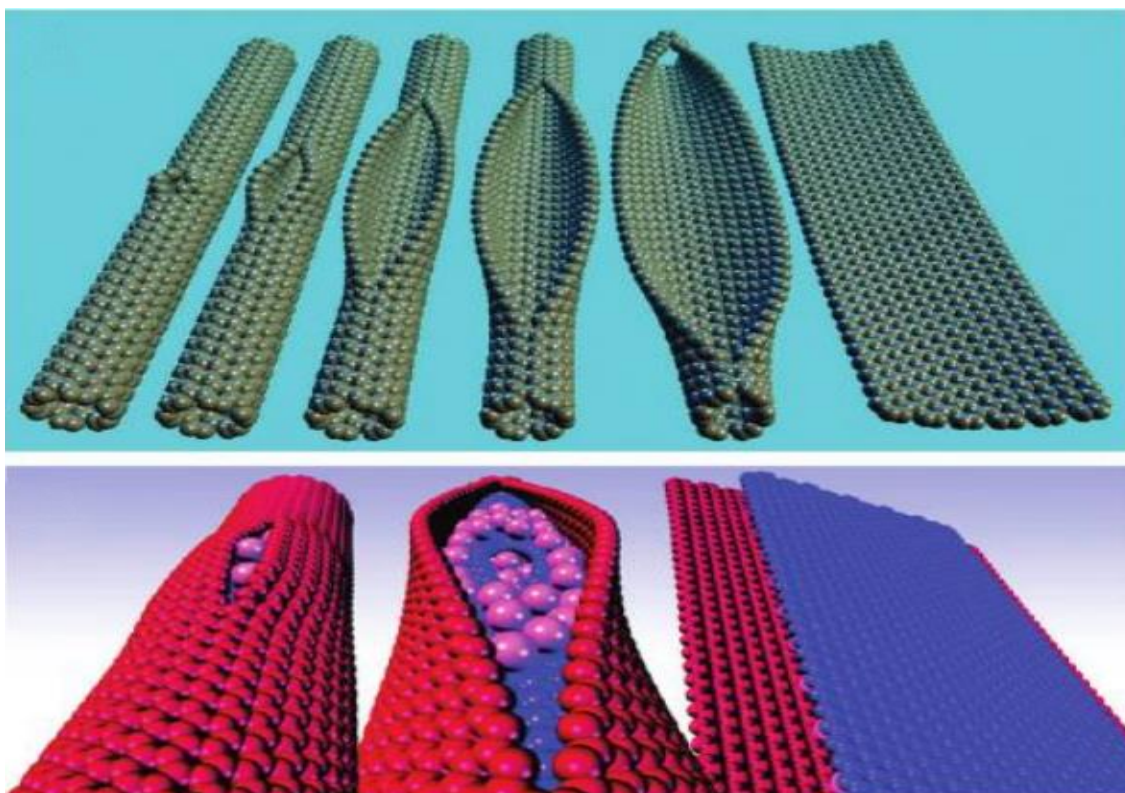


**Figure 6.** Schematics of graphene nanoribbon synthesis. Reprinted with permission from [96] and [97], Copyright 2011, ACS; Copyright 2009, Nature, respectively.

### ***Functional Structure***

As a monolayer of carbon atoms bonded into a hexagonal lattice, graphene possesses favourable properties that allow it to be employed with various conductive metals to enhance ORR. Pristine graphene exhibits ambipolar behaviour with a neutrality point at zero.<sup>78</sup> In addition to graphene metal nanocomposites, dopant heteroatoms, such as nitrogen, show fascinating catalytic activity towards ORR owing to the intrinsic properties of C-N bonding. Several methods have been investigated nitrogen-doped graphene (NG) (see Figure 7). As a primary work, nitrogen containing precursors such as melanine was added to the carbon to produce NG during the CVD process.<sup>100</sup> Another technique involves thermal annealing of graphene oxide with ammonia gas (NH<sub>3</sub>).<sup>101</sup> Through the heat treatment of GO, the oxygen groups of graphene oxide are thermally reduced to form exfoliated graphene layers.<sup>102-103</sup> Simultaneously, this synthesis technique also allows for the modification of graphene properties through substitutional doping of the nitrogen and can enhance electron transfer efficiency of graphene.<sup>103</sup> Different methods of N-doping have been reported, most commonly by chemical vapour deposition (CVD)<sup>102, 104-105</sup>, plasma treatment<sup>104</sup>, solvothermal treatment<sup>106</sup>, or thermal treatment<sup>107</sup>. For example, a thermal method introduced by Wang et al.<sup>107</sup>, uses NH<sub>3</sub> gas as the N precursor with graphene to produce N-doped graphene (NG) achieving high ORR performance. Recently, Chen et al. have introduced unique thermal methods to reduce GO and dope nitrogen simultaneously into individual graphitic layers to produce NG.<sup>4, 101-102, 107-110</sup> These methods involve instant exposure to high temperatures, which provides electrochemical advantages in comparison to NG produced via different methods. Additional to nitrogen doping, other heteroatoms besides nitrogen are under study to be introduced into graphene.<sup>111-113</sup> This thesis will present methods and resulting electrochemical

analyses of the addition of sulfur atoms to basal plane of graphene as additional dopant next to nitrogen.

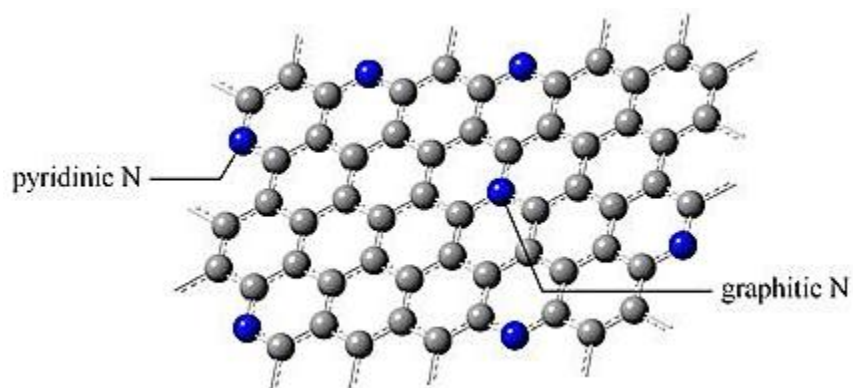


**Figure 7.** Nitrogen doped graphene. Reprinted with permission from [134], Copyrights 2011, ACS.

## 2.3 Carbon Nanotube

Carbon nanotube (CNT) has drawn the attention next to the discovery of Bucky ball (C<sub>60</sub>) since 1991.<sup>117</sup> CNT is known to be simple in atomic compositions but provide tremendous diversity in structures and properties in mechanical<sup>118</sup>, thermal<sup>119</sup>, chemical<sup>120-121</sup>, electrical properties<sup>122</sup>. Popularly, heteroatom such as nitrogen is introduced to CNT consequently exhibiting superior ORR activity compared to that of precious metal catalysts.<sup>123-125</sup> The carbon nanotube is hollow cylindrical structure composed of carbon created by rolling up layers of graphene sheets (see Figure 8).<sup>119</sup> Single layer of graphene layer forms a single-walled nanotube (SWNT), double walls of graphene is rolled up to form double-walled nanotube (DWNT), and multiple layers of graphene leads to forming multi-walled nanotube (MWNT). Therefore, the outside diameter of the CNT varies by its number of layers. Length-wise, CNT ranges from several micrometers to several millimeters.

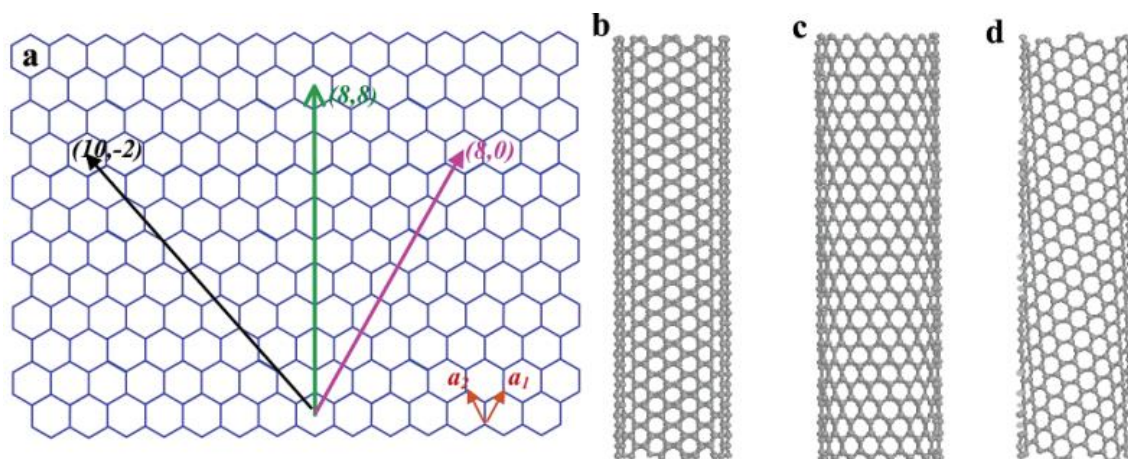


**Figure 8.** Folding direction from graphene to form SWNT. Different direction of folding determines the chirality of CNT. Reprinted from [125], Copyright 2002, ACS.

As folded from honeycomb lattice structured graphene, CNT consists of hexagonal lattice. The directions of folding the graphene sheet results in formation of different chirality of CNT (see Figure 8). The chirality alters the properties of CNT such that the SWNT can be either metal or semiconductor with band gaps that are relatively large regardless to the outside diameter. The most appealing property is the electrical properties. CNT exhibits extremely high electric current density that is far beyond some metals.<sup>122</sup> Additional advantage of employing CNT as catalysts for ORR is its inertness in both aqueous and alkaline conditions owing to its stable sp<sup>2</sup> hybridized covalent bonds. On the contrary, CNT demonstrates low affinity in dioxygen molecules binding caused by neutral charge distribution at equilibrium, which promotes undesirable ORR activity.

As a solution, a heterogeneous dopant is inserted into the graphitic network to modify the charge delocalization of CNT. Different heteroatoms are studied including boron<sup>126-128</sup>, phosphorous<sup>129-130</sup>, and nitrogen<sup>125, 131</sup>. Among the studied heteroatoms, introducing nitrogen atoms to the graphitic network of CNT (noted as NCNT) showed interestingly high ORR activity.<sup>132-134</sup> The

increased affinity for ORR of CNT is reported to be owing to the delocalized charges allowing better flow of charge.

Most widely used technique to synthesize NCNT is through chemical vapour deposition (CVD) at high temperature. The CVD method flows carbon and nitrogen containing gas as precursor as for it to precipitates and consequently construct NCNT. The flow of inert gas (i.e., Ar) accompanies during the flow of the precursor gas. The precipitation sites require a metal seed such as iron, nickel, and copper. As the carbon and nitrogen containing precursor gas flows, the growth of NCNT is initiated at the metal catalyst when the temperature reaches the sublimation point of the precursor gas. At the sublimation point, the carbon and nitrogen containing materials will precipitate on to the metal catalysts, which have already formed into small droplets. Each droplet of molten metal catalysts can only support limited precursor materials until the point of supersaturation. At this point, the carbon atoms will self-assemble onto the surface of the metal catalyst droplets forming hexagonal network. Thus, the synthesized nanotube will consists of nitrogen atoms disrupting the original hexagonal network of CNT due to its bonding properties. Consequently the pyrrolic cyclic rings can be found within the network forming separate compartments within the nanotube structure (see Figure 9).<sup>135</sup> In addition, different configuration arranged between carbon and nitrogen atoms depending on the local atomic interactions will result in different surface nitrogen groups including pyridinic, pyrrolic, quaternary, and pyrrolidone groups.

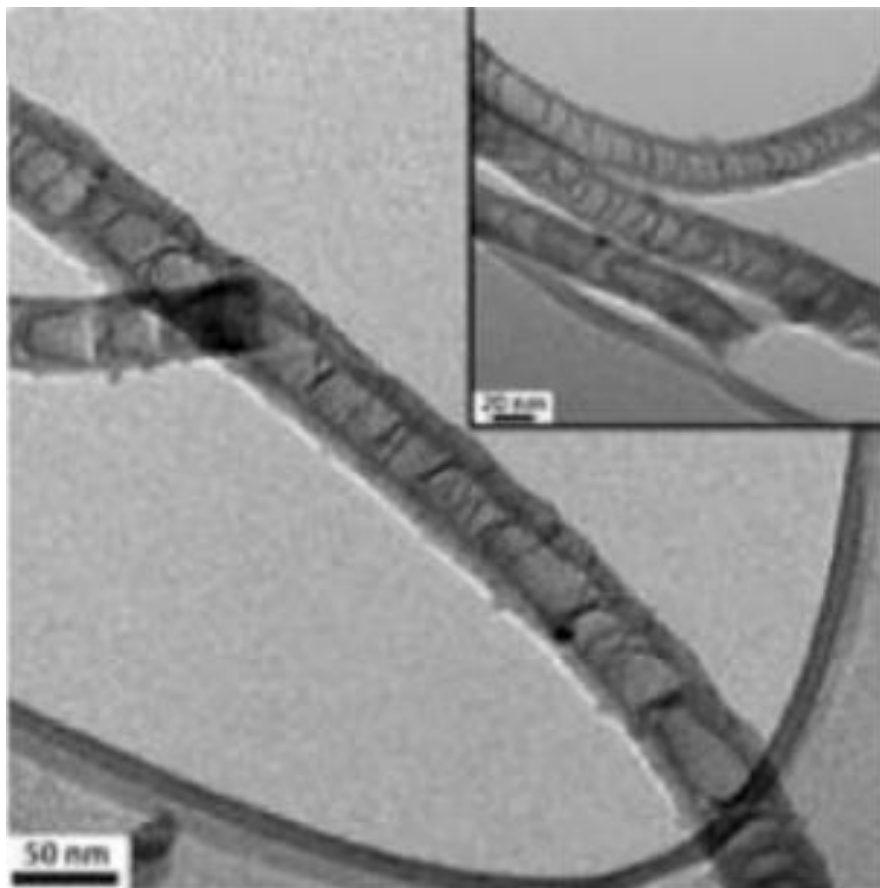


**Figure 9.** TEM image of a typical NCNT. Reprinted from [135], Copyright 2010, Elsevier.

## 2.4 Material Synthesis and Characterization

Graphene oxide is used as the starting carbon substrate for non-precious metal catalysts synthesized in this work. The synthesis methodology of GO, graphene, and nitrogen-doped carbon nanotube is established in this chapter. Also, methods of physical characterizations of the synthesized material are discussed in detail in order to provide understanding of the materials and their properties. These characterizations include *scanning electron microscopy* (SEM), *transmission electron microscopy* (TEM), *X-ray diffraction* (XRD), and *raman spectroscopy*. In addition, *X-ray photoelectron spectroscopy* (XPS) is also conducted to study surface elemental chemistry. The performance as electrochemical catalysts was evaluated through three-electrode

half-cell testing. Additionally, the practical application performance was measured in a zinc-air battery.

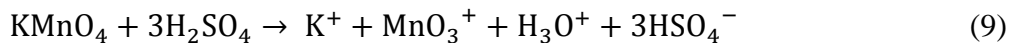
## 2.4.1 Graphene

### *Graphene Oxide*

There are three major techniques introduced in the past to produce graphene oxide (GO). First, in 1859 British chemist, D. C. Brodie, performed formation of GO involved addition of potassium chlorate ( $\text{KClO}_3$ ) to *slurry* graphite in fuming nitric acid ( $\text{HNO}_3$ ) resulting with material composed of carbon, hydrogen, and oxygen.<sup>114</sup> L. Staudenmaier improved this method of preparing GO by adding the chlorate ( $\text{ClO}_3^-$ ) in multiple aliquots over the course of the reaction.<sup>115</sup> In addition, concentrated sulfuric acid was added to increase the acidity in a single reaction vessel, which improved the practicality. Consequently, these changes improved the oxidized level of the produced GO. The both methods made use of nitric acid, a common oxidizing agent and known to react with aromatic carbon surfaces. The reaction involves various oxides containing species such as *carboxyls, lactones, and ketones*. Oxidations by  $\text{HNO}_3$  release gaseous  $\text{NO}_2$  and/or  $\text{N}_2\text{O}_4$  (as demonstrated in Brodie's observation of yellow vapors).<sup>71</sup> Moreover, presence of potassium chlorate ( $\text{KClO}_3$ ) natural source of dioxygen which acts as the reactive species. Through this method of preparing GO, yellow vapor was observed as gases released in presence of  $\text{HNO}_3$ .

Most fundamental work of graphene oxide synthesis was first established by Hummers in 1957.<sup>116</sup> Graphite powder was effectively oxidized in harsh acidic environment involving sulfuric acid and sodium nitrate and adding strong oxidizing agent potassium permanganate ( $\text{KMnO}_4$ ) resulting with GO with about 2.1 of carbon to oxygen ratio.<sup>116</sup> Even though potassium

permanganate is a commonly used oxidant, via reaction with strong acid, sulfuric acid, *dimanganese heptoxide* ( $Mn_2O_7$ ) is far more reactive than its monometallic tetraoxide ( $KMnO_4$ ).



Dimanganese heptoxide is known to detonate at high temperature ( $>55^\circ C$ ) or in contact with organic compounds. The material can selectively oxidize unsaturated aliphatic double bonds over aromatic double bonds, which may sway the structure and reaction pathways during oxidation.

Over the years, this method has been modified in order to achieve higher carbon to oxygen ratio. Recently, an improved method of GO synthesis was reported by Marcano et al. removing sodium nitrate and additionally mixing phosphoric acid.<sup>71</sup> The resulting GO demonstrated more regular structure owing to presence of phosphoric acid and enhance the safety issues of the procedure. In addition, the GO synthesized through the improved method showed much higher oxidation level compared to both conventional and modified of GO produced via Hummers' method. In this work, the improved method of GO synthesis has been modified in order to produce increased oxidized level.

In this work improved method is modified to produce 'highly oxidized graphene oxide (H-GO)'. H-GO was prepared from graphite powder (Alfa Aesar, A Johnson Matthey Company, U.S.A.) through improved method procedure as reported by Marcano et al.<sup>71</sup> In a typical synthesis, graphitic powder (2 g) was dispersed in 400 mL mixture of concentrated  $H_2SO_4$  and  $H_3PO_4$  (9:1) in an ice bath. With continuous agitation, 18 g of  $KMnO_4$  was slowly added to the solution maintaining the temperature of the solution below  $25^\circ C$ . Then the mixture was heated up to  $55^\circ C$  and was stirred until the color became brownish color (~16 hr). Then deionized (DI) water (400

ml) was slowly added to the mixture. Subsequently, the suspension was treated with H<sub>2</sub>O<sub>2</sub> solution (20 mL, 30%) turning bright-yellow in color. The resulting solution was centrifuged (6000 rpm for 5 min) and the supernatant was decanted. The pellet was washed with DI water (250 mL), HCl (250 mL, 30%), ethanol (250mL), and finally DI water (200 mL) twice, and then was lyophilized. The lyophilized H-GO was immediately annealed in an argon (Ar) environment at 900 °C for 10 min to produce exfoliated graphene (Ex-G).

### **2.4.3 Scanning Electron Microscopy**

Scanning electron microscopy (SEM) was used to understand the morphology of catalysts and materials synthesized. SEM was used extensively to analyze the structural of metal particles formed on graphene layers for its ability to achieve high magnifications. Also, rough estimate of elemental compositions were identified by using X-ray diffraction and analysis. The electron column focuses electron beam to the specimen using the electron gun (see Figure 10). Secondary and back-scattered electrons, which are produced through interactions between atoms and incident electrons, are produced and detected by the detectors.<sup>136</sup> The image is produced on a cathode ray tube after translating the signals into electrical signals.<sup>137</sup>

Due the source of illumination is not an ordinary light but an electron beam, the condenser lens controls the intensity of the electron beam which controls the brightness. The resolution is controlled by the objective lens by allowing the electrons to flow through the focusing lens which is composed of coils. These foils deflect the electron beam to control the focus to the specimen.<sup>138</sup> The main drawback of this electron microscopy is operation condition in vacuum. Since the flow of charged electrons beam is necessary, the sample chamber requires vacuum.<sup>138</sup>

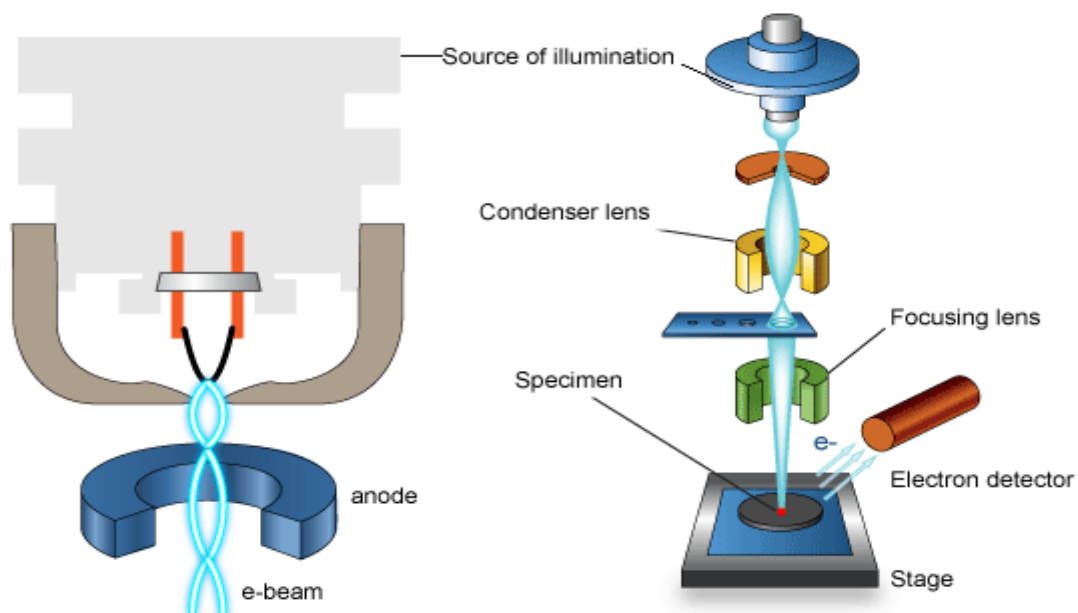


**Figure 10.** Apparatus of scanning electron microscope. Reprinted from [138], Copyright 2013, AMMRF.

The images obtained through this microscopy are collected in grey colours. In this work, SEM to view the uniformity of the nanostructures of synthesized catalysts with graphene as substrates.

#### 2.4.4 Transmission Electron Microscopy

Transmission electron microscopy (TEM) was used to examine the detailed structures of the developed nanomaterials. TEM specially allows the user to characterize lattice and surface structures owing to its ability to draw images at higher resolution than SEM. TEM is used in this thesis to study the features of nanoparticles and other morphology in a lattice scale.

As described in Figure 10, the principle behind TEM is based on electron beam passing through the specimen. The sample is prepared on a mesh grid through which the highly energetic electron beam passes. As the energetic electrons make their way through the grid, some are lost due to the deflection or the absorption made into the specimens on the grid. The passed electrons are collected onto a phosphorescent screen or by a built-in camera.<sup>138</sup> The images are created by unscattered electrons and absorbed electrons depicted as bright image and dark image,

respectively. Besides, some grey parts of an image signify the scatter of electrons during the way through.<sup>138</sup> The electron beam is generated through the electron gun (similar to of SEM) and positioned top of the instrument. In between the electron gun and the phosphorescent screen (or camera), there are sample port to insert the grid holding the sample and apertures, which consists of different sizes of holes that allow modulation of the beam to different degree of precision.<sup>138</sup>

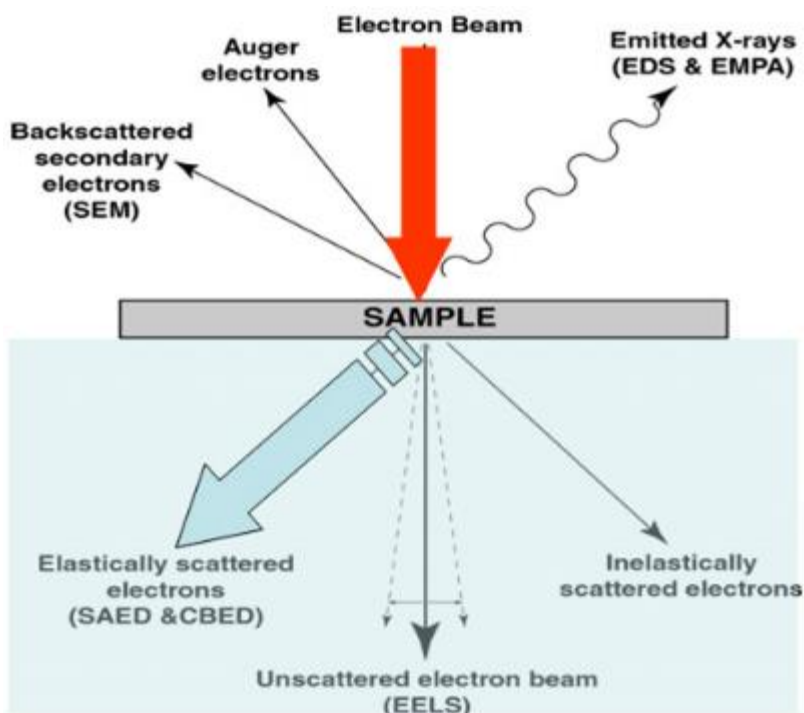


**Figure 11.** Principle behind TEM. Reprinted from [138], Copyright 2013, AMMRF.

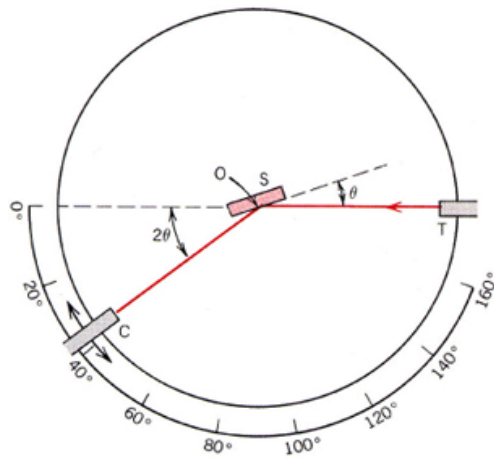
As the holder, where its tip is holding the grid, is inserted into the electron column, the inside is evacuated.

Generally, the function of selected area electron diffraction (SAED) study is carried out during TEM demonstrating its advantage over XRD due to the use shorter wavelength to examine more reciprocal lattice points. In addition, electron energy loss spectroscopy (EELS) can be done by detecting the energy loss of the beam with narrow kinetic energy distribution. As results, information about the elemental composition, valence and bonding, and band structure are

provided through the study. The most commonly used feature of TEM is the high resolution imaging (HR-TEM). HR-TEM can magnify to a specimen up to 0.5nm and allows the user to navigate in its crystallite structure. In this work, HR-TEM is done to distinguish uniqueness of novel catalysts.

#### **2.4.5 X-ray Diffraction**

Powder X-ray diffraction (XRD) is a powerful tool used to study and quantify the crystal structure by measuring the diffraction of X-rays from the planes of atoms of the specimen. XRD provides information about the crystalline content, the crystalline phase, spacing between the lattice plane and the length scales of the material due to its capability to determine the types of relative position of atoms and the length scale of the crystalline.<sup>138</sup> The types of sample eligible for XRD analysis range from inorganic materials, organic materials, polymers, metals and its composites in forms of powder. Also, XRD can be used in study of porous structured materials. In order to describe the material through XRD analysis, elements present in the samples and their arrangements have to be known. Elements in the specimen can be described by a chemical stoichiometry formula and their polymorphs.<sup>138</sup>



## Bragg's Law

$$n\lambda = 2d(\sin\theta)$$

where

$d$  = lattice interplanar spacing of the crystal

$\theta$  = x-ray incidence angle

$\lambda$  = wavelength of the characteristic x-rays

$n$  = the difference in the path length between the adjacent x-ray beam

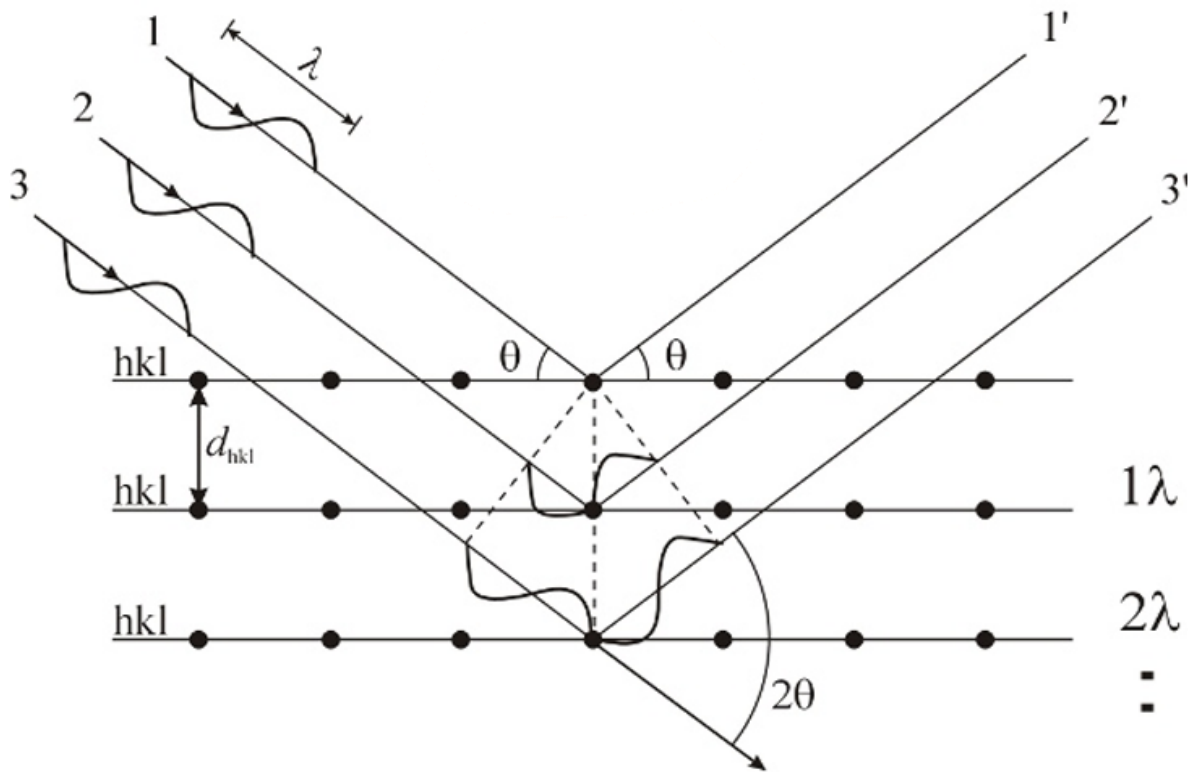


**Figure 12.** Schematic of XRD operation; Bragg Equation and geometry for diffraction of x-radiation.

As described in Figure 12, XRD analyses and detected diffraction rays are governed by Bragg law. The sample is mounted on a goniometer which rotates as the monochromatic X-ray incidents on the surface. As rotates, the angle between the X-ray and the sample changes diffraction of the rays would occur at a specific angle that corresponds to a certain crystalline structure. This angle

is  $\theta$  in the Bragg equation. Through detecting the intensity of diffracted rays at certain angles would allow the user to determine the interlayer spacing of the crystalline structure. Also, diffraction pattern at certain angle provides geometry of the crystalline and its unit cell structures. The crystalline structures of metal particles and the lattice structures of the developed catalysts were studied through XRD analysis. In this work, X-ray used is generated by Copper K- $\alpha$  X-ray radiation that exhibits a wavelength of 1.54 Angstrom.

#### 2.4.6 X-ray Photoelectron Spectroscopy

X-ray photoelectron spectroscopy (XPS) provides information about elemental chemistry at the surface of a sample including their electronic states, surface bond configuration, valence and elemental composition of a sample.<sup>139</sup> The XPS spectra are obtained by detecting the kinetic energies of the electrons emitted from the surface of the sample material when radiated with a beam of X-ray. Electrons that losses energy in traversing the sample are displayed in the spectral background.<sup>139</sup> Abiding to the law of energy conservation, the photoemission to electrons occupying different energy state is described as following equation<sup>136</sup>:

$$E_{hv} = E_k + E_\phi + E_B(i) \quad (11)$$

where  $E_{hv}$  is photon energy from X-ray which can be determined by Planck's equation:

$$E_{hv} = h\nu \quad (12)$$

where  $h$  is the Planck's constant and  $\nu$  is the frequency of the X-ray photon.  $E_k$  is the kinetic energy measured by electron energy analyzer scanning the kinetic energy spectrum.  $E_B(i)$  represents the electron binding energy of the  $i$ -th level.<sup>136</sup> Thus, the binding energy can be obtained with assuming or with known value of  $E_\phi$ , which is the correction for the solid effects.

Understanding this principle, XPS is used to analyze the surface chemistry of developed catalysts. In the present study, XPS analysis will be carried out on non-precious metal catalyst on nitrogen doped graphene substrate. This is in order to determine the state of non-precious metals and nitrogen functional groups present on the surface of these catalysts.

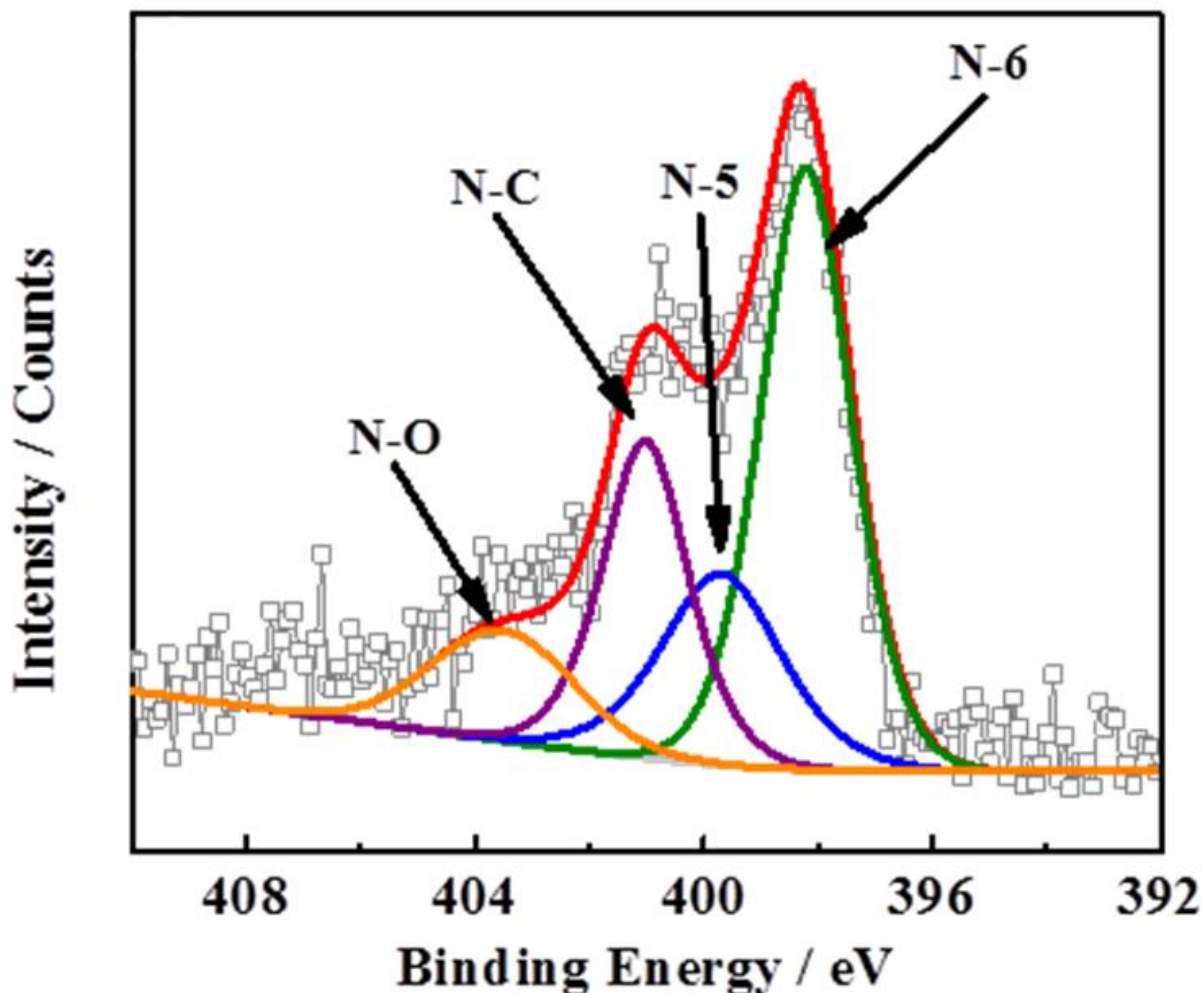


**Figure 13.** HR-XPS analysis of a typical N-doped graphene.

Furthermore, high resolution XPS (HR-XPS) is conducted on the nitrogen, carbon, and metal peaks to study the different the functional groups present. Commonly, representative nitrogen groups exist within the nitrogen spectra distinguished by their specific binding energies (see Figure 13). These binding energies are identified through deconvolution of the HR-XPS peak for

nitrogen: about 398.6 eV for pyridinic (N-6)<sup>140-142</sup>, 400.0-400.6 eV for pyrrolic (N-5), 401.1-401.7 eV graphitic (N-G), and 402.0 – 405.0 eV for oxidized-N (N-O).<sup>102, 143-144</sup> Such as shown, other atomic contributions to its elemental analyses can be quantitatively determined based on the library of studied binding energies for different binding energy levels.

### **2.4.7 Raman Spectroscopy**

Raman spectroscopy is a characterization method to provide information about the vibrational and rotational modes of a material. This spectroscopy offers qualitatively measurement of the degree of defects in the pristine graphene layer caused by presence of heteroatoms. Raman spectroscopy technique is based on inelastic scattering of monochromatic laser light.<sup>145</sup> The interaction between the laser beam and the sample leads to deformation of molecules which produces vibration with characteristic frequency. The frequency of the vibration causes light emission of three different frequencies: Rayleigh scattering, Stokes frequency, and Anti-Stokes frequency. After excited by the laser, molecules return back to their original vibrational state, which then the excess energy is emitted in the form of light with the same frequency. The sample is illuminated by the excitation source (UV or Vis), and the scattered light is collected with a lens, which also goes through spectrophotometer to obtain Raman spectrum.<sup>145</sup> The light energy translated by spectrophotometer is plotted on the Raman scattering intensity to the wavenumber, which each Raman band contributes to the shift in light energy. In the present work, Raman spectroscopy is used to characterize the defects caused due to doping heteroatoms (N and S) to graphene layer.

## 2.4.8 Half-Cell Electrochemical Analysis

Performances of developed catalyst are evaluated using half-cell electrochemical tests. Electrochemical tests provide easy and simple methods to screen the redox reactions that occurs either side of electrodes. Herein, rotating disk electrode (RDE) voltammetry was employed to test different sets of electrochemical methods such as *cyclic voltammetry* and *linear sweep voltammetry*. Figure 14 shows a typical setup of RDE with each apparatus. Electrolyte is contained in a three-neck flask. The electrolyte provides a phase through which charges are carried by the movement of ions.<sup>47</sup> The electrolyte is purged with either oxygen (O<sub>2</sub>) or nitrogen (N<sub>2</sub>) depending on the purpose of the voltammetry. The working electrode (RDE) is the electrode where half-cell reaction occurs, which consists of a glassy carbon that is 5 mm of its outside diameter held by Teflon material. The Teflon, being absolutely hydrophobic, helps to retain the catalytic ink during coating. The electrode fixed with the rotating motor, which its rotation speed could be controlled. Reference electrode is used to standardize the other half of the cell, which consists of phases having constant composition.<sup>47</sup> Widely used reference electrode include: standard hydrogen electrode (SHE), saturated calomel electrode (SCE), and silver-silver electrode (Ag/AgCl).<sup>47</sup> SHE has all components at unit activity (Pt/H<sub>2</sub> (a = 1) / H<sup>+</sup> (a = 1, aqueous), which slashes represents a phase boundary.<sup>47</sup> SCE is more commonly used as reference which exhibits 0.242 V (vs. SHE) owing to its referential reaction of (Hg/Hg<sub>2</sub>Cl<sub>2</sub>/KCl saturated in water). Ag/AgCl reference electrode is also widely employed which conveys 0.197 V (vs. SHE) owing to its referential reaction of (Ag/AgCl/KCl saturated in water).<sup>47</sup>

On the contrary, pure platinum wire is used as the counter electrode. All three electrodes are connected to a potentiostat that controls the RDE system by adjusting voltage and reads the current from the working electrode. The mentioned catalyst containing ink is prepared prior to

RDE voltammetry using a hydrophobic binder in ethanol solution. Then, the mixture was sonicated to obtain admirable dispersion.

In this work the RDE voltammetry was carried out following the described setup. The RDE voltammetry used to measure the electrocatalytic activity used alkaline electrolyte (0.1 M KOH). All RDE voltammetry were performed at room temperature using a Saturated Calomel Electrode (SCE) as a reference electrode. A glassy carbon electrode (5 mm OD) was coated with 20  $\mu\text{L}$  of 4  $\text{mg mL}^{-1}$  catalyst suspension made by mixing catalyst and a 0.5 wt.% of binding solution, Nafion, in ethanol is used as the working electrode leading to an electrode loading of 0.4  $\text{mg cm}^{-2}$ . The ORR activities were measured from 0.1 to -1.0 V at a scan rate of 10  $\text{mV s}^{-1}$  with  $\text{O}_2$ -saturated electrolyte under various rotation speeds (representatively, 100, 400, 900, 1600 rpm). The use of rotating disk as the electrode allows a laminar flow of electrolytes which promotes the dissolved reactants to the surface of the RDE electrode. In addition, the ORR polarization curves are background corrected by subtracting the currents obtained under the same testing conditions in Ar-electrolyte. Pt-C was tested as the comparison under the same conditions and the loading.

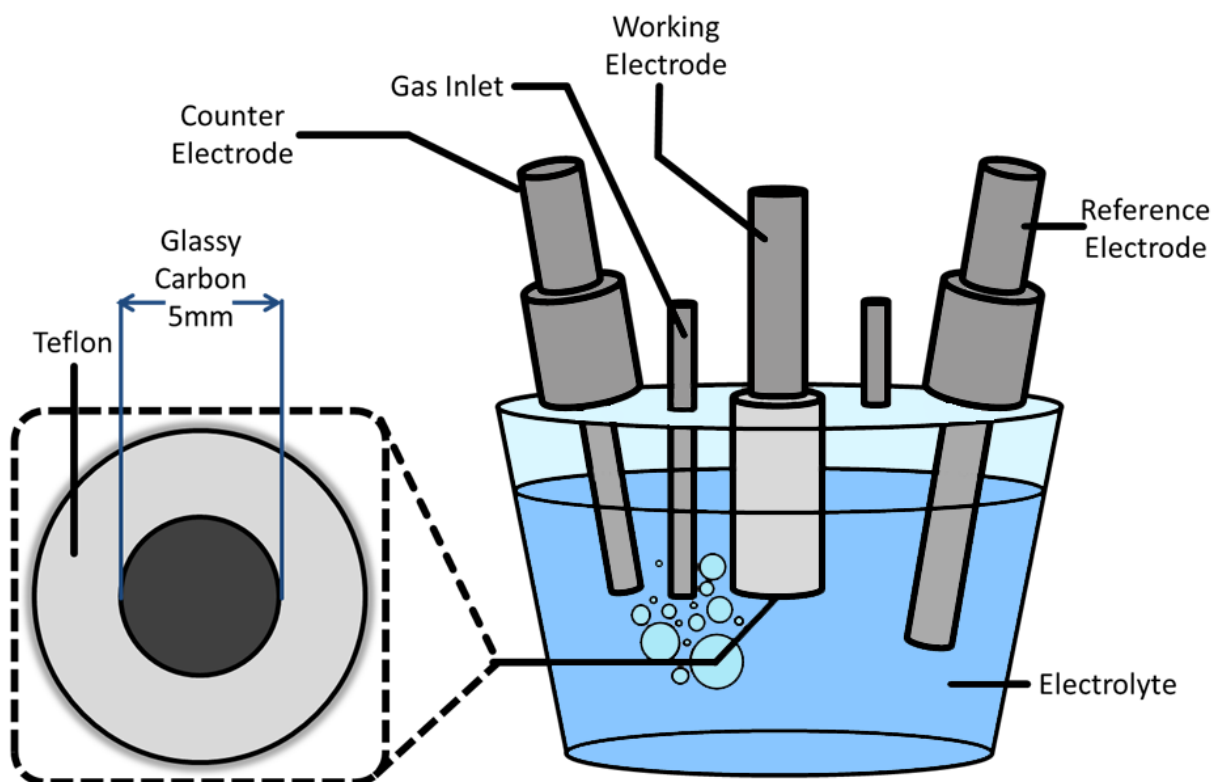


**Figure 14.** RDE voltammetry setup and RDE electrode schematic.

Mainly, two types of electrochemical protocols were carried out using the RDE setup. First, cyclic voltammetry (CV) was carried out for potentiodynamic electrochemical measurement. A result of CV is used to identify the capacitance and surface electrochemical species of the catalyst on the working electrode. In the present work, the potential of the working electrode is swept reversely between the boundaries. The potential sweep rate used is  $50 \text{ mVs}^{-1}$  and the electrolyte is purged with nitrogen. The capacitance is determined by calculating the area of the enclosed curves. CV is a reversal technique that is the potential-scan equivalent of double potential step chronoamperometry (i.e. linear sweep voltammetry). Linear sweep voltammetry (LSV) is a technique to measure the current with respect to changing potential per interval of time. In the case of measuring ORR activity, as the sweep goes from positive to negative with the starting potential at a positive of the standard potential for the given reduction reaction,

nonfaradaic current flows until the potential approaches the standard reduction potential at the working electrode.<sup>47</sup> During this region of potential is controlled by kinetics of the reaction. As the potential approaches the near the standard potential, reduction reaction begins to occur and the current will start to flow, which will be plotted simultaneously by the software. As the potential drop continues, the oxygen concentration at the surface will drop leading to flux increase to the surface as well as the current.<sup>47</sup> During this drop, the current is controlled by both mass transfer of oxygen and kinetic limitation of the overall rate of reaction for the catalyst. Continuously, as potential moves away from the standard reduction potential, the surface concentration drops nearly to zero which the maximum mass transfer of oxygen has reached its maximum rate and the depletion effects sets in.<sup>47</sup> Therefore, current at this region of potential range is limited by the mass transfer of the oxygen to the surface. The above descriptions are shown in Figure 15 by the ORR polarization curve of a catalyst under four different rotation speeds.

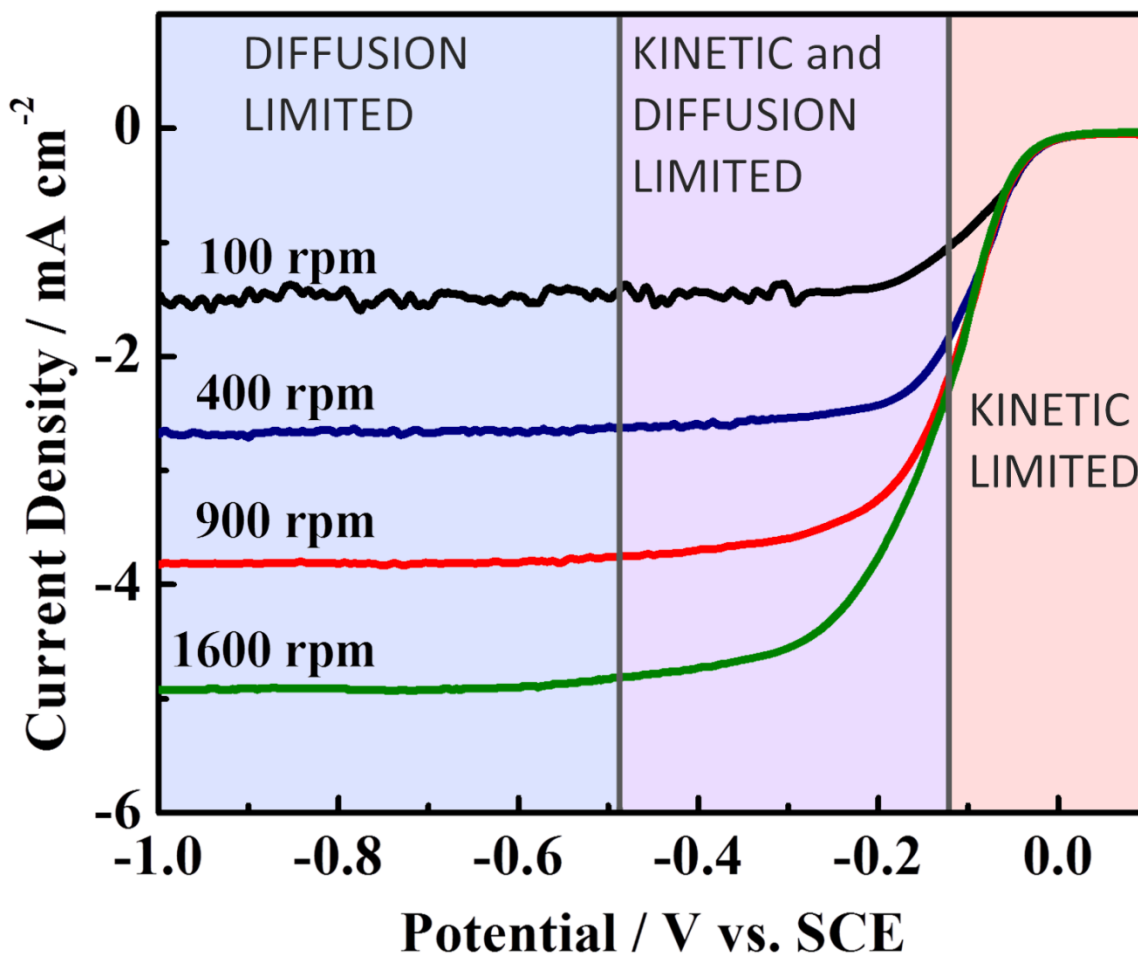


Figure 15. ORR polarization of an active catalyst.

Furthermore, the Koutecky-Levich (K-L) equation is incorporated in studying the kinetics of ORR. K-L plots are used to determine the number of electrons transferred at the surface of the electrocatalyst. The observed current density ( $j$ ) is used to relate to the kinetic current ( $j_k$ ) and limiting current density ( $j_L$ ) by:

$$\frac{1}{j} = \frac{1}{j_k} + \frac{1}{j_L} \quad (13)$$

Abiding to the Koutechy-Levich equation, the number of electrons transferred per O<sub>2</sub> molecule,  $n$ , is calculated:

$$j_L = 0.2nFD_o^{2/3}\nu^{-1/6}C_o\omega^{1/2} \quad (14)$$

In the above equation,  $j_L$  is the limiting current density,  $F$  is the Faraday constant (96 485 C mol<sup>-1</sup>),  $D_o$  is the diffusion coefficient of O<sub>2</sub> (1.9 x 10<sup>-5</sup> cm<sup>2</sup> s<sup>-1</sup>) in 0.1 M KOH,  $\nu$  is the kinematic viscosity of 0.1 M KOH (0.01 cm<sup>2</sup> s<sup>-1</sup>), and  $C_o$  is the concentration of O<sub>2</sub> in the electrolyte (1.2 x 10<sup>-6</sup> mol cm<sup>-3</sup>).<sup>146</sup> At different ORR potentials with various rotating speeds,  $\omega$  in rpm, the ideal number of electrons transferred should be close to 4.0 (refer to equation 1), which leads to assumption that a four-electron reduction of oxygen pathways is in preference during the cathodic reaction.

In the case of positive potential sweep, high concentration of oxidizable anion radicals of oxygen is present at the surface. As the potential grows towards positive direction passing through the standard potential, the anions become re-oxidized and corresponding anodic current is observed. During the positive shift of potential, electrochemical balance at the surface grows towards favouring the formation of neutral oxygen species.<sup>47</sup> The catalysts in the present study is further studied

#### **2.4.9 Zinc-Air Battery Performance**

The application that the development of electrocatalyst in this work leads to is zinc-air battery. All air electrodes used in this zinc-air full cell test are prepared by spraying the catalyst on to a gas diffusion layer (GDL) (Ion Power Inc., SGL Carbon 10 BB. 2.5 cm × 2.5 cm) to achieve a catalyst loading of 0.5 mg<sub>catalyst</sub>/cm<sup>2</sup>. The electrolyte used in the zinc-air battery was 6 M KOH, and a polished zinc plate was used as the anode. The assembled design of the battery prototype is shown in Figure 16.



**Figure 16.** Assembled prototype of zinc-air battery.

As shown by the figure, the prototype of a zinc-air battery is pillared with four plexiglass pieces holding the main components together, tightened with screws at each corner. A hole is created at the centre of each plexiglass piece for access of air from the atmosphere and for the contact between the electrodes and the electrolyte. Gaskets are put in between each plexiglass to retain the electrolyte within the cell by preventing leakage from the side. Next to each electrode (zinc plate and backside of GDL), stainless steel meshes are inserted as current collectors for performance analyses through galvanodischarge test.

The galvanodynamic test was done with multichannel potentiostat (VersaSTAT MC, Princeton Applied Research, U.S.) with current densities varying from 0 to 200mA to measure the discharge performance of batteries. The galvanodischarge curves of zinc-air batteries were recorded at  $50 \text{ mA cm}^2$ .

### 3.0 Effects of Iron and Nanoshell Composites on N-Doped Graphene

Reprinted with permission from ACS, Copyright 2013.

Bae Jung Kim, Dong Un Lee, Jason Wu, Drew Higgins, Aiping Yu, Zhongwei Chen. Iron- and Nitrogen-Functionalized Graphene Nanosheet and Nanoshell Composites as a Highly Active Electrocatalyst for Oxygen Reduction Reaction. *Journal of Physical Chemistry C*. (2013)

#### 3.1 Purpose

Currently, Pt-based catalysts are considered the best oxygen reduction reaction (ORR) catalysts; although Pt is extremely expensive and susceptible to volatile market prices. Thus, there is increasing demand for replacing Pt with more abundant metals due to the scarcity and high price of this noble metal.<sup>3-5</sup> To remedy these drawbacks, the development of an efficient and durable electrocatalyst as a promising renewable energy to replace expensive precious metal based catalyst for the future is absolutely necessary. Promising candidates for substituting Pt based electrocatalyst for ORR are transition metal-nitrogen complexes on carbon support of which the exact identity of the active site remains a subject of debate<sup>147</sup>, despite being consistently demonstrated to provide reasonable catalytic activities towards the ORR.<sup>147-150</sup> Particularly, it is conceived that Fe-containing catalysts have higher ORR activity than those containing other non-precious metals due to its ability to undergo a four-electron transfer process during ORR.<sup>5, 150</sup> For the Fe metals to effectively catalyze the ORR, nitrogen (N) species need to be present, potentially forming metal-nitrogen-carbon or nitrogen-carbon complexes, which can easily be done by a simple pyrolysis process.<sup>150-151</sup> In this chapter, Fe is chosen as a non-noble metal in combination with heterogeneously doped nitrogen atoms to develop an efficient ORR catalyst as an inexpensive and commercially viable electrode material for Zn-air battery applications.<sup>5, 152</sup> Fe-NG was synthesized as an ORR cathode catalyst by a simple thermal treatment using urea to efficiently functionalize the graphene layers. These precursors are physically mixed in a mortar,

simplifying the process and eliminating the drying step necessary in cases where the precursors are combined in a solvent.<sup>3, 102, 143-144, 152-154</sup> Upon pyrolysis, graphitic nanoshells were produced encapsulating metal based nanoparticles, whereby it is expected that the large degree of edge plane exposure present in these nanoshells contributes to the excellent ORR activity demonstrated through half-cell testing and in a full-cell zinc-air battery.

### **3.2 Experimental Methods**

The composite catalyst of Fe-NG was prepared using Ex-G as the starting material. Ex-G is synthesized prior to this step (refer to section 2.4.1). Ex-G (50mg) and urea (2 g) was mechanically grounded until no evidence of urea particles. Subsequently, iron(II) acetate was added to the above mixture and ground. Then the powdered mixture was placed in a quartz tube under Ar environment that was loaded outside of a heating zone of the horizontal tube furnace. With 100 sccm flow rate of Ar, the furnace was heated to 900 °C, after that the position of the quartz tube was manually shifted along the horizontal furnace to bring the powdered mixture to the heating zone. At this point, iron deposited nitrogen doped graphene (Fe-NG) was produced. The sample names were referred as Fe-NG-5-b, Fe-NG-30-b, Fe-NG-50-b, and Fe-NG-100-b based on the amount of iron in the mixture (5 mg, 30 mg, 50 mg, and 100 mg, respectively), and -b (indicating before the post treatment). This step-wise increase in temperature allowed urea decomposition of which doped nitrogen into graphene layer

Fe-NG (20mg) was acid washed in dilute H<sub>2</sub>SO<sub>4</sub> (0.5 M, 50 mL) by dispersion in an ultrasonication bath for 30 min. Then, the mixture was heated at 85 °C for 5 hours under a reflux. The mixture was washed with DI water (1 L) via vacuum filtration using polycarbonate filter paper (Millipore, 0.8µm). The filtrated Fe-NG was re-dispersed in DI water and lyophilized.

Subsequent annealing was carried out in the same way as described above to afford Fe-NG. This treatment was effective in removing some inactive metal species.

### 3.3 Results and Discussion

#### 3.3.1 SEM and TEM: Structure and Morphology

The final Fe-NG materials were produced by a post treatment process of Fe-NG-b (b indicates before treatment), which consists of acid washing followed by a second pyrolysis. The morphological change from Fe-NG-b to Fe-NG is clearly observed by SEM characterization.

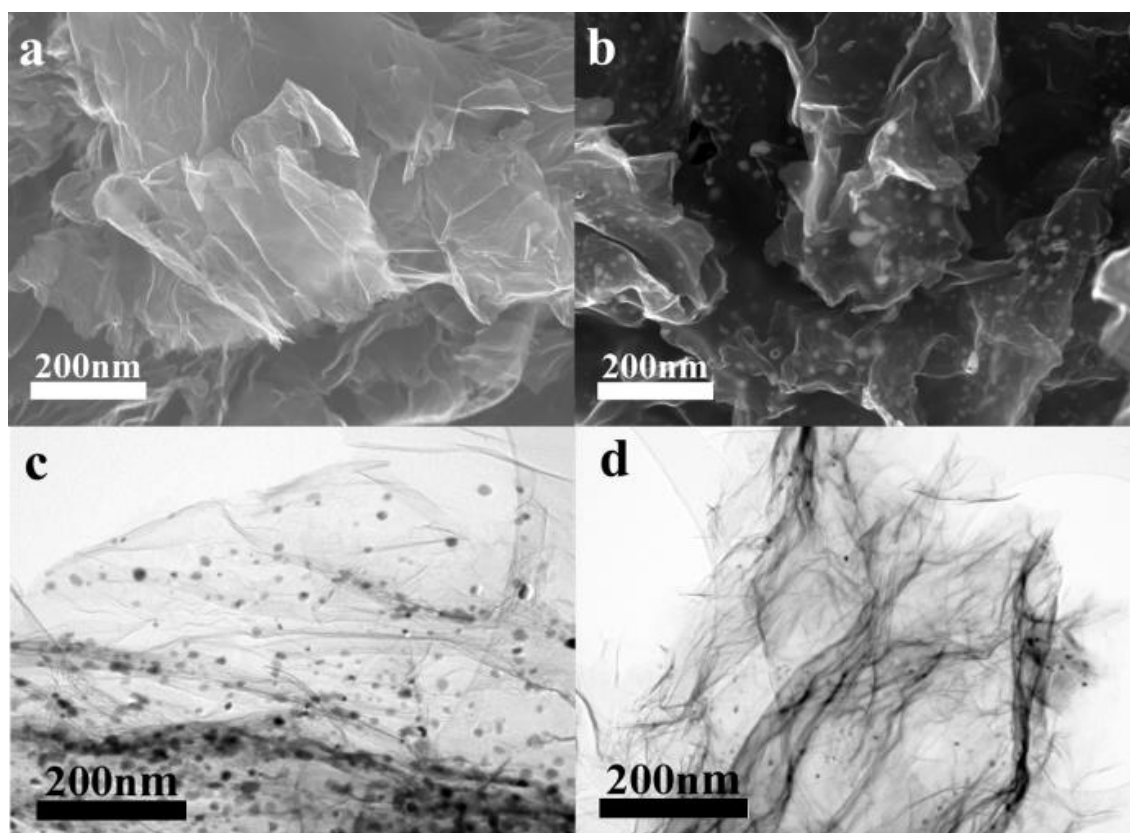


**Figure 17.** SEM and TEM images of Fe-NG and its derivatives. SEM images of a) Ex-G; b) before-post treatment Fe-NG (Fe-NG-30-b); and TEM images of before and after post treatment of Fe-NG: c) before-; d) after post treatment.

Figure 17a shows SEM image of the starting carbon material, Ex-G. The use of urea and iron(II) acetate facilitated N-doping along with the formation of iron nanoparticles in Fe-NG-b (Figure

17b), with the latter observation commonly reported for heat treated iron-based catalysts.<sup>102</sup> After the post treatment of Fe-NG-b with H<sub>2</sub>SO<sub>4</sub> (0.5 M) and annealing for a second time at 900 °C, Fe-NG is observed to maintain the voile-like morphology of graphene sheets while both the number and size of Fe aggregates have significantly decreased (Figure 18a). The presence of oxygen containing functional groups on the surface of the starting exfoliated graphene materials allows Fe species to be adsorbed onto the surface by the negative net charge at the surface.<sup>71, 149</sup> Meanwhile, the Ex-G interacts with the nitrogen species from urea allowing N-doping into the defected plane.<sup>102-103</sup> These doped-N sites could potentially coordinate with Fe-ions in a Fe-N complex arrangement based on this high content of pyridinic nitrogen indicated by XPS (discussed later), a species that resides on the edge plane structures of NG.<sup>150, 155</sup> Particularly, the presence of these edge plane sites is advantageous as they are known to provide catalytic site for reduction of oxygen.<sup>148, 156</sup> Similar to the SEM analysis, TEM images of Fe-NG revealed a wrinkled surface morphology characteristic of nitrogen doped graphene nanosheets, along with well-distributed dark spots representing Fe nanoparticles,<sup>155, 157</sup> albeit present with decreased quantity and sizes after post-treatment. Unnecessary Fe species were removed during this step enhancing the level of exposure of catalytic sites that could assist in improving the ORR activity. High resolution TEM images of Fe-NG shows graphitic edges surrounded by irregular nanoshell features (Figure 18b). The encapsulation is reported to be promoted during the formation of Fe nanoparticles along with the graphitization (Figure 18c).<sup>154-156, 158-159</sup> The presence of nanoshells is commonly observed from acid leached catalysts owing to the removal of iron nanoparticles (Figure 18d).<sup>154-155, 158-159</sup> Figure 18d clearly shows a hollow nanoshell formed by the removal of a nanoparticle. This suggests that some Fe complexes that were incompletely encapsulated by graphitic layers have dissolved during the acid treatment. The shell structured graphitic layers are

tightly packed where the interlayer distance of each lattice was revealed to be ca. 0.34 nm. High resolution TEM images of an occupied nanoshell (Figure 18c) shows some Fe nanoparticles were well protected from acid leaching by the graphitic layers.<sup>154-155</sup> The presence of the ridges of the shells increases the degree of edge exposure of the graphene, which is most likely to result in improved ORR performance due to the increased exposure of sites responsible for oxygen adsorption.<sup>151</sup>

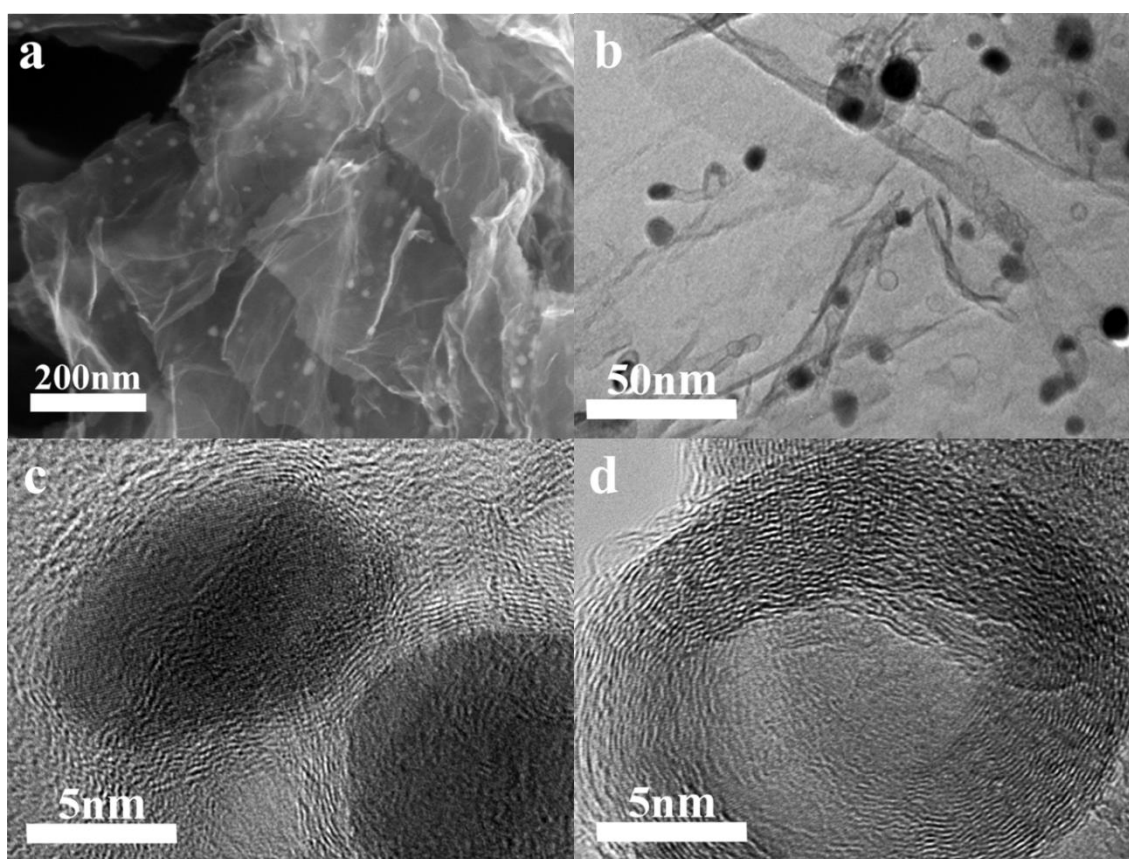


**Figure 18.** SEM and TEM images of after post treatment of Fe-NG. a) SEM image of Fe-NG-30 after the post treatment showing decreased amount of Fe particles. b) TEM image of Fe-NG-30 revealing both hollow and Fe nanoparticle occupied nanoshells. c) High resolution TEM (HR-TEM) image of Fe nanoparticle occupied nanoshells. d) HR-TEM image of the hollow nanoshell.

### 3.3.2 XRD Analysis

The crystalline structure after the post-treatment from Fe-NG-b to Fe-NG does not change as characterized by the X-ray diffraction (XRD) pattern (Figure 19a). XRD patterns of the post-treated product shows a peak (marked with  $\diamond$ ) at  $26.3^\circ$ , identified as the 002 peak of N-doped graphene sheets.<sup>3, 143, 158</sup> This pattern corresponds to the crystalline graphite structure, which is an indication that the graphene layers are maintained after the thermal treatment. The d-spacing calculated using the 002 peak is  $3.39 \text{ \AA}$  consistent with typical d-spacing of heat treated N-doped graphene sheet reported previously.<sup>143</sup> The high intensity of the  $\diamond$  peak compared to reported graphene sheet signifies the existence of turbostratic carbon, which are the consequence of the formation of the nanoshells and edges created by the graphitic layers as observed in the TEM images.<sup>154-155, 158</sup> The XRD pattern of Fe-NG exhibits other peaks at  $37.2^\circ$ ,  $39.6^\circ$ ,  $40.6^\circ$ ,  $43.6^\circ$ ,  $44.7^\circ$ ,  $48.7^\circ$ ,  $50.6^\circ$ ,  $54.8^\circ$ , and  $63.2^\circ$  which correspond to the reported crystalline structure of Fe-carbide (marked with  $\nabla$ ).<sup>143, 155, 158</sup> The Fe-carbide peaks are indication that supports images of encapsulated Fe-particles by graphitic layer.<sup>148, 158</sup> The metal precursor has a significant role in shaping and forming the Fe nanoparticles when combined with carbon, promoting graphitic lattice distortion and encapsulation of Fe-nanoparticles. This structure of the formed nanoparticles is important in ultimately aiding to improve the ORR activity. Dodelet et al. have reported the improved fuel cell durability due to the presence of graphitic nanoshells surrounding metal nanoparticles.<sup>151, 155-156</sup> The formation of carbon nanoshells are reported to be promoted by metal nanoparticles acting as seeds, where graphitic structure are formed around it as they are heat treated at  $900^\circ\text{C}$ .<sup>149, 154-155</sup>

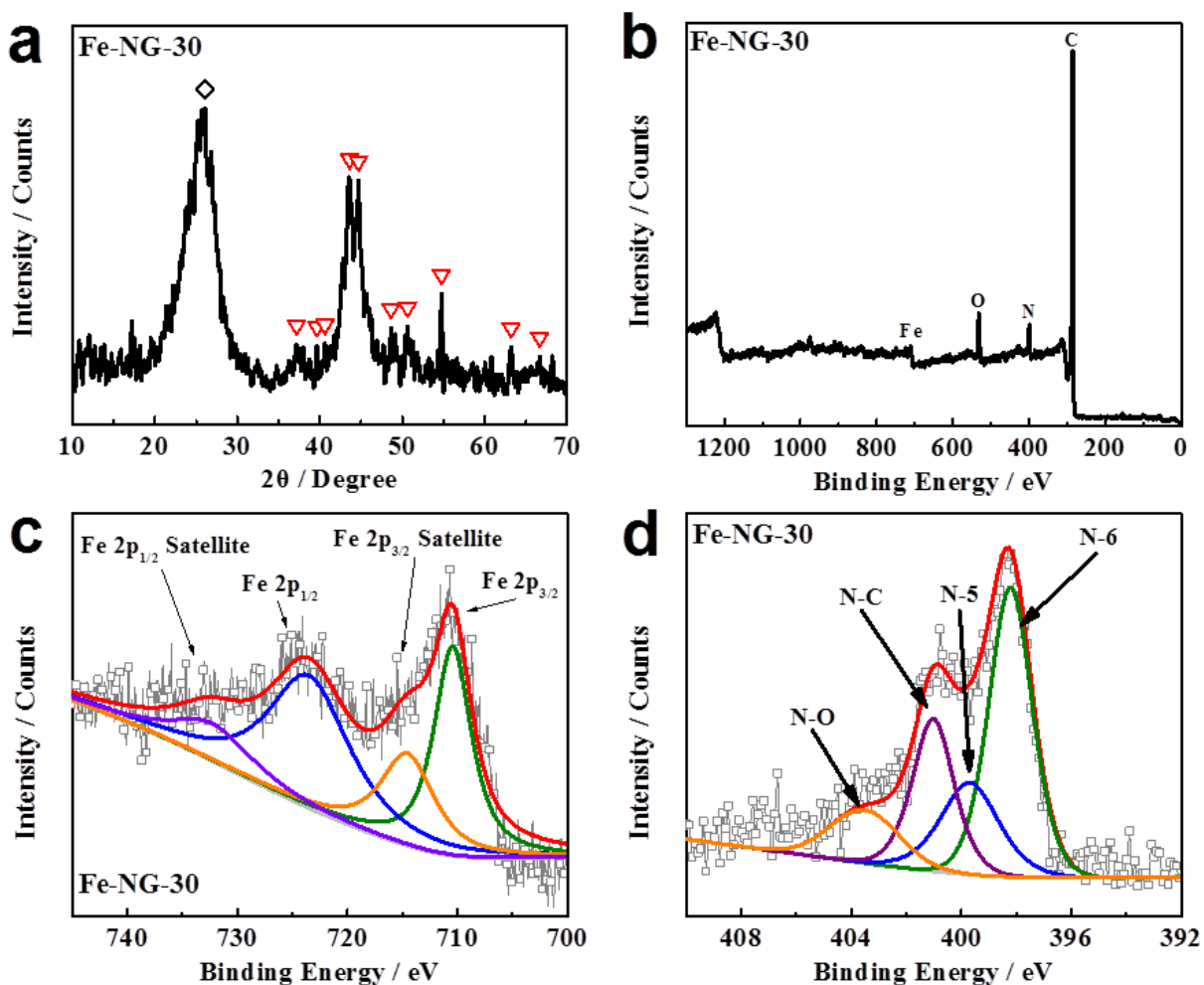


**Figure 19.** Physical and composition analysis of Fe-NG-30. a) XRD analysis of Fe-GN-30. b) XPS survey spectrum of Fe-NG-30. c) HR-XPS Fe-2p spectra. d) HR-XPS N 1s spectra.

### 3.3.3 XPS Analysis

X-ray photoelectron spectroscopy (XPS) is used to analyze the elemental composition of Fe-NG. Figure 19b shows the XPS spectrum survey of Fe-NG with atomic percentages of C, O, N, and Fe of 87.47 at%, 5.83 at%, 5.81 at%, and 0.89 at%, respectively. The high resolution spectrum of Fe-2p of Fe-NG reveals a distribution of Fe-2p into two species: Fe-2p<sub>1/2</sub> and Fe-2p<sub>3/2</sub> observed at 723.88eV and 710.48eV, respectively (Figure 19c), consistent with previously reported Fe deposited carbon materials.<sup>143-144, 160</sup> The spectrum has missing peaks at 706–708 eV corresponding to Fe-2p species in comparison to previously reported XPS results.<sup>143, 161-162</sup> This

suggested that the detection of the residual Fe particles was hindered due to the thickness of the nanoshells. As identified by XPS, the high resolution of N-1s spectrum of Fe-NG reveals four different configurations of N-species: pyridinic- (N-6), pyrrolic- (N-5), graphitic- (N-G), and oxidized-N (N-O) with binding energies of 398.08eV, 399.08eV, 400.78eV, and 403.48eV, respectively (Figure 19d).<sup>102, 143-144</sup> The relative atomic percentage of N-6 species is calculated to be 45.08 % of the total N-species, indicating a high degree of edge plane exposure. A possible pathway for N-doping is by the thermal decomposition of urea into melamine groups (ammelide and ammeline) and carbon nitride during pyrolysis.<sup>102, 163</sup>

### 3.3.4 ORR Performance

The oxygen reduction activity of the synthesized catalyst (Fe-NG-b) is evaluated using rotating disk electrode voltammetry in an alkaline aqueous electrolyte half-cell by comparison to N-doped graphene (NG) that is synthesized using the same procedure but without the addition of Fe-precursor, and thermally exfoliated graphene (Ex-G) (Figure 20a). The carbon precursor, Ex-G, shows insufficient ORR performance alone. N-doping of the Ex-G in the absence of iron showed an improvement in both half-wave and limiting current meanwhile shows poor kinetic and diffusion limited oxygen reduction activity.

Addition of Fe to the NG showed remarkably improved ORR activity from its precursors, NG and Ex-G. Variation in Fe loading was studied to evaluate the optimal amount of Fe (Figure 20b). As shown, Fe-NG-30-b shows the most outstanding ORR activity with an onset potential of -0.050 V (vs. SCE) and a half-wave potential of -0.143 V (vs. SCE) comparable to those of produced in three different Fe loadings: 5 mg, 50 mg, and 100 mg (indicated by the numbers of the name in Figure 20b). Shifts to negative direction in both onset and half-wave potentials are

observed as Fe loading is decreased. Fe-NG-5-b, however, does not follow the trend, showing the onset and half-wave shift towards positive direction of the potentials. The lower loading of Fe indicates a decrease in the formation of nanoparticles, consequently lowering the level of aggregation created.<sup>3, 148</sup> This result suggests that a sufficient Fe-aggregation is needed for the construction of carbon nanoshells, which contributes to efficient ORR activity. The ORR activity evaluated after the acid treatment and the subsequent thermal treatment of Fe-NG-30-b, named as Fe-NG-30, shows further shift to negative direction on both onset and half-wave potential to -0.023 V (vs. SCE) and to -0.110 V (vs. SCE), respectively (Figure 20c).

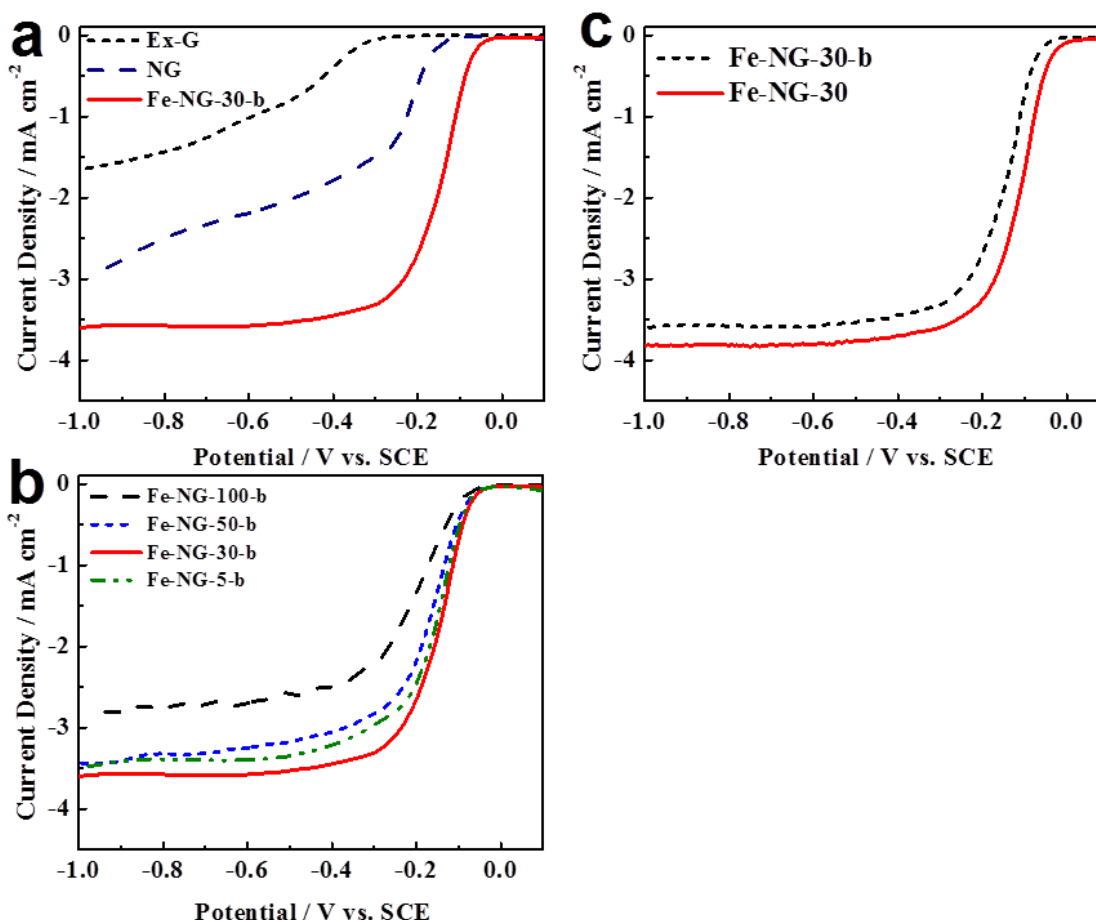


**Figure 20.** Linear sweep voltammetry (LSV) in evaluating oxygen reduction reaction in 0.1 M KOH at a scan rate of 10 mV s<sup>-1</sup>. a) Comparison of ORR performance of Ex-G, NG, and Fe-NG-30-b b) LSVs of Fe-NG with different Fe loadings. c) Improved ORR performance of the catalyst after post treatment of the catalyst.

ORR performance of a typical carbon based electrocatalysts relates to these considerations: (1) starting carbon source<sup>164</sup>, (2) graphene surface affected by N-doping<sup>3</sup>, (3) Fe and N complexes on the surface<sup>154</sup>, (4) graphitic nanoshells either encapsulating metal nanoparticles or in vacancy<sup>151, 154-155</sup>. The shifts in potentials is an indication that a deliberate acid treatment of the synthesized product is important for more accessible to the catalytic sites through the removal of extra Fe nanoparticle aggregates outside the nanoshells. On the contrary, the vacant nanoshells are the result of the post treatment of Fe-NG-b with 0.5 M of H<sub>2</sub>SO<sub>4</sub> and an additional pyrolysis process. Referring to Figure 18c, the incomplete removal of the encapsulated Fe particles indicates that metal particles are completely sealed preserving against acid from leaching out the metal complexes.<sup>154-155</sup> The enhanced ORR performance of the catalyst is attributed to improved electron mobility due to the morphological advantage of the graphitic nanoshells that increases the level of edge site exposure.<sup>164</sup> Thus, the enriched ORR activity after the post treatment, Fe-NG, is clearly demonstrated and evaluated through measuring the shifts in the onset and the half-wave potentials (Figure 20b).

As presented in Figure 21a, enhanced onset and half-wave potentials of Fe-NG-30 shows comparable performance to those of Pt-C in an alkaline electrolyte (onset and half-wave values of Pt-C are -0.021 V (vs. SCE) and -0.120 V (vs. SCE), respectively). Using the ORR polarization curves of Fe-NG at various rotation rates (Figure 21b), Koutechý-Levich (K-L) plots are used to determine the number of electrons transferred at the surface of the electrocatalyst (Figure 21b inset).

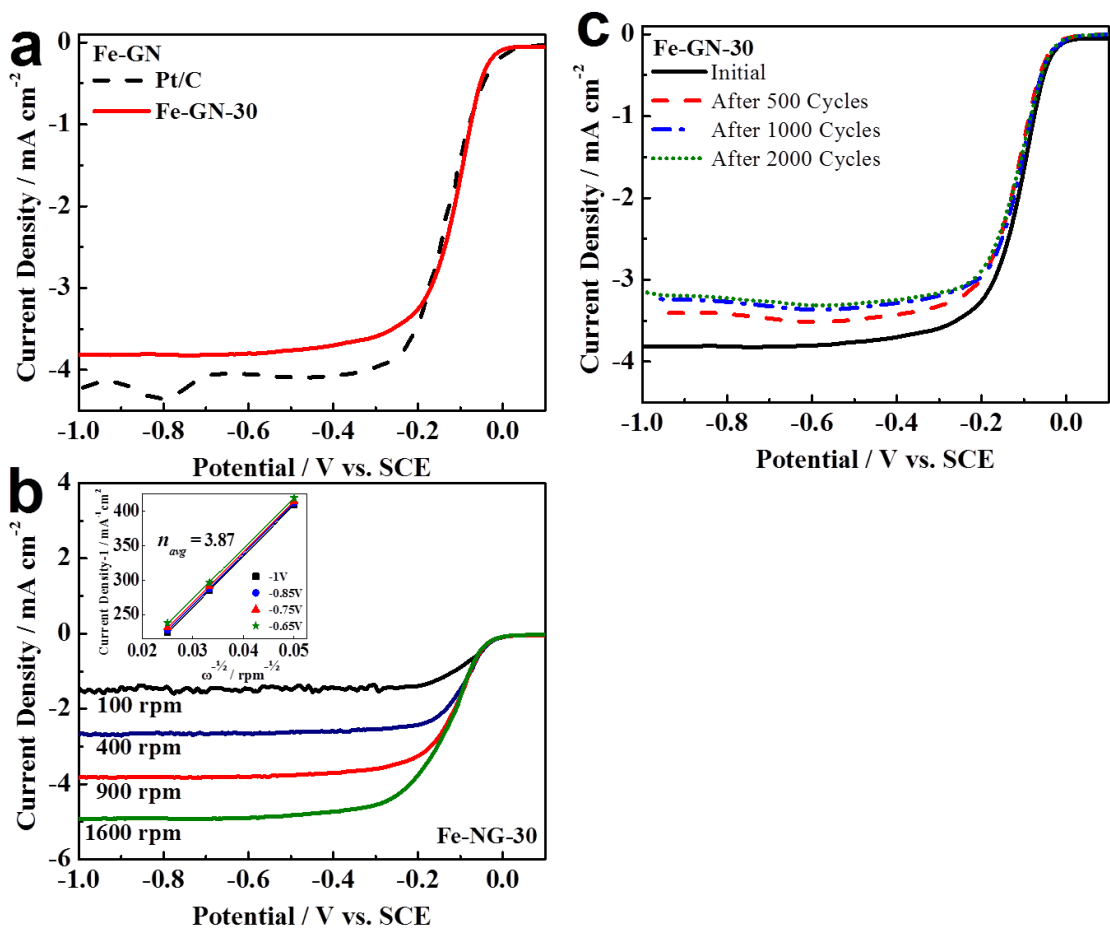


**Figure 21.** Linear sweep voltammetry (LSV) in evaluating oxygen reduction reaction in 0.1 M KOH at a scan rate of 10 mV s<sup>-1</sup>. a) Comparison of ORR performance of Fe-NG-30 and Pt-C b) LSVs of Fe-NG-30 at different rotating speeds (Inset: Koutecky-Levich plot) c) LSVs of Fe-NG-30 after CV cycles.

K-L plot is determined referring to section 2.4.6. As shown in Figure 21b inset, at different ORR potentials with various rotating speeds,  $\omega$  in rpm, the number of electrons transferred was found to be close to 4.0, which suggests a four-electron reduction of oxygen during the cathodic reaction ( $O_2 + 2H_2O + 4e^- \rightarrow 4OH^-$ ). The high selectivity for the four-electron transfer pathway of Fe-NG is attributed to the synergistic active sites created by Fe- and N-species; N-containing graphene typically incorporates Fe- atoms to the graphitic layer, which encourages four-electron transfer pathway at higher ORR potentials.<sup>165-167</sup> In addition to the catalytic sites

promoted through Fe-N complexes, the presence of nanoshells and the constructed edges contributed to the improvement of the ORR activity.<sup>149, 151, 154</sup>

### 3.3.5 Zinc-Air Battery Performance

Elaborating on the electrochemical half-cell analysis of FeNG-30, single-cell zinc-air battery testing has been carried out to confirm the promising results. Figure 22 shows galvanodynamic discharge polarization curve of Fe-NG-30 that demonstrates comparable performance to that of Pt/C accordingly to of their ORR performances. The behaviour of the catalyst illustrates an activation loss region followed by a pseudo-linear ohmic loss region. The activation region is associated with potential loss due to activation barrier that a reactant species must overcome, and the subsequent ohmic loss region indicates the loss associated with electrical resistance of the components. In the air breathing electrode, Fe-G-30 provides performance capabilities approaching that of commercial Pt/C with a peak power density of 61  $\text{mW cm}^{-2}$  (Figure 22).

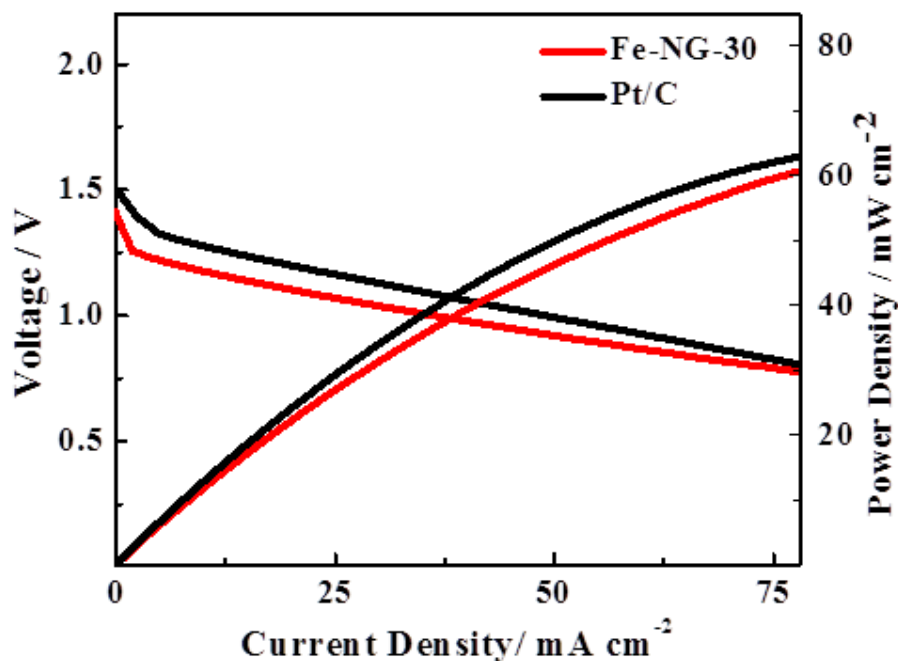


**Figure 22.** Galvanodynamic discharge polarization curve of full-cell zinc-air battery of Fe-NG-30 as its cathode catalyst compared to the cell with Pt/C as its cathode catalyst.

### 3.4 Conclusion

This chapter introduced a simple method to synthesize high performance nitrogen doped graphene based catalyst. Through this work, we were able to establish a simple preparation method through the mechanical mixing of graphene with N and Fe precursors which evolved to become active sites for ORR without the use of solvent and the subsequent drying steps. The present work demonstrates that urea is a suitable N precursor in introducing the dopant to the graphene layer as well as most likely in coordination with metal precursor in forming Fe- N-complexes. Also the pyrolysis of mechanically mix of precursors with graphene at high temperature induces the formation of graphitic shells, and it is speculated that these graphitized carbon nanoshells contribute to ORR performance due to the high degree of edge plane exposure. The synthesized product (Fe-NG-b) was also post treated by acid washing and a second pyrolysis, and the final product (Fe-NG) was found to provide further improved ORR activity. Among different variations of Fe loading, Fe-NG with 30 mg (i.e. 1wt.%) of Fe (Fe-NG-30) demonstrated outstanding ORR kinetics with onset and half-wave potentials of -0.023 V and -0.110 V (vs. SCE), respectively, which were comparable to that of Pt/C. Zn-air battery performance was also evaluated through galvanodynamic discharge test. The catalyst shows proficient performance upon comparing the discharge polarization curve of the catalyst to that of Pt/C demonstrating  $61 \text{ mW cm}^{-2}$  of power density. Overall results suggests further approaches are to be made in analyzing the mechanism of Fe-N along with formation of carbon nanoshells sites are necessary to gain better understanding of behaviours of transition metals for electrocatalysts used in metal air batteries.

## **4.0 Effect of Heteroatoms in Graphene and CNT Composite**

### **4.1 Purpose**

Previous chapter incorporates non-precious metal as to replace platinum, currently the best active ORR catalyst. This approach provides promising ORR activity with a unique morphology of graphene nanosheet modified through the formation of iron particles. This novel structured catalyst helped to enhance the overall cost of metal-air battery system. Yet, further improvements need to be made in terms of the cost and efficiency. As preciously explained in section 2.3, CNT could be introduced as additional substrate next to graphene. Therefore, the chapter focuses on developing efficient ORR catalyst, specifically on the developing functionalized carbon based metal free catalyst. Through atomic modification, CNT and graphene composite offers to be a very electron conductive support material with high affinity towards ORR. Currently, this study has preliminarily investigated the effect of heteroatoms, nitrogen and sulfur, on CNT and graphene composite. Effects of sulfur to carbon as heteroatom have merely been investigated by fuel cell community. Past reports have shown that S-doped graphene demonstrates significant ORR activity, excellent long-term stability, and high tolerance against methanol in alkaline media.<sup>111-112, 168-169</sup> Alongside to nitrogen, introduction of sulfur has demonstrated greatly improved ORR activity in alkaline media. Furthermore, we hypothesize the synergetic effect from the presence of sulfur and nitrogen heteroatoms in CNT and graphene would greatly enhance the ORR activity owing to acknowledgeable ORR affinity of NCNT and N-doped graphene. This chapter discusses about the ORR performance and its potentials as the cathode of metal-air battery of the sulfur added N-doped CNT and graphene composite (GC-NS) at a relatively low temperature.

## **4.2 Experimental Methods**

### **4.2.1 Oxidized Carbon Nanotube**

The CNT is oxidized from commercial multi-walled carbon nanotubes (MWNT) (>50 nm O.D., 10 – 20  $\mu\text{m}$  in length, >95 wt% purity). MWNT (300 mg) was dispersed in 100 mL of nitric acid. The mixture was heated up to 104  $^{\circ}\text{C}$  for 6 hours under a reflux condenser. Then deionized (DI) water (100 ml) was slowly added to the mixture cooled in an ice bath. The solution was centrifuged (6000 rpm for 5 min) and the supernatant was decanted, and the pellet was washed with DI water, repeatedly. Then, the pellet was collected and dried at 60  $^{\circ}\text{C}$  to produce oxidized CNT (O-CNT).

### **4.2.2 Graphene Oxide and Oxidized Carbon Nanotube Composite**

Prior to the synthesis of the composite, graphene oxide (GO) was prepared as outlined in sections 2.4.1. The prepared H-GO and O-CNT (5:1 weight ratio) was added into 10 mL of acetone in a 20 mL vial. The mixture was sonicated for 4 hours under controlled temperature by addition of ice. After, the solution is dried in a petri-dish at room temperature to obtain GO and O-CNT composite (GC).

### **4.2.3 Nitrogen-Doped GC**

Nitrogen-doped GO and O-CNT composite (GC-N) was prepared through CVD method. GC was placed in a quartz tube under mixture of ammonia ( $\text{NH}_3$ ) accompanied by inert gas (Ar) at the centre of a heating zone of the horizontal tube furnace. With 100 sccm flow rate of Ar and 60 sccm flow of  $\text{NH}_3$ , the furnace was heated up to 500  $^{\circ}\text{C}$  at 5  $^{\circ}\text{C min}^{-1}$  and maintained at that temperature for 5 hours. After the temperature has cooled down to room temperature, GC-N was

obtained. The sample names were referred as GC-NL and GC-NH based on the heating temperature (L for low temperature of 500 °C and H for high temperature of 900 °C).

#### **4.2.4 Sulphur-Doped GC-N**

The produced GC-N was mixed with phenyl disulphide (PDS) to produce sulphur-doped GC-N (GC-NS). GC-N and PDS in (1:5 weight ratio) was mechanically grounded until no evidence of PDS particles. Then the powdered mixture was placed in a quartz tube under Ar environment that was loaded outside of a heating zone of the horizontal tube furnace. With 100 sccm flow rate of Ar, the furnace was heated to 900 °C at 5 °C min<sup>-1</sup> and maintained at that temperature for 5 hours. After the temperature has cooled down to room temperature, GC-NS was obtained. The sample names were referred as GC-NLS and GC-NHS based on the heating temperature during the N-doping of GC; only one temperature of 900 °C was used during the sulphur doping.

### **4.3 Results and Discussion**

#### **4.3.1 SEM: Structure and Morphology**

GC-NS is obtained through two step thermal heat treatment, each treatment subsequently introduced nitrogen and sulfur species. The following Figure 23 illustrates coexistence of graphene oxide and O-CNT structure. SEM image clearly shows that O-CNT structure is well maintained and merged together with graphene oxide layers. Consequently, this composite is oxidized form of its carbon allotropes.

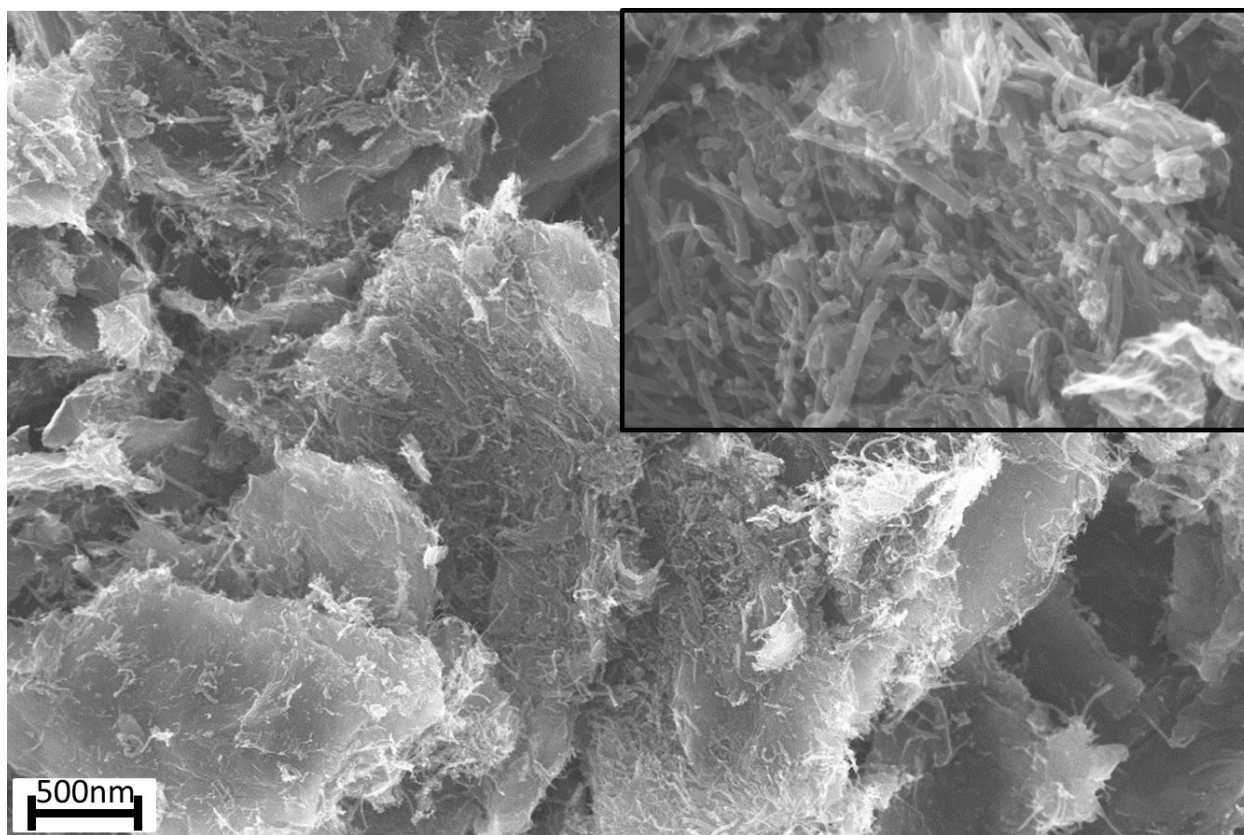


**Figure 23.** SEM images of GO and O-CNT composite.

The composite is doped with nitrogen species simultaneously from ammonia gas as it is reduced. Even after the introduction of the nitrogen species to the carbon composite, the structure of the composite is maintained. Figure 24 reveals SEM image of the nitrogen-doped graphene and CNT composite (GC-N). Nitrogen gas is reported for its wide use as the nitrogen precursor, which has demonstrated its positive effects in quantity of the nitrogen content in carbon materials.<sup>170-171</sup> The resulting GC-N is physically mixed with sulfur precursor, PDS, for final addition of sulfur species. Due to the imperfect reduction of oxygen functional groups during simultaneous N-doping step from the GO and O-CNT composite, GC-N interacts with the sulfur species from PDS allowing S-doping into the defected graphitic network. Figure 25 reveals unchanged morphology of GC-N after S-doping.

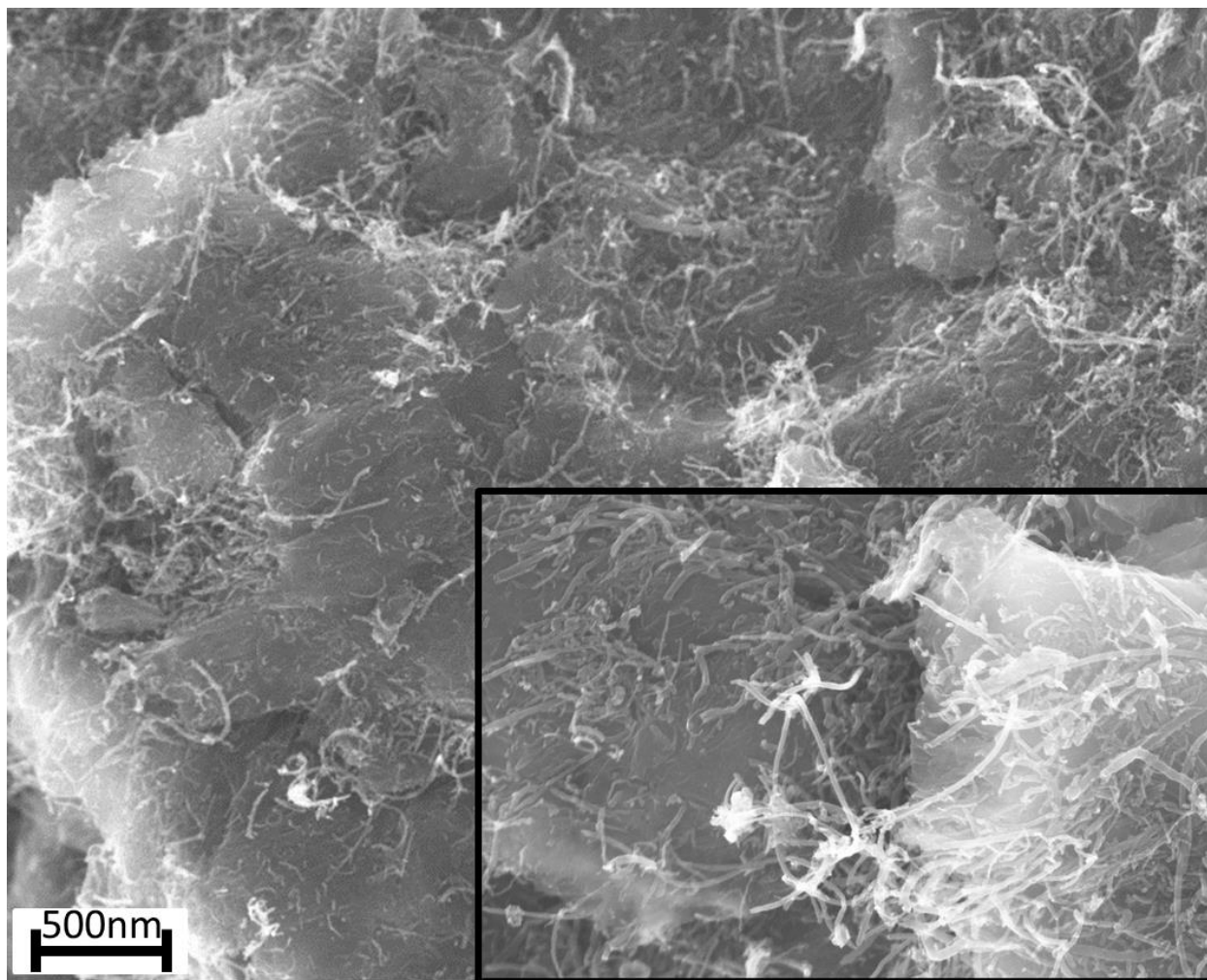


**Figure 24.** SEM image of GC-NL.

The temperature during thermal treatment for N-doping is varied between 500 °C and 900 °C (remarked as L for 500 °C and H for 900 °C). The effect of the thermal treatment temperature during nitrogen in ORR will be discussed later in this chapter. On the other hand, one temperature (900 °C) was used for the sulfur-doping for both GC-NL and GC-NH.

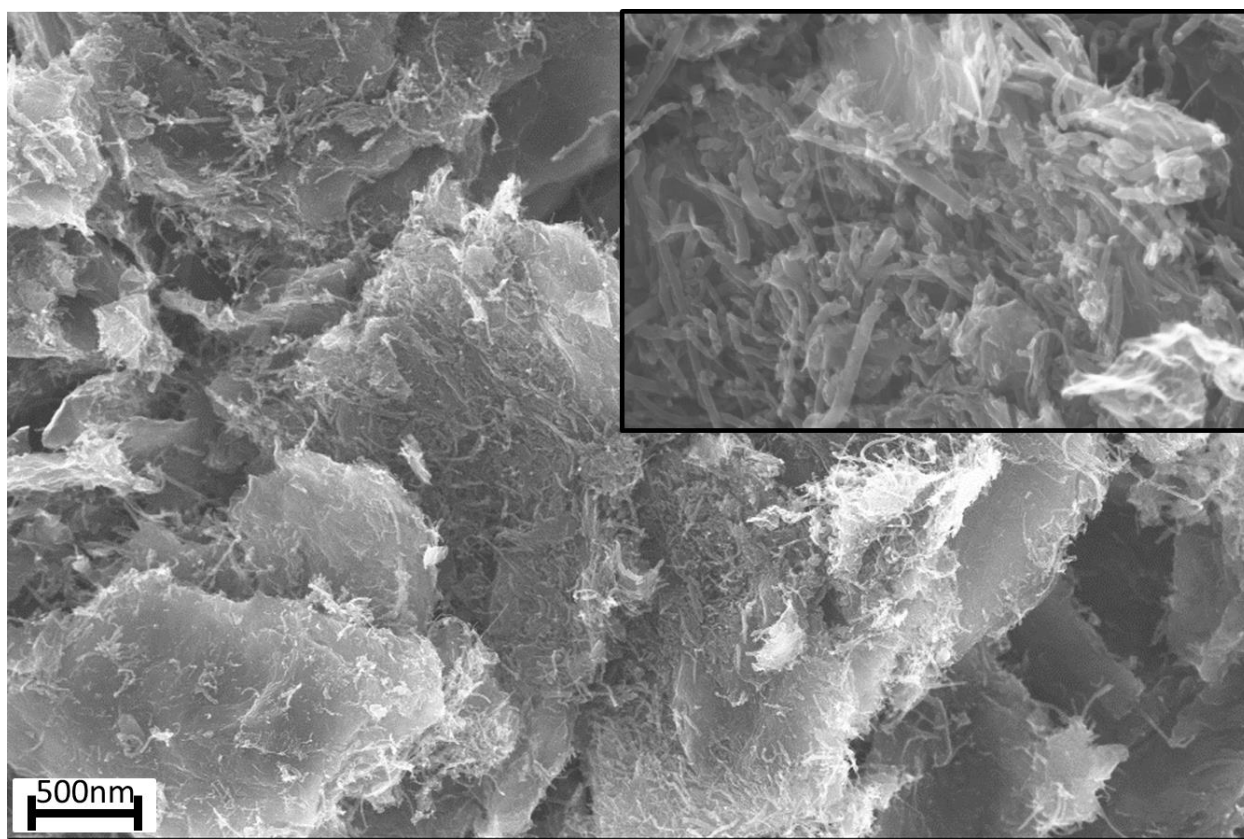


**Figure 25.** SEM image of GC-NLS.

### 4.3.2 XPS Analysis

XPS is used to analyze the elemental composition of GC-NS and its ascendant. Figure 26a shows the XPS spectrum survey of GC-NLS with atomic percentages of C, O, N, and S of 94.54 at%, 3.19 at%, 2.03 at%, and 0.23 at%, respectively. The high resolution spectrum of S-2p of GC-NLS reveals a distribution of S-2p into two species: S-2p<sub>1/2</sub> and S-2p<sub>3/2</sub> observed at 168.68eV and 164.48eV, respectively (Figure 26d), consistent with previously reported S-doped carbon materials.<sup>111, 168-169, 172</sup> As identified by XPS, the high resolution of N-1s spectrum of GC-NLS reveals four different configurations of N-species: pyridinic- (N-6), pyrrolic- (N-5), graphitic- (N-G), and oxidized-N (N-O) with binding energies of 398.58eV, 400.68eV, 401.88eV, and 405.38eV, respectively (Figure 26c). The relative atomic percentage of N-6 species is calculated

to be 45.24 % of the total N-species, indicating a high degree of edge plane exposure. In addition, high resolution of carbon peaks of GC-NLS showed different carbon species (see Figure 26b). As identified by XPS, the high resolution of C-1s spectrum of Fe-NG reveals six different functional groups that are associated with carbon composite substrate: sulfur atom (C-S-C), graphitic (C-C), hydroxyl group (C-OH), oxygen group (C=O), nitrogen (C-N-C), and carboxylic group (COOH) with binding energies of 283.98eV, 284.68eV, 285.48eV, 286.78eV, 287.88eV, and 289.88eV, respectively (see Figure 26b).<sup>111, 168, 172</sup> Among the mentioned functional groups of the carbon species, C-N-C and C-S-C allows quantification of the relative amount of the doped heteroatoms – N and S, respectively. Thus, 9.89 % and 3.89 % of relative atomic percentages relatively contributes to N and S species in the graphitic network. Specifically, structure of present sulfur within the graphitic framework was deduced from the carbon to sulfur interaction shown in HR-XPSs of S-2p and the C-1s to mainly exist in a thiophene-like structure.<sup>172</sup>

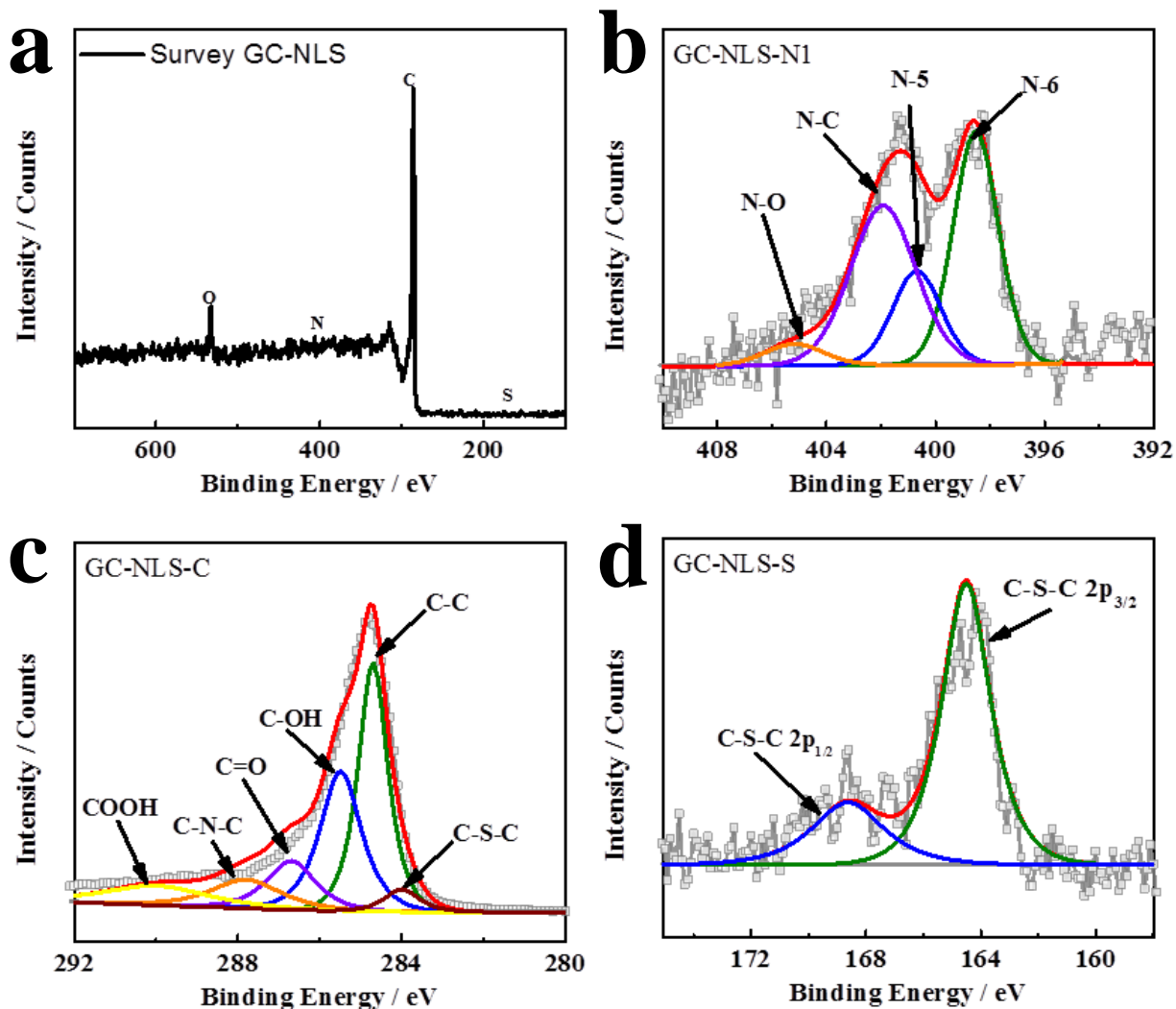


**Figure 26.** XPS analysis of GC-NLS. a) XPS survey spectrum of GC-NLS. b) HR-XPS N-1s spectra. b) HR-XPS C-1s spectra. b) HR-XPS S-1s spectra.

Comparable XPS analyses were carried for GC-NHS, which of GC-NS with the nitrogen was doped at the higher temperature as mentioned in section 4.2.3. Referring to Figure 27a, similar atomic percentages between species were measured with the exception of N. Table 3 shows the comparison of relative atomic percentages of C, O, N, and S from the XPS spectrum surveys between GC-NLS and GC-NHS. (C: 89.43 at%, O: 9.64 at%, N: 0.60 at%, and S: 0.34 at%). The high resolution spectrum of S-2p of GC-NHS reveals alike distribution of S-2p of the two species mentioned – S-2p<sub>1/2</sub> and S-2p<sub>3/2</sub> – observed at 169.08eV and 164.58eV, respectively (see

Figure 27d). On the contrary, XPS results of N-1s spectrum in high resolution did not reveal any of possible N species unlike for GC-NLS. However, the recognizable nitrogen species were observed HR-XPS of N-1s in GC-NH, before S-doping. This suggests disappearance of N-species during the introduction of S-species to the graphitic framework. This phenomenon is also supported by observation made of HR-XPS C-1s spectra (see Figure 27c). The minimal C-N-C relative atomic percentage (3.40 %) indicates low N species within the graphitic network. In Figure 27b, no peaks are observed for GC-NHS compared to its prior ascendant sample, GC-NH. Effects of relative absence of nitrogen in ORR activity is shown in the next section. Tables 3 to 6 show relative atomic percentages between all species for each element of GC-NS.

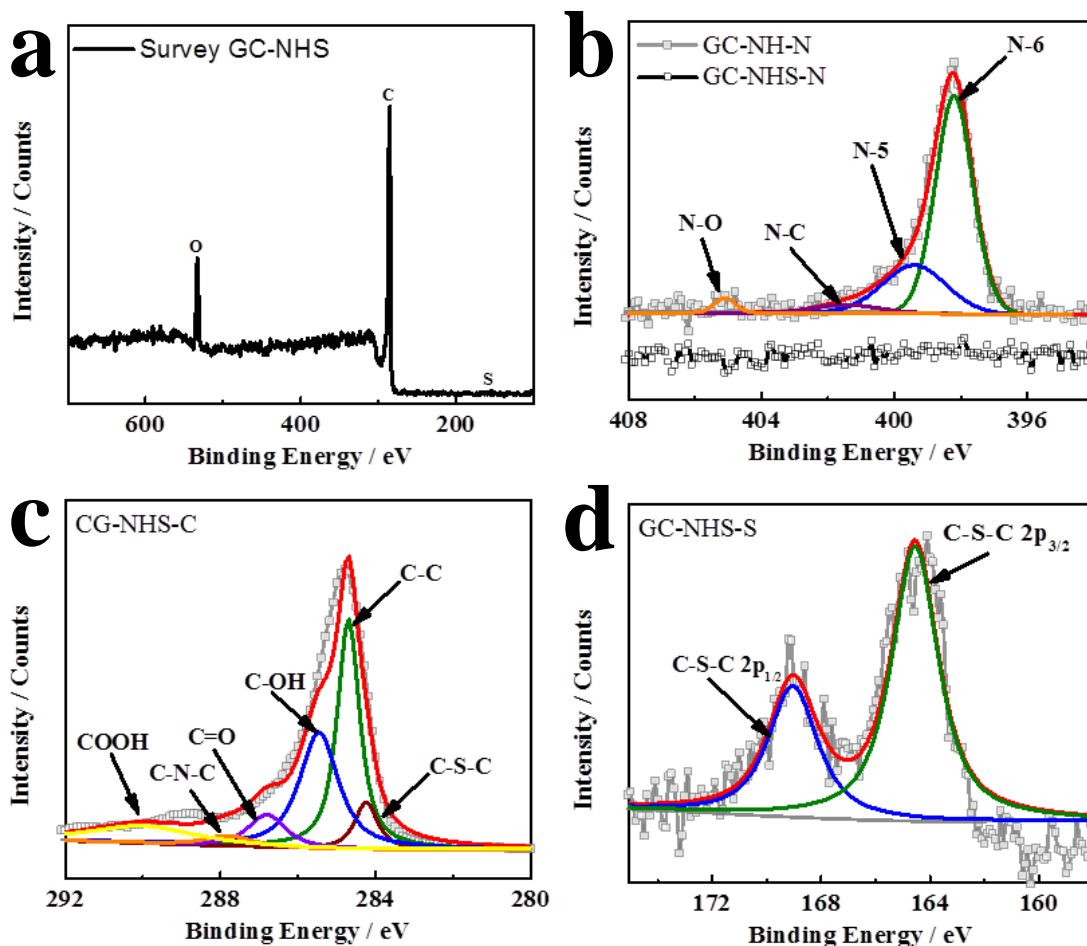


**Figure 27.** XPS analysis of GC-NHS. a) XPS survey spectrum of GC-NHS. b) HR-XPS N-1s spectra. c) HR-XPS C-1s spectra. d) HR-XPS S-1s spectra

**Table 3.** Relative atomic percentage of elements.

Sample	C1s	N1s	O1s	S2p
GC-NL	88.83%	5.75%	5.42%	0.00%
GC-NLS	94.54%	2.03%	3.19%	0.23%
GC-NH	92.36%	3.71%	3.93%	0.00%
GC-NHS	89.43%	0.60%	9.64%	0.34%

**Table 4.** Relative atomic percentage of C-1s species

Sample	C1s					
	C-S-C	C-C	C-OH	C=O	C-N-C	COOH
GC-NLS	3.89%	36.20%	28.24%	11.71%	9.89%	10.07%
GC-NHS	7.51%	36.19%	31.59%	8.51%	3.40%	12.81%

**Table 5.** Relative atomic percentage of N-1s species

Sample	N1s			
	N-6	N-5	N-C	N-O
GC-NL	46.24%	30.97%	14.90%	7.89%
GC-NLS	39.13%	17.00%	39.04%	4.83%
GC-NH	67.62%	25.43%	4.39%	2.55%
GC-NHS	-	-	-	-

**Table 6.** Relative atomic percentage of S-2p species

Sample	S2p	
	2p 1/2	2p 3/2
GC-NLS	24.71%	75.29%
GC-NHS	33.58%	66.42%

### 4.3.3 ORR Performance

The oxygen reduction activity of the synthesized catalyst (GC-NS) is evaluated using rotating disk electrode voltammetry in an alkaline aqueous electrolyte half-cell. First, GC-NL was compared to GC-NH that is synthesized using the same procedure but at different temperature during the heat treatment (Figure 28a). Both nitrogen-doped GC composite synthesized at high and low temperature shows undesirable ORR performance. The onset potentials and half-wave

potentials for GC-NH showed -0.137 V (vs. SCE) and -0.211 V (vs. SCE), respectively; and -0.157 V (vs. SCE) and -0.249 V (vs. SCE), respectively, for GC-NL. Similar onset potential values of GC-NL and GC-NH was revealed, yet, the GC-N synthesized at lower temperature demonstrated more promising limiting-current compared to that of GC-NH (Figure 28a). Subsequent sulfur doping of GC-NL, which produced GC-NLS, demonstrated improved ORR activity from its precursor, GC-NL (Figure 28b). As shown, GC-NLS shows the most outstanding ORR activity with an onset potential of -0.117 V (vs. SCE) and a half-wave potential of -0.193 V (vs. SCE). In addition, sulfur-doped GC-NH demonstrated improved ORR activity compared to GC-NH with an onset potential of -0.117 V (vs. SCE) and a half-wave potential of -0.194 V (vs. SCE) (see Figure 28d). Although, two GC-NS with different synthesis temperature for N-doping show similar onset and half-wave potential values, but GC-NH showed poor limiting current alike its precursor, GC-NH. The low limiting current may have been caused by higher resistance of the film of the catalyst on the RDE, and insufficient active sites. Also, its incapability conveying through four-electron pathway during ORR (refer to section 2.1.5) may be the cause of poor limiting current of the polarization curve. As mentioned in previous section 4.3.2, XPS analysis of GC-NHS interestingly showed diminished or almost no nitrogen contents after the final sulfur-doping (Figure 27b). Therefore, GC-NHS is unable to demonstrate the synergetic effect of coexistence of N-species and S-species within the carbon network of GC composite. Referring to Figure 28c, ORR activities of GC composites consisting of the single heteroatom, either N or S, within carbon framework were compared. As shown, GC composite with only N-dopant outperformed that with only S-dopant in terms of both onset and half-wave potentials. Therefore, the temperature during N-doping process has affected the final product of subsequent S-doping; such that the GC composite N-doped at high temperature ultimately

resulted with absence of N-species, and that N-doped at relatively lower temperature retained its N-species even after doping additional heteroatom. Thus, owing to coexistence of N- and S-species in its graphitic network, GC-NLS showed promising ORR activity compare to that of GC-NHS that lacks in N-species to draw a synergetic effect.

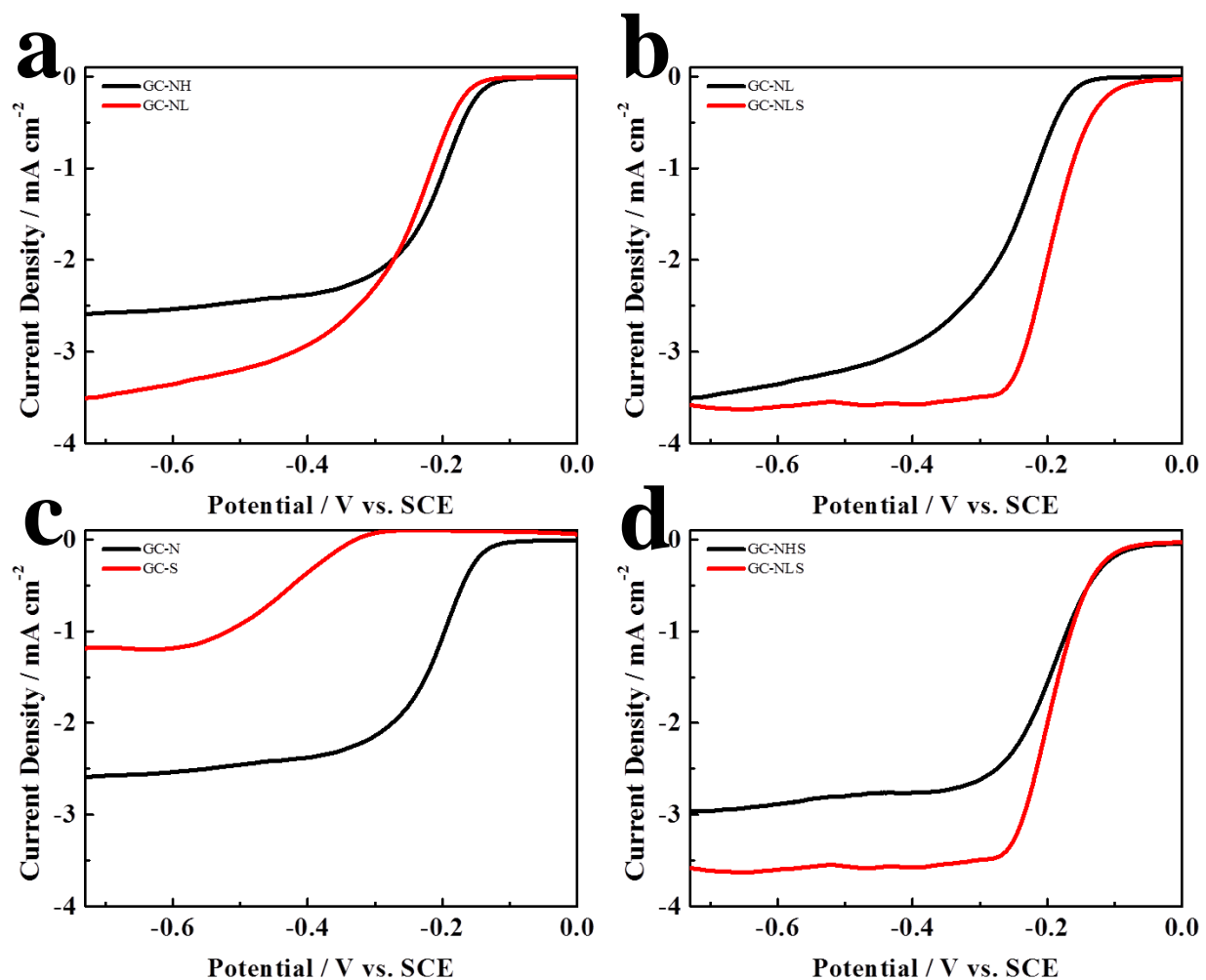


**Figure 28.** Linear sweep voltammetry (LSV) in evaluating oxygen reduction reaction in 0.1 M KOH at a scan rate of 10 mV s<sup>-1</sup>. a) Comparison of ORR performance of GC-NH and GC-NL b) Comparison of ORR performance of GC-NL and GC-NLS c) Comparison of ORR performance of GC-N and GC-S d)

As presented in Figure 29a, ORR polarization curves of GC-NLS at various rotation rates are used to produce Koutechý-Levich (K-L) plots to determine the number of electrons transferred at the surface of the electrocatalyst (Figure 29a inset). K-L plot is determined referring to section

2.4.6. As shown in Figure 29a inset, at different ORR potentials with various rotating speeds,  $\omega$  in rpm, the number of electrons transferred was found in near domain of 4.0, which suggests a four-electron reduction of oxygen during the cathodic reaction owing to the synergetic effect by S- and N-species. Enhanced onset and half-wave potentials of GC-NLS still shows incompetent performance to those of Pt-C in an alkaline electrolyte (onset and half-wave values of Pt-C are -0.021 V (vs. SCE) and -0.120 V (vs. SCE), respectively). However, the absence of metals in GC-NLS offers a lot of advantages during commercialization. The novelty of GC-NLS owes to its competent ORR performance compared to others that have been reported. In addition, coexistence of offers synergetic effects which contributed to its promising onset and half-wave potentials as a metal-free electrocatalyst.<sup>6, 168, 172-176</sup>

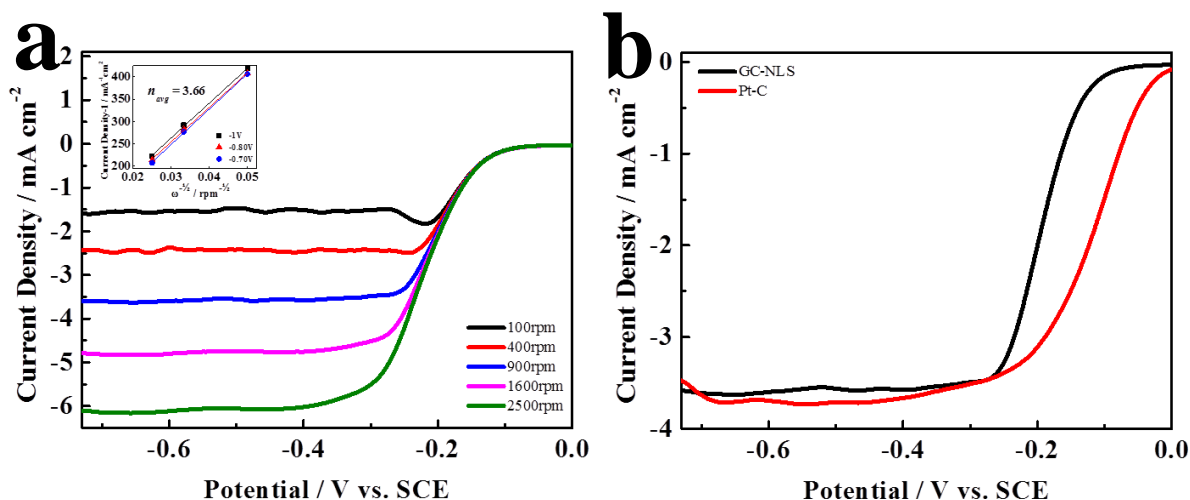


**Figure 29.** Linear sweep voltammetry (LSV) in evaluating oxygen reduction reaction in 0.1 M KOH at a scan rate of 10 mV s<sup>-1</sup>. a) LSVs of GC-NLS at different rotating speeds (Inset: Koutecký-Levich plot) c) Comparison of ORR performance of GC-NLS and Pt-C

#### 4.4 Conclusion

This chapter introduces metal free catalyst based on the two carbon allotropes, CNT and graphene, and the effects of multiple heteroatom dopants, sulfur and nitrogen, on its catalytic activity. Through the completion of this work, we have developed efficient metal free cathode catalysts of which its active sites are created by the co-doping of sulfur and nitrogen within the graphitic network. The effect of temperature on nitrogen doping using  $\text{NH}_3$  gas has also been investigated. With lower temperature, the subsequent S-doping by pyrolysis of the mix of PDS and N-doped graphene and CNT composite produces active ORR catalyst. The high temperature N-doped catalyst results in lower limiting current due to the lack of N-species after S-doping process. Therefore, the synergetic effect of the heteroatom dopant and the carbon composite delivers excellent ORR activity, which shows promising onset and half-wave potentials of -0.117 V (vs. SCE) and -0.193 V (vs. SCE).

## 5.0 Summary and Future Directions

Excellent properties of carbon based electrocatalyst and its promising performance in ORR activity have been demonstrated throughout the work as solutions to the essential problem in fuel cell community. Herein, the work is aimed to study the potentials of carbon based materials as cathode catalyst to ultimately replace the expensive and unstable precious metal currently used in fuel cell technologies. Surface modifications have been investigated to enhance intrinsic properties to be more effective as electrocatalysts for fuel cell applications.

In the first investigation, a facile synthesis method of graphitic nanoshells was reviewed. The method eliminated the use of solutions as the mixing base, which instead incorporated the precursor through one step physical mixing. As the result of the one step synthesis, nanoshells are created by the folding of the graphitic edges. These edges of the nanoshells greatly enhanced the electron transfer property of pristine graphene sheet. Also, the addition of iron species induced the formation of the nanoshells and produced further active sites for ORR. The ORR performance of the final catalyst, Fe-NG, was tested in a half-cell RDE setup. The outstanding ORR activity was observed owing to its unique morphology and the presence of iron induced active sites. The novelty of this work lies in the simple method of producing graphene base material with complex yet fascinating morphology which contributes to the excellent ORR activity.

The second study was conducted to further improve cost of the cathode electrode by developing metal free ORR catalyst. In this study, CNT is used in combination with graphene as an additional substrate. Therefore, the progress of developing efficient ORR catalysts currently focuses on metal-free functionalized carbon based catalysts, CNT and graphene composite.

Through modifications by heteroatom doping, CNT and graphene offers to be a very electron conductive support material with high affinity towards ORR. The premise of this study is to synthesize and investigated the effect of heteroatoms, nitrogen and sulfur, on CNT and graphene composite. Alongside to nitrogen dopants, sulfur in the graphitic framework has demonstrated its synergistic effect in improving the ORR activity. Additionally, the high temperature during the N-doping attributed to the reduction of N contents after the subsequent sulfur doping step. The synergetic effect was demonstrated after the subsequent sulfur doping when prepared in low temperature during N-doping step. The low temperature N-doping have allowed the addition of sulfur doping into the graphitic network, which greatly enhanced its ORR activity as tested in the half-cell RDE system.

Endless effort must be made in order to leap forward in the development of efficient fuel cells, specifically in its electrode fabrications. As mentioned previously, various fuel cell types are attracting electrochemistry community as potential sustainable and renewable energy resources. The present investigations provide an exceptional understanding the fundamentals involved in ORR catalysis by carbon based materials without the addition of precious metal. Using this knowledge, possible future works can be directed to non-precious catalysts developments for metal-air battery technology as listed in the following:

1. Optimization of ORR activity of graphene and CNT composite by amplifying the synergetic effect from both nitrogen and sulfur dopants.
2. Addition of NCNT to graphene based nanoshell structure with metal oxides or mixed metal oxides to further optimize the ORR activities in both aqueous and alkaline electrolytes for a broad range of applications both in metal-air battery and fuel cell technologies as a bi-functional catalyst.

3. Combination of GC-NS with non-precious metals and metal oxides (such as cobalt oxides) to lower the overpotentials during the charge and discharge processes of the battery as an efficient bi-functional catalyst.

## References

1. Lee, J. S.; Kim, S. T.; Cao, R.; Choi, N. S.; Liu, M.; Lee, K. T.; Cho, J., Metal-Air Batteries with High Energy Density: Li-Air versus Zn-Air. *Adv Energy Mater* **2011**, *1* (1), 34-50.
2. Armand, M.; Tarascon, J. M., Building better batteries. *Nature* **2008**, *451* (7179), 652-657.
3. Liu, Q.; Zhang, H. Y.; Zhong, H. W.; Zhang, S. M.; Chen, S. L., N-doped graphene/carbon composite as non-precious metal electrocatalyst for oxygen reduction reaction. *Electrochim Acta* **2012**, *81*, 313-320.
4. Lee, D. U.; Kim, B. J.; Chen, Z. W., One-pot synthesis of a mesoporous NiCo<sub>2</sub>O<sub>4</sub> nanoplatelet and graphene hybrid and its oxygen reduction and evolution activities as an efficient bi-functional electrocatalyst. *J Mater Chem A* **2013**, *1* (15), 4754-4762.
5. Wu, J.; Li, W. M.; Higgins, D.; Chen, Z. W., Heat-Treated Nonprecious Catalyst Using Fe and Nitrogen-Rich 2,3,7,8-Tetra(pyridin-2-yl)pyrazino[2,3-g]quinoxaline Coordinated Complex for Oxygen Reduction Reaction in PEM Fuel Cells. *J Phys Chem C* **2011**, *115* (38), 18856-18862.
6. Zheng, Y.; Jiao, Y.; Ge, L.; Jaroniec, M.; Qiao, S. Z., Two-Step Boron and Nitrogen Doping in Graphene for Enhanced Synergistic Catalysis. *Angew Chem Int Edit* **2013**, *52* (11), 3110-3116.
7. Tombaz, S.; Vastberg, A.; Zander, J., Energy- and Cost-Efficient Ultra-High-Capacity Wireless Access. *Ieee Wirel Commun* **2011**, *18* (5), 18-24.
8. United States. Congress. Senate. Committee on Energy and Natural Resources., *U.S. global energy outlook for 2012 : hearing before the Committee on Energy and Natural Resources, United States Senate, One Hundred Twelfth Congress, second session, to receive testimony on the U.S. global energy outlook for 2012, January 31, 2012*. U.S. G.P.O. : For sale by the Supt. of Docs., U.S. G.P.O.: Washington, 2012; p iii, 61 p.
9. Deane, J. P.; Gallachoir, B. P. O.; McKeogh, E. J., Techno-economic review of existing and new pumped hydro energy storage plant. *Renew Sust Energ Rev* **2010**, *14* (4), 1293-1302.
10. Bouffard, F.; Galiana, F. D., Stochastic security for operations planning with significant wind power generation. *Ieee T Power Syst* **2008**, *23* (2), 306-316.
11. Benitez, L. E.; Benitez, P. C.; van Kooten, G. C., The economics of wind power with energy storage. *Energ Econ* **2008**, *30* (4), 1973-1989.
12. Dunn, B.; Kamath, H.; Tarascon, J. M., Electrical Energy Storage for the Grid: A Battery of Choices. *Science* **2011**, *334* (6058), 928-935.
13. Skyllas-Kazacos, M.; Chakrabarti, M. H.; Hajimolana, S. A.; Mjalli, F. S.; Saleem, M., Progress in Flow Battery Research and Development. *J Electrochem Soc* **2011**, *158* (8), R55-R79.
14. Burke, A. F., Batteries and ultracapacitors for electric, hybrid, and fuel cell vehicles. *P Ieee* **2007**, *95* (4), 806-820.
15. Winter, M.; Brodd, R. J., What are batteries, fuel cells, and supercapacitors? *Chem Rev* **2004**, *104* (10), 4245-4269.
16. McCloskey, B. D.; Scheffler, R.; Speidel, A.; Bethune, D. S.; Shelby, R. M.; Luntz, A. C., On the Efficacy of Electrocatalysis in Nonaqueous Li-O<sub>2</sub> Batteries. *J Am Chem Soc* **2011**, *133* (45), 18038-18041.
17. Broussely, M.; Planchat, J. P.; Rigobert, G.; Virey, D.; Sarre, G., Lithium-ion batteries for electric vehicles: performances of 100 Ah cells. *J Power Sources* **1997**, *68* (1), 8-12.

18. Kennedy, B.; Patterson, D.; Camilleri, S., Use of lithium-ion batteries in electric vehicles. *J Power Sources* **2000**, *90* (2), 156-162.
19. Fergus, J. W., Recent developments in cathode materials for lithium ion batteries. *J Power Sources* **2010**, *195* (4), 939-954.
20. Arora, P.; White, R. E.; Doyle, M., Capacity fade mechanisms and side reactions in lithium-ion batteries. *J Electrochem Soc* **1998**, *145* (10), 3647-3667.
21. Wagner, F. T.; Lakshmanan, B.; Mathias, M. F., Electrochemistry and the Future of the Automobile. *J Phys Chem Lett* **2010**, *1* (14), 2204-2219.
22. Akani, M., Review of recent developments with metal-air batteries for electric vehicles. *New Materials for Fuel Cell and Modern Battery Systems Ii* **1997**, 239-251.
23. Girishkumar, G.; McCloskey, B.; Luntz, A. C.; Swanson, S.; Wilcke, W., Lithium - Air Battery: Promise and Challenges. *J Phys Chem Lett* **2010**, *1* (14), 2193-2203.
24. Kraysberg, A.; Ein-Eli, Y., Review on Li-air batteries-Opportunities, limitations and perspective. *J Power Sources* **2011**, *196* (3), 886-893.
25. Shimizu, Y.; Matsuda, H.; Miura, N.; Yamazoe, N., Bi-Functional Oxygen-Electrode Using Large Surface-Area Perovskite-Type Oxide Catalyst for Rechargeable Metal-Air Batteries. *Chem Lett* **1992**, (6), 1033-1036.
26. Chen, G. Y.; Delafuente, D. A.; Sarangapani, S.; Mallouk, T. E., Combinatorial discovery of bifunctional oxygen reduction - water oxidation electrocatalysts for regenerative fuel cells. *Catal Today* **2001**, *67* (4), 341-355.
27. Lu, Y. C.; Gasteiger, H. A.; Shao-Horn, Y., Catalytic Activity Trends of Oxygen Reduction Reaction for Nonaqueous Li-Air Batteries. *J Am Chem Soc* **2011**, *133* (47), 19048-19051.
28. Sheng, W. C.; Lee, S. W.; Crumlin, E. J.; Chen, S.; Shao-Horn, Y., Synthesis, Activity and Durability of Pt Nanoparticles Supported on Multi-walled Carbon Nanotubes for Oxygen Reduction. *J Electrochem Soc* **2011**, *158* (11), B1398-B1404.
29. Lee, S.; Zhu, S. L.; Milleville, C. C.; Lee, C. Y.; Chen, P. W.; Takeuchi, K. J.; Takeuchi, E. S.; Marschilok, A. C., Metal-Air Electrochemical Cells: Silver-Polymer-Carbon Composite Air Electrodes. *Electrochem Solid St* **2010**, *13* (11), A162-A164.
30. Lee, S. W.; Chen, S.; Suntivich, J.; Sasaki, K.; Adzic, R. R.; Shao-Horn, Y., Role of Surface Steps of Pt Nanoparticles on the Electrochemical Activity for Oxygen Reduction. *J Phys Chem Lett* **2010**, *1* (9), 1316-1320.
31. Cheng, F. Y.; Shen, J. A.; Peng, B.; Pan, Y. D.; Tao, Z. L.; Chen, J., Rapid room-temperature synthesis of nanocrystalline spinels as oxygen reduction and evolution electrocatalysts. *Nat Chem* **2011**, *3* (1), 79-84.
32. Lee, Y.; Suntivich, J.; May, K. J.; Perry, E. E.; Shao-Horn, Y., Synthesis and Activities of Rutile IrO<sub>2</sub> and RuO<sub>2</sub> Nanoparticles for Oxygen Evolution in Acid and Alkaline Solutions. *J Phys Chem Lett* **2012**, *3* (3), 399-404.
33. Kinoshita, K.; Electrochemical Society., *Electrochemical oxygen technology*. Wiley: New York, 1992; p xiv, 431 p.
34. Peng, B.; Chen, J., Functional materials with high-efficiency energy storage and conversion for batteries and fuel cells. *Coordin Chem Rev* **2009**, *253* (23-24), 2805-2813.
35. Cheng, F. Y.; Chen, J., Metal-air batteries: from oxygen reduction electrochemistry to cathode catalysts. *Chem Soc Rev* **2012**, *41* (6), 2172-2192.
36. Abraham, K. M.; Jiang, Z., A polymer electrolyte-based rechargeable lithium/oxygen battery. *J Electrochem Soc* **1996**, *143* (1), 1-5.

37. Ogasawara, T.; Debart, A.; Holzapfel, M.; Novak, P.; Bruce, P. G., Rechargeable Li<sub>2</sub>O<sub>2</sub> electrode for lithium batteries. *J Am Chem Soc* **2006**, *128* (4), 1390-1393.
38. Hadjipaschalis, I.; Poullikkas, A.; Efthimiou, V., Overview of current and future energy storage technologies for electric power applications. *Renew Sust Energ Rev* **2009**, *13* (6-7), 1513-1522.
39. McLarnon, F. R.; Cairns, E. J., The Secondary Alkaline Zinc Electrode. *J Electrochem Soc* **1991**, *138* (2), 645-664.
40. Blurton, K. F.; Sammells, A. F., Metal-Air Batteries - Their Status and Potential - Review. *J Power Sources* **1979**, *4* (4), 263-279.
41. Li, W. Y.; Li, C. S.; Zhou, C. Y.; Ma, H.; Chen, J., Metallic magnesium nano/mesoscale structures: Their shape-controlled preparation and Mg/air battery applications. *Angew Chem Int Edit* **2006**, *45* (36), 6009-6012.
42. Reddy, T., *Linden's Handbook of Batteries, 4th Edition*. McGraw-hill: 2010.
43. Padbury, R.; Zhang, X. W., Lithium-oxygen batteries-Limiting factors that affect performance. *J Power Sources* **2011**, *196* (10), 4436-4444.
44. Sen, R. K.; Van Voorhees, S. L.; Ferrel, T. *Metal-air battery assessment*; PNL-6475; Other: ON: DE88011361 United States10.2172/7242201Other: ON: DE88011361Mon Nov 26 07:55:01 EST 2012NTIS, PC A05/MF A01; 1.PNNL; EDB-88-121665English; 1988; p Medium: ED.
45. Homa, A. S.; Rudd, E. J. In *The development of aluminum-air batteries for electric vehicles*, Energy Conversion Engineering Conference, 1989. IECEC-89., Proceedings of the 24th Intersociety, 6-11 Aug 1989; 1989; pp 1331-1334 vol.3.
46. Mohamad, A. A., Zn/gelled 6 M KOH/O<sub>2</sub> zinc-air battery. *J Power Sources* **2006**, *159* (1), 752-757.
47. Bard, A. J.; Faulkner, L. R., *Electrochemical Methods: Fundamentals and Applications*. Wiley: 2000.
48. Yang, C. C.; Lin, S. J., Improvement of high-rate capability of alkaline Zn-MnO<sub>2</sub> battery. *J Power Sources* **2002**, *112* (1), 174-183.
49. Zhang, X. G., Fibrous zinc anodes for high power batteries. *J Power Sources* **2006**, *163* (1), 591-597.
50. Lee, C. W.; Sathiyarayanan, K.; Eom, S. W.; Yun, M. S., Novel alloys to improve the electrochemical behavior of zinc anodes for zinc/air battery. *J Power Sources* **2006**, *160* (2), 1436-1441.
51. Devyatkina, T. I.; Gun'ko, Y. L.; Mikhalenko, M. G., Development of ways to diminish corrosion of zinc electrode. *Russ J Appl Chem+* **2001**, *74* (7), 1122-1125.
52. Sapkota, P.; Kim, H., Zinc-air fuel cell, a potential candidate for alternative energy. *J Ind Eng Chem* **2009**, *15* (4), 445-450.
53. Sapkota, P.; Kim, H., An experimental study on the performance of a zinc air fuel cell with inexpensive metal oxide catalysts and porous organic polymer separators. *J Ind Eng Chem* **2010**, *16* (1), 39-44.
54. Einerhand, R. E. F.; Visscher, W. H. M.; Barendrecht, E., Hydrogen-Production during Zinc Deposition from Alkaline Zincate Solutions. *J Appl Electrochem* **1988**, *18* (6), 799-806.
55. Arora, P.; Zhang, Z. M., Battery separators. *Chem Rev* **2004**, *104* (10), 4419-4462.
56. Chakkaravarthy, C.; Waheed, A. K. A.; Udupa, H. V. K., Zinc-Air Alkaline Batteries - a Review. *J Power Sources* **1981**, *6* (3), 203-228.

57. Muller, S.; Striebel, K.; Haas, O., La<sub>0.6</sub>Ca<sub>0.4</sub>CoO<sub>3</sub> - a Stable and Powerful Catalyst for Bifunctional Air Electrodes. *Electrochim Acta* **1994**, *39* (11-12), 1661-1668.
58. Eom, S. W.; Lee, C. W.; Yun, M. S.; Sun, Y. K., The roles and electrochemical characterizations of activated carbon in zinc air battery cathodes. *Electrochim Acta* **2006**, *52* (4), 1592-1595.
59. Wu, G.; Cui, G. F.; Li, D. Y.; Shen, P. K.; Li, N., Carbon-supported Co<sub>1.67</sub>Te<sub>2</sub> nanoparticles as electrocatalysts for oxygen reduction reaction in alkaline electrolyte. *J Mater Chem* **2009**, *19* (36), 6581-6589.
60. Norskov, J. K.; Rossmeisl, J.; Logadottir, A.; Lindqvist, L.; Kitchin, J. R.; Bligaard, T.; Jonsson, H., Origin of the overpotential for oxygen reduction at a fuel-cell cathode. *J Phys Chem B* **2004**, *108* (46), 17886-17892.
61. Jorissen, L., Bifunctional oxygen/air electrodes. *J Power Sources* **2006**, *155* (1), 23-32.
62. Neburchilov, V.; Wang, H. J.; Martin, J. J.; Qu, W., A review on air cathodes for zinc-air fuel cells. *J Power Sources* **2010**, *195* (5), 1271-1291.
63. Hamdani, M.; Singh, R. N.; Chartier, P., Co<sub>3</sub>O<sub>4</sub> and Co- Based Spinel Oxides Bifunctional Oxygen Electrodes. *Int J Electrochem Sc* **2010**, *5* (4), 556-577.
64. Nikolova, V.; Iliev, P.; Petrov, K.; Vitanov, T.; Zhecheva, E.; Stoyanova, R.; Valov, I.; Stoychev, D., Electrocatalysts for bifunctional oxygen/air electrodes. *J Power Sources* **2008**, *185* (2), 727-733.
65. Wang, B., Recent development of non-platinum catalysts for oxygen reduction reaction. *J Power Sources* **2005**, *152* (1), 1-15.
66. McLean, G. F.; Niet, T.; Prince-Richard, S.; Djilali, N., An assessment of alkaline fuel cell technology. *Int J Hydrogen Energ* **2002**, *27* (5), 507-526.
67. Gulzow, E., Alkaline fuel cells: A critical view. *J Power Sources* **1996**, *61* (1-2), 99-104.
68. Iliev, I.; Kaisheva, A.; Gamburgzev, S., Air Electrodes for Metal-Air Batteries and Fuel-Cells. *Proceedings of the 26th Intersociety Energy Conversion Engineering Conference, Vols 1-6* **1991**, C469-C470.
69. Geim, A. K., Graphene: Status and Prospects. *Science* **2009**, *324* (5934), 1530-1534.
70. Geim, A. K.; Novoselov, K. S., The rise of graphene. *Nat Mater* **2007**, *6* (3), 183-191.
71. Marcano, D. C.; Kosynkin, D. V.; Berlin, J. M.; Sinitskii, A.; Sun, Z. Z.; Slesarev, A.; Alemany, L. B.; Lu, W.; Tour, J. M., Improved Synthesis of Graphene Oxide. *Acs Nano* **2010**, *4* (8), 4806-4814.
72. Chen, J.; Yao, B. W.; Li, C.; Shi, G. Q., An improved Hummers method for eco-friendly synthesis of graphene oxide. *Carbon* **2013**, *64*, 225-229.
73. Avouris, P.; Dimitrakopoulos, C., Graphene: synthesis and applications. *Mater Today* **2012**, *15* (3), 86-97.
74. Brownson, D. A. C.; Kampouris, D. K.; Banks, C. E., Graphene electrochemistry: fundamental concepts through to prominent applications. *Chem Soc Rev* **2012**, *41* (21), 6944-6976.
75. Geim, A. K., Graphene prehistory. *Phys Scripta* **2012**, T146.
76. Novoselov, K. S.; Jiang, D.; Schedin, F.; Booth, T. J.; Khotkevich, V. V.; Morozov, S. V.; Geim, A. K., Two-dimensional atomic crystals. *P Natl Acad Sci USA* **2005**, *102* (30), 10451-10453.
77. Sun, Z. Z.; James, D. K.; Tour, J. M., Graphene Chemistry: Synthesis and Manipulation. *J Phys Chem Lett* **2011**, *2* (19), 2425-2432.

78. Novoselov, K. S.; Geim, A. K.; Morozov, S. V.; Jiang, D.; Zhang, Y.; Dubonos, S. V.; Grigorieva, I. V.; Firsov, A. A., Electric field effect in atomically thin carbon films. *Science* **2004**, *306* (5696), 666-669.
79. Bae, S.; Kim, H.; Lee, Y.; Xu, X. F.; Park, J. S.; Zheng, Y.; Balakrishnan, J.; Lei, T.; Kim, H. R.; Song, Y. I.; Kim, Y. J.; Kim, K. S.; Ozyilmaz, B.; Ahn, J. H.; Hong, B. H.; Iijima, S., Roll-to-roll production of 30-inch graphene films for transparent electrodes. *Nat Nanotechnol* **2010**, *5* (8), 574-578.
80. Pei, S. F.; Cheng, H. M., The reduction of graphene oxide. *Carbon* **2012**, *50* (9), 3210-3228.
81. Stankovich, S.; Dikin, D. A.; Piner, R. D.; Kohlhaas, K. A.; Kleinhammes, A.; Jia, Y.; Wu, Y.; Nguyen, S. T.; Ruoff, R. S., Synthesis of graphene-based nanosheets via chemical reduction of exfoliated graphite oxide. *Carbon* **2007**, *45* (7), 1558-1565.
82. Li, D.; Muller, M. B.; Gilje, S.; Kaner, R. B.; Wallace, G. G., Processable aqueous dispersions of graphene nanosheets. *Nat Nanotechnol* **2008**, *3* (2), 101-105.
83. Shin, H. J.; Kim, K. K.; Benayad, A.; Yoon, S. M.; Park, H. K.; Jung, I. S.; Jin, M. H.; Jeong, H. K.; Kim, J. M.; Choi, J. Y.; Lee, Y. H., Efficient Reduction of Graphite Oxide by Sodium Borohydride and Its Effect on Electrical Conductance. *Adv Funct Mater* **2009**, *19* (12), 1987-1992.
84. Yang, D.; Velamakanni, A.; Bozoklu, G.; Park, S.; Stoller, M.; Piner, R. D.; Stankovich, S.; Jung, I.; Field, D. A.; Ventrone, C. A.; Ruoff, R. S., Chemical analysis of graphene oxide films after heat and chemical treatments by X-ray photoelectron and Micro-Raman spectroscopy. *Carbon* **2009**, *47* (1), 145-152.
85. Becerril, H. A.; Mao, J.; Liu, Z.; Stoltenberg, R. M.; Bao, Z.; Chen, Y., Evaluation of solution-processed reduced graphene oxide films as transparent conductors. *Acs Nano* **2008**, *2* (3), 463-470.
86. Wang, X.; Zhi, L. J.; Mullen, K., Transparent, conductive graphene electrodes for dye-sensitized solar cells. *Nano Lett* **2008**, *8* (1), 323-327.
87. Pei, S. F.; Zhao, J. P.; Du, J. H.; Ren, W. C.; Cheng, H. M., Direct reduction of graphene oxide films into highly conductive and flexible graphene films by hydrohalic acids. *Carbon* **2010**, *48* (15), 4466-4474.
88. Sun, Z. Z.; Yan, Z.; Yao, J.; Beitler, E.; Zhu, Y.; Tour, J. M., Growth of graphene from solid carbon sources. *Nature* **2010**, *468* (7323), 549-552.
89. Berger, C.; Song, Z. M.; Li, X. B.; Wu, X. S.; Brown, N.; Naud, C.; Mayou, D.; Li, T. B.; Hass, J.; Marchenkov, A. N.; Conrad, E. H.; First, P. N.; de Heer, W. A., Electronic confinement and coherence in patterned epitaxial graphene. *Science* **2006**, *312* (5777), 1191-1196.
90. Li, X. S.; Cai, W. W.; An, J. H.; Kim, S.; Nah, J.; Yang, D. X.; Piner, R.; Velamakanni, A.; Jung, I.; Tutuc, E.; Banerjee, S. K.; Colombo, L.; Ruoff, R. S., Large-Area Synthesis of High-Quality and Uniform Graphene Films on Copper Foils. *Science* **2009**, *324* (5932), 1312-1314.
91. Sutter, P.; Hybertsen, M. S.; Sadowski, J. T.; Sutter, E., Electronic Structure of Few-Layer Epitaxial Graphene on Ru(0001). *Nano Lett* **2009**, *9* (7), 2654-2660.
92. Reina, A.; Jia, X. T.; Ho, J.; Nezich, D.; Son, H. B.; Bulovic, V.; Dresselhaus, M. S.; Kong, J., Large Area, Few-Layer Graphene Films on Arbitrary Substrates by Chemical Vapor Deposition. *Nano Lett* **2009**, *9* (1), 30-35.

93. Kim, K. S.; Zhao, Y.; Jang, H.; Lee, S. Y.; Kim, J. M.; Kim, K. S.; Ahn, J. H.; Kim, P.; Choi, J. Y.; Hong, B. H., Large-scale pattern growth of graphene films for stretchable transparent electrodes. *Nature* **2009**, *457* (7230), 706-710.
94. Li, X. S.; Magnuson, C. W.; Venugopal, A.; An, J. H.; Suk, J. W.; Han, B. Y.; Borysiak, M.; Cai, W. W.; Velamakanni, A.; Zhu, Y. W.; Fu, L. F.; Vogel, E. M.; Voelkl, E.; Colombo, L.; Ruoff, R. S., Graphene Films with Large Domain Size by a Two-Step Chemical Vapor Deposition Process. *Nano Lett* **2010**, *10* (11), 4328-4334.
95. Li, X. L.; Wang, X. R.; Zhang, L.; Lee, S. W.; Dai, H. J., Chemically derived, ultrasmooth graphene nanoribbon semiconductors. *Science* **2008**, *319* (5867), 1229-1232.
96. Kosynkin, D. V.; Lu, W.; Sinitskii, A.; Pera, G.; Sun, Z. Z.; Tour, J. M., Highly Conductive Graphene Nanoribbons by Longitudinal Splitting of Carbon Nanotubes Using Potassium Vapor. *Acs Nano* **2011**, *5* (2), 968-974.
97. Kosynkin, D. V.; Higginbotham, A. L.; Sinitskii, A.; Lomeda, J. R.; Dimiev, A.; Price, B. K.; Tour, J. M., Longitudinal unzipping of carbon nanotubes to form graphene nanoribbons. *Nature* **2009**, *458* (7240), 872-U5.
98. Jiao, L. Y.; Zhang, L.; Wang, X. R.; Diankov, G.; Dai, H. J., Narrow graphene nanoribbons from carbon nanotubes. *Nature* **2009**, *458* (7240), 877-880.
99. Yang, R.; Zhang, L. C.; Wang, Y.; Shi, Z. W.; Shi, D. X.; Gao, H. J.; Wang, E. G.; Zhang, G. Y., An Anisotropic Etching Effect in the Graphene Basal Plane. *Adv Mater* **2010**, *22* (36), 4014-4019.
100. Jin, Z.; Yao, J.; Kittrell, C.; Tour, J. M., Large-Scale Growth and Characterizations of Nitrogen-Doped Monolayer Graphene Sheets. *Acs Nano* **2011**, *5* (5), 4112-4117.
101. Li, X. L.; Wang, H. L.; Robinson, J. T.; Sanchez, H.; Diankov, G.; Dai, H. J., Simultaneous Nitrogen Doping and Reduction of Graphene Oxide. *J Am Chem Soc* **2009**, *131* (43), 15939-15944.
102. Lin, Z. Y.; Waller, G.; Liu, Y.; Liu, M. L.; Wong, C. P., Facile Synthesis of Nitrogen-Doped Graphene via Pyrolysis of Graphene Oxide and Urea, and its Electrocatalytic Activity toward the Oxygen-Reduction Reaction. *Adv Energy Mater* **2012**, *2* (7), 884-888.
103. Wang, H. B.; Maiyalagan, T.; Wang, X., Review on Recent Progress in Nitrogen-Doped Graphene: Synthesis, Characterization, and Its Potential Applications. *Acs Catal* **2012**, *2* (5), 781-794.
104. Shao, Y. Y.; Zhang, S.; Engelhard, M. H.; Li, G. S.; Shao, G. C.; Wang, Y.; Liu, J.; Aksay, I. A.; Lin, Y. H., Nitrogen-doped graphene and its electrochemical applications. *J Mater Chem* **2010**, *20* (35), 7491-7496.
105. Imamura, G.; Saiki, K., Synthesis of Nitrogen-Doped Graphene on Pt(111) by Chemical Vapor Deposition. *J Phys Chem C* **2011**, *115* (20), 10000-10005.
106. Deng, D. H.; Pan, X. L.; Yu, L. A.; Cui, Y.; Jiang, Y. P.; Qi, J.; Li, W. X.; Fu, Q. A.; Ma, X. C.; Xue, Q. K.; Sun, G. Q.; Bao, X. H., Toward N-Doped Graphene via Solvothermal Synthesis. *Chem Mater* **2011**, *23* (5), 1188-1193.
107. Wang, X., N-doping of graphene through electrothermal reactions with ammonia (vol 324, pg 768, 2009). *Science* **2010**, *329* (5998), 1467-1467.
108. Sheng, Z. H.; Shao, L.; Chen, J. J.; Bao, W. J.; Wang, F. B.; Xia, X. H., Catalyst-Free Synthesis of Nitrogen-Doped Graphene via Thermal Annealing Graphite Oxide with Melamine and Its Excellent Electrocatalysis. *Acs Nano* **2011**, *5* (6), 4350-4358.

109. Park, H. W.; Lee, D. U.; Nazar, L. F.; Chen, Z. W., Oxygen Reduction Reaction Using MnO<sub>2</sub> Nanotubes/Nitrogen-Doped Exfoliated Graphene Hybrid Catalyst for Li-O<sub>2</sub> Battery Applications. *J Electrochem Soc* **2013**, *160* (2), A344-A350.
110. Lee, D. U.; Yu, A.; Chen, Z., Nitrogen-doped Graphene as an Active Electrocatalyst for Oxygen Reduction Reaction. *Silicon Compatible Materials, Processes, and Technologies for Advanced Integrated Circuits and Emerging Applications 2* **2013**, *50* (2), 1887-1893.
111. Yang, Z.; Yao, Z.; Li, G. F.; Fang, G. Y.; Nie, H. G.; Liu, Z.; Zhou, X. M.; Chen, X.; Huang, S. M., Sulfur-Doped Graphene as an Efficient Metal-free Cathode Catalyst for Oxygen Reduction. *Acs Nano* **2012**, *6* (1), 205-211.
112. Yao, Z.; Nie, H. G.; Yang, Z.; Zhou, X. M.; Liu, Z.; Huang, S. M., Catalyst-free synthesis of iodine-doped graphene via a facile thermal annealing process and its use for electrocatalytic oxygen reduction in an alkaline medium. *Chem Commun* **2012**, *48* (7), 1027-1029.
113. Yang, L. J.; Jiang, S. J.; Zhao, Y.; Zhu, L.; Chen, S.; Wang, X. Z.; Wu, Q.; Ma, J.; Ma, Y. W.; Hu, Z., Boron-Doped Carbon Nanotubes as Metal-Free Electrocatalysts for the Oxygen Reduction Reaction. *Angew Chem Int Edit* **2011**, *50* (31), 7132-7135.
114. Brodie, B. C., On the Atomic Weight of Graphite. *Philosophical Transactions of the Royal Society of London* **1859**, *149*, 249-259.
115. Staudenmaier, L., Verfahren zur Darstellung der Graphits äure. *Berichte der deutschen chemischen Gesellschaft* **1898**, *31* (2), 1481-1487.
116. Hummers, W. S.; Offeman, R. E., Preparation of Graphitic Oxide. *J Am Chem Soc* **1958**, *80* (6), 1339-1339.
117. Bahr, J. L.; Yang, J. P.; Kosynkin, D. V.; Bronikowski, M. J.; Smalley, R. E.; Tour, J. M., Functionalization of carbon nanotubes by electrochemical reduction of aryl diazonium salts: A bucky paper electrode. *J Am Chem Soc* **2001**, *123* (27), 6536-6542.
118. Yu, M. F.; Lourie, O.; Dyer, M. J.; Moloni, K.; Kelly, T. F.; Ruoff, R. S., Strength and breaking mechanism of multiwalled carbon nanotubes under tensile load. *Science* **2000**, *287* (5453), 637-640.
119. Dai, H. J., Carbon nanotubes: Synthesis, integration, and properties. *Accounts of Chemical Research* **2002**, *35* (12), 1035-1044.
120. Zheng, M.; Huang, X. Y., Nanoparticles comprising a mixed monolayer for specific bindings with biomolecules. *J Am Chem Soc* **2004**, *126* (38), 12047-12054.
121. Zhou, O.; Fleming, R. M.; Murphy, D. W.; Chen, C. H.; Haddon, R. C.; Ramirez, A. P.; Glarum, S. H., Defects in Carbon Nanostructures. *Science* **1994**, *263* (5154), 1744-1747.
122. Hong, S.; Myung, S., Nanotube electronics - A flexible approach to mobility. *Nat Nanotechnol* **2007**, *2* (4), 207-208.
123. Li, H.; Liu, H.; Jong, Z.; Qu, W.; Geng, D. S.; Sun, X. L.; Wang, H. J., Nitrogen-doped carbon nanotubes with high activity for oxygen reduction in alkaline media. *Int J Hydrogen Energ* **2011**, *36* (3), 2258-2265.
124. Tang, Y. F.; Allen, B. L.; Kauffman, D. R.; Star, A., Electrocatalytic Activity of Nitrogen-Doped Carbon Nanotube Cups. *J Am Chem Soc* **2009**, *131* (37), 13200-+.
125. Gong, K. P.; Du, F.; Xia, Z. H.; Durstock, M.; Dai, L. M., Nitrogen-Doped Carbon Nanotube Arrays with High Electrocatalytic Activity for Oxygen Reduction. *Science* **2009**, *323* (5915), 760-764.
126. Stephan, O.; Ajayan, P. M.; Colliex, C.; Redlich, P.; Lambert, J. M.; Bernier, P.; Lefin, P., Doping Graphitic and Carbon Nanotube Structures with Boron and Nitrogen. *Science* **1994**, *266* (5191), 1683-1685.

127. Golberg, D.; Bando, Y.; Han, W.; Kurashima, K.; Sato, T., Single-walled B-doped carbon, B/N-doped carbon and BN nanotubes synthesized from single-walled carbon nanotubes through a substitution reaction. *Chem Phys Lett* **1999**, *308* (3-4), 337-342.
128. Han, W. Q.; Bando, Y.; Kurashima, K.; Sato, T., Boron-doped carbon nanotubes prepared through a substitution reaction. *Chem Phys Lett* **1999**, *299* (5), 368-373.
129. Cruz-Silva, E.; Cullen, D. A.; Gu, L.; Romo-Herrera, J. M.; Munoz-Sandoval, E.; Lopez-Urias, F.; Sumpter, B. G.; Meunier, V.; Charlier, J. C.; Smith, D. J.; Terrones, H.; Terrones, M., Heterodoped nanotubes: Theory, synthesis, and characterization of phosphorus-nitrogen doped multiwalled carbon nanotubes. *Acs Nano* **2008**, *2* (3), 441-448.
130. Maciel, I. O.; Campos-Delgado, J.; Cruz-Silva, E.; Pimenta, M. A.; Sumpter, B. G.; Meunier, V.; Lopez-Urias, F.; Munoz-Sandoval, E.; Terrones, H.; Terrones, M.; Jorio, A., Synthesis, Electronic Structure, and Raman Scattering of Phosphorus-Doped Single-Wall Carbon Nanotubes. *Nano Lett* **2009**, *9* (6), 2267-2272.
131. Sidik, R. A.; Anderson, A. B.; Subramanian, N. P.; Kumaraguru, S. P.; Popov, B. N., O-2 reduction on graphite and nitrogen-doped graphite: Experiment and theory. *J Phys Chem B* **2006**, *110* (4), 1787-1793.
132. Liu, H. S.; Song, C. J.; Tang, Y. H.; Zhang, J. L.; Zhang, H. J., High-surface-area CoTMPP/C synthesized by ultrasonic spray pyrolysis for PEM fuel cell electrocatalysts. *Electrochim Acta* **2007**, *52* (13), 4532-4538.
133. Lee, K.; Zhang, L.; Lui, H.; Hui, R.; Shi, Z.; Zhang, J. J., Oxygen reduction reaction (ORR) catalyzed by carbon-supported cobalt polypyrrole (Co-PPy/C) electrocatalysts. *Electrochim Acta* **2009**, *54* (20), 4704-4711.
134. Qu, L. T.; Liu, Y.; Baek, J. B.; Dai, L. M., Nitrogen-Doped Graphene as Efficient Metal-Free Electrocatalyst for Oxygen Reduction in Fuel Cells. *Acs Nano* **2010**, *4* (3), 1321-1326.
135. Chen, Z.; Higgins, D.; Chen, Z. W., Nitrogen doped carbon nanotubes and their impact on the oxygen reduction reaction in fuel cells. *Carbon* **2010**, *48* (11), 3057-3065.
136. Seiler, H., Secondary-Electron Emission in the Scanning Electron-Microscope. *J Appl Phys* **1983**, *54* (11), R1-R18.
137. Wischnitzer, S., *Introduction to electron microscopy*. Pergamon Press: New York.
138. Facility, A. M. M. R. My Scope: Training for Advanced Research. <http://www.ammr.org.au/> (accessed November 17, 2013).
139. Hollander, J. M.; Jolly, W. L., X-ray photoelectron spectroscopy. *Accounts of Chemical Research* **1970**, *3* (6), 193-200.
140. Liu, G.; Li, X. G.; Ganesan, P.; Popov, B. N., Development of non-precious metal oxygen-reduction catalysts for PEM fuel cells based on N-doped ordered porous carbon. *Appl Catal B-Environ* **2009**, *93* (1-2), 156-165.
141. Matter, P. H.; Zhang, L.; Ozkan, U. S., The role of nanostructure in nitrogen-containing carbon catalysts for the oxygen reduction reaction. *J Catal* **2006**, *239* (1), 83-96.
142. van Dommele, S.; Romero-Izquierdo, A.; Brydson, R.; de Jong, K. P.; Bitter, J. H., Tuning nitrogen functionalities in catalytically grown nitrogen-containing carbon nanotubes. *Carbon* **2008**, *46* (1), 138-148.
143. Kamiya, K.; Hashimoto, K.; Nakanishi, S., Instantaneous one-pot synthesis of Fe-N-modified graphene as an efficient electrocatalyst for the oxygen reduction reaction in acidic solutions. *Chem Commun (Camb)* **2012**, *48* (82), 10213-5.

144. Li, S. Z.; Hu, Y. Y.; Xu, Q.; Sun, J.; Hou, B.; Zhang, Y. P., Iron- and nitrogen-functionalized graphene as a non-precious metal catalyst for enhanced oxygen reduction in an air-cathode microbial fuel cell. *J Power Sources* **2012**, *213*, 265-269.
145. Instruments, P. *Raman Spectroscopy Basics*; 2012; pp 1-5.
146. Luo, Z. Q.; Lim, S. H.; Tian, Z. Q.; Shang, J. Z.; Lai, L. F.; MacDonald, B.; Fu, C.; Shen, Z. X.; Yu, T.; Lin, J. Y., Pyridinic N doped graphene: synthesis, electronic structure, and electrocatalytic property. *J Mater Chem* **2011**, *21* (22), 8038-8044.
147. Chen, Z. W.; Higgins, D.; Yu, A. P.; Zhang, L.; Zhang, J. J., A review on non-precious metal electrocatalysts for PEM fuel cells. *Energ Environ Sci* **2011**, *4* (9), 3167-3192.
148. Jaouen, F.; Marcotte, S.; Dodelet, J. P.; Lindbergh, G., Oxygen reduction catalysts for polymer electrolyte fuel cells from the pyrolysis of iron acetate adsorbed on various carbon supports. *J Phys Chem B* **2003**, *107* (6), 1376-1386.
149. Wu, G.; More, K. L.; Johnston, C. M.; Zelenay, P., High-Performance Electrocatalysts for Oxygen Reduction Derived from Polyaniline, Iron, and Cobalt. *Science* **2011**, *332* (6028), 443-447.
150. Bezerra, C. W. B.; Zhang, L.; Lee, K. C.; Liu, H. S.; Marques, A. L. B.; Marques, E. P.; Wang, H. J.; Zhang, J. J., A review of Fe-N/C and Co-N/C catalysts for the oxygen reduction reaction. *Electrochim Acta* **2008**, *53* (15), 4937-4951.
151. Dignardbailey, L.; Trudeau, M. L.; Joly, A.; Schulz, R.; Lalande, G.; Guay, D.; Dodelet, J. P., Graphitization and Particle-Size Analysis of Pyrolyzed Cobalt Phthalocyanine Carbon Catalysts for Oxygen Reduction in Fuel-Cells. *J Mater Res* **1994**, *9* (12), 3203-3209.
152. Fan, Z. J.; Kai, W.; Yan, J.; Wei, T.; Zhi, L. J.; Feng, J.; Ren, Y. M.; Song, L. P.; Wei, F., Facile Synthesis of Graphene Nanosheets via Fe Reduction of Exfoliated Graphite Oxide. *Acc Nano* **2011**, *5* (1), 191-198.
153. Lin, Z. Y.; Song, M. K.; Ding, Y.; Liu, Y.; Liu, M. L.; Wong, C. P., Facile preparation of nitrogen-doped graphene as a metal-free catalyst for oxygen reduction reaction. *Phys Chem Chem Phys* **2012**, *14* (10), 3381-3387.
154. Ozaki, J. I.; Nozawa, K.; Yamada, K.; Uchiyama, Y.; Yoshimoto, Y.; Furuichi, A.; Yokoyama, T.; Oya, A.; Brown, L. J.; Cashion, J. D., Structures, physicochemical properties and oxygen reduction activities of carbons derived from ferrocene-poly(furfuryl alcohol) mixtures. *J Appl Electrochem* **2006**, *36* (2), 239-247.
155. Nabae, Y.; Moriya, S.; Matsubayashi, K.; Lyth, S. M.; Malon, M.; Wu, L. B.; Islam, N. M.; Koshigoe, Y.; Kuroki, S.; Kakimoto, M. A.; Miyata, S.; Ozaki, J., The role of Fe species in the pyrolysis of Fe phthalocyanine and phenolic resin for preparation of carbon-based cathode catalysts. *Carbon* **2010**, *48* (9), 2613-2624.
156. Lefevre, M.; Dodelet, J. P.; Bertrand, P., O<sub>2</sub> reduction in PEM fuel cells: Activity and active site structural information for catalysts obtained by the pyrolysis at high temperature of Fe precursors. *J Phys Chem B* **2000**, *104* (47), 11238-11247.
157. Geng, D. S.; Chen, Y.; Chen, Y. G.; Li, Y. L.; Li, R. Y.; Sun, X. L.; Ye, S. Y.; Knights, S., High oxygen-reduction activity and durability of nitrogen-doped graphene. *Energ Environ Sci* **2011**, *4* (3), 760-764.
158. Luo, N.; Li, X. J.; Wang, X. H.; Yan, H. H.; Zhang, C. J.; Wang, H. T., Synthesis and characterization of carbon-encapsulated iron/iron carbide nanoparticles by a detonation method. *Carbon* **2010**, *48* (13), 3858-3863.
159. Gavillet, J.; Loiseau, A.; Journet, C.; Willaime, F.; Ducastelle, F.; Charlier, J. C., Root-growth mechanism for single-wall carbon nanotubes. *Phys Rev Lett* **2001**, *87* (27).

160. Yamashita, T.; Hayes, P., Analysis of XPS spectra of Fe<sup>2+</sup> and Fe<sup>3+</sup> ions in oxide materials. *Appl Surf Sci* **2008**, *254* (8), 2441-2449.
161. Maruyama, J.; Abe, I., Formation of platinum-free fuel cell cathode catalyst with highly developed nanospace by carbonizing catalase. *Chem Mater* **2005**, *17* (18), 4660-4667.
162. Peng, H. L.; Mo, Z. Y.; Liao, S. J.; Liang, H. G.; Yang, L. J.; Luo, F.; Song, H. Y.; Zhong, Y. L.; Zhang, B. Q., High Performance Fe- and N- Doped Carbon Catalyst with Graphene Structure for Oxygen Reduction. *Sci Rep-Uk* **2013**, *3*.
163. Schaber, P. A.; Colson, J.; Higgins, S.; Thielen, D.; Anspach, B.; Brauer, J., Thermal decomposition (pyrolysis) of urea in an open reaction vessel. *Thermochim Acta* **2004**, *424* (1-2), 131-142.
164. Rodriguez-Reinoso, F., The role of carbon materials in heterogeneous catalysis. *Carbon* **1998**, *36* (3), 159-175.
165. Tributsch, H.; Koslowski, U. I.; Dorbandt, I., Experimental and theoretical modeling of Fe-, Co-, Cu-, Mn-based electrocatalysts for oxygen reduction. *Electrochim Acta* **2008**, *53* (5), 2198-2209.
166. Bouwkamp-Wijnoltz, A. L.; Visscher, W.; van Veen, J. A. R., The selectivity of oxygen reduction by pyrrolysed iron porphyrin supported on carbon. *Electrochim Acta* **1998**, *43* (21-22), 3141-3152.
167. Iwazaki, T.; Obinata, R.; Sugimoto, W.; Takasu, Y., High oxygen-reduction activity of silk-derived activated carbon. *Electrochem Commun* **2009**, *11* (2), 376-378.
168. Xu, J. X.; Dong, G. F.; Jin, C. H.; Huang, M. H.; Guan, L. H., Sulfur and Nitrogen Co-Doped, Few-Layered Graphene Oxide as a Highly Efficient Electrocatalyst for the Oxygen-Reduction Reaction. *Chemsuschem* **2013**, *6* (3), 493-499.
169. Wohlgemuth, S. A.; White, R. J.; Willinger, M. G.; Titirici, M. M.; Antonietti, M., A one-pot hydrothermal synthesis of sulfur and nitrogen doped carbon aerogels with enhanced electrocatalytic activity in the oxygen reduction reaction. *Green Chem* **2012**, *14* (5), 1515-1523.
170. Ozaki, J.; Kimura, N.; Anahara, T.; Oya, A., Preparation and oxygen reduction activity of BN-doped carbons. *Carbon* **2007**, *45* (9), 1847-1853.
171. Terrones, M.; Grobert, N.; Olivares, J.; Zhang, J. P.; Terrones, H.; Kordatos, K.; Hsu, W. K.; Hare, J. P.; Townsend, P. D.; Prassides, K.; Cheetham, A. K.; Kroto, H. W.; Walton, D. R. M., Controlled production of aligned-nanotube bundles. *Nature* **1997**, *388* (6637), 52-55.
172. Liang, J.; Jiao, Y.; Jaroniec, M.; Qiao, S. Z., Sulfur and Nitrogen Dual-Doped Mesoporous Graphene Electrocatalyst for Oxygen Reduction with Synergistically Enhanced Performance. *Angew Chem Int Edit* **2012**, *51* (46), 11496-11500.
173. Long, J. L.; Xie, X. Q.; Xu, J.; Gu, Q.; Chen, L. M.; Wang, X. X., Nitrogen-Doped Graphene Nanosheets as Metal-Free Catalysts for Aerobic Selective Oxidation of Benzylic Alcohols. *Acs Catal* **2012**, *2* (4), 622-631.
174. Liu, Z.; Nie, H. G.; Yang, Z.; Zhang, J.; Jin, Z. P.; Lu, Y. Q.; Xiao, Z. B.; Huang, S. M., Sulfur-nitrogen co-doped three-dimensional carbon foams with hierarchical pore structures as efficient metal-free electrocatalysts for oxygen reduction reactions. *Nanoscale* **2013**, *5* (8), 3283-3288.
175. Ma, Y. W.; Sun, L. Y.; Huang, W.; Zhang, L. R.; Zhao, J.; Fan, Q. L.; Huang, W., Three-Dimensional Nitrogen-Doped Carbon Nanotubes/Graphene Structure Used as a Metal-Free Electrocatalyst for the Oxygen Reduction Reaction. *J Phys Chem C* **2011**, *115* (50), 24592-24597.

176. Chizari, K.; Janowska, I.; Houle, M.; Florea, I.; Ersen, O.; Romero, T.; Bernhardt, P.; Ledoux, M. J.; Pham-Huu, C., Tuning of nitrogen-doped carbon nanotubes as catalyst support for liquid-phase reaction. *Appl Catal a-Gen* **2010**, 380 (1-2), 72-80.